Measurements of ship emissions using in-situ and LP-DOAS instruments

Dissertation
zur Erlangung des akademischen Grades
Doktor der Naturwissenschaften
(Dr. rer. nat)

Institut für Umweltphysik
Fachbereich Physik und Elektrotechnik
Universität Bremen

Vorgelegt von:
Kai Krause
Bremen, März 2023

1. Gutachter: Prof. Dr. John P. Burrows
2. Gutachter: Prof. Dr. Markus Quante

Datum des Kolloquiums: 08.06.2023

Abstract

Ships are an important source of pollutants along busy waterways. Depending on the type of ship, sea going or inland vessel, different key pollutants are emitted. In all cases, ships equipped with combustion engines are strong emitters of NO_x (NO + NO_2) and other pollutants emitted by combustion processes. Additionally, sea going ships are also strong emitters of SO_2. Generally, NO_x and SO_2 are key parameters of air quality. These pollutants can be monitored by different kinds of instruments, e.g. in-situ instruments and remote sensing instruments.

In the first part of this thesis, the capabilities of active remote sensing to monitor ship emissions will be presented. A LP-DOAS instrument specifically designed by the company Airyx to monitor ship emissions will be presented and compared to a scientific LP-DOAS instrument. To highlight the opportunities offered by LP-DOAS measurements for the monitoring of ship emissions, one year of LP-DOAS measurements made across the river Elbe close to Hamburg are evaluated. Elevated concentrations of NO_2 and SO_2 are assigned to individual ship passages and a method to derive emission rates of SO_2, NO_2, and NO_x using a Gaussian plume model is presented. More than 7000 individual ship passages have been monitored and their respective emission rates have been derived. The emission rates have been analysed in the context of ship type (inland or sea going), length, and speed over ground. The emission rates were compared to emission factors from previous studies and show good agreement.

In the second part, ship emission rates of individual inland vessels are derived from several years of measurement in the lower Rhine area, specifically in Duisburg and Neuss. The emission rates were derived from on-shore in-situ measurements using an improved version of the algorithm presented in the first part. Elevated concentrations of NO_x were assigned to the corresponding source ships and each ship passage was simulated a Gaussian-puff model to derive the NO_x emission rate of the respective source ship. In total over 32900 ship passages have been monitored in a time frame of four years of measurement. The emission rates were analysed in the context of the ship size, ship speed over ground, ship speed in water, and direction of travel. Comparison of on-board and on-shore emission rates for selected ships participating in the EU Life project CLINSH showed good agreement between both methods. The derived emission rates also agree with emission factors from previous studies. In most cases, the ships comply with emission regulations.

Scientific Publications

Articles in peer-reviewed journals

- **Krause, K.**, Wittrock, F., Richter, A., Busch, D., Bergen, A., Burrows, J. P., Freitag, S., and Halbherr, O.: Determination of NO_x emission rates of inland ships from on-shore measurements, Atmos. Meas. Tech. [accepted], https://doi.org/10.5194/egusphere-2022-767, 2022.

- Lange, K., Richter, A., Schönhardt, A., Meier, A. C., Bösch, T., Seyler, A., **Krause, K.**, Behrens, L. K., Wittrock, F., Merlaud, A., Tack, F., Fayt, C., Friedrich, M. M., Dimitropoulou, E., Van Roozendael, M., Kumar, V., Donner, S., Dörner, S., Lauster, B., Razi, M., Borger, C., Uhlmannsiek, K., Wagner, T., Ruhtz, T., Eskes, H., Bohn, B., Santana Diaz, D., Abuhassan, N., Schüttemeyer, D., and Burrows, J. P.: Validation of Sentinel-5P TROPOMI tropospheric NO2 products by comparison with NO2 measurements from airborne imaging DOAS, ground-based stationary DOAS, and mobile car DOAS measurements during the S5P-VAL-DE-Ruhr campaign, Atmos. Meas. Tech., 16, 1357–1389, https://doi.org/10.5194/amt-16-1357-2023, 2023.

- **Krause, K.**, Wittrock, F., Richter, A., Schmitt, S., Pöhler, D., Weigelt, A., and Burrows, J. P.: Estimation of ship emission rates at a major shipping lane by long-path DOAS measurements, Atmos. Meas. Tech., 14, 5791–5807, https://doi.org/10.5194/amt-14-5791-2021, 2021.

Conference Talks

- **Krause, K.**, Wittrock, F., Richter, A., Busch, D., Bergen, A., Burrows, J.P.: "Estimation of ship emission rates from on shore measurements", SETAC German Language Branch e.V. 25. Jahrestagung, Germany, September 2021.

- **Krause, K.**, Wittrock, F., Richter, A., Schmitt, S., Pöhler, D., Weigelt, A., Burrows, J.P.: "Ermittlung von SO_2 und NO_x Emissionsraten fahrender Schiffe aus Langpfad-DOAS Messungen", virtual DPG Spring Meeting, Germany, September 2021

- **Krause, K.**, Wittrock, F., Schmitt, S., Pöhler, D., Weigelt, A. Schmolke, S., Burrows, J.P.: "Comparative measurements for detection of ship emissions", EGU General Assembly, Vienna, Austria, April 2019

- **Krause, K.**, Wittrock, F., Schmitt, S., Pöhler, D., Weigelt, A. Schmolke, S., Burrows, J.P.: "Comparative measurements of two Long Path DOAS for detection of ship emissions", DPG Spring Meeting, Munich, Germany, March 2019

Non peer-reviewed Publications

- Richter, A., Seyler, A., **Krause, K.**, Wittrock, F., Schmitt, S., Pöhler, D.: Messungen von Schiffsemissionen mit differentieller optischer Absorptions-Spektroskopie (DOAS), Gefahrstoffe, 10.37544/0949-8036-2022-05-06-61, 2022

- Busch, D., **Krause, K.**: Air quality on the Rhine and in the inland ports of Duisburg and Neuss – Immission-side effect of emissions from shipping and port operations on nitrogen oxide pollution – Results from the EU Life Project "Clean Inland Shipping" (CLINSH), Immissionsschutz, pp. 78–85, 2021

Contents

1 Motivation

According to the World Health Organization (WHO), 99 % of the global population breathe air with high levels of pollution, leading to 7 million deaths per year (WHO, 2023). Air pollution can be caused by different sources, these can be anthropogenic or natural. Anthropogenic sources are e.g. fossil fuel combustion, biomass burning, industrial production, mining activities or intensive agriculture. Natural sources are e.g., volcanoes or forest fires.

Ships are an important source of air pollution, especially in coastal regions and harbour cities. Within the last decades, the global fleet steadily grew and the amount of goods transported by ship has more than quadrupled since 1970 (Löschke, 2021). With the increase in fleet size, also the emissions caused by the shipping industry increased. Most air pollution by international shipping takes place within 400 km of land (Eyring et al., 2010), making it relevant for air quality on shore. The most important air pollutants emitted by ships are SO_2, NO_x, black carbon (BC), volatile organic compounds (VOC), particulate matter (PM) and greenhouse gases.

There are regulations in place to limit the amount of pollutants emitted by the shipping sector. For sea going ships, these regulations are set by the International Maritime Organization (IMO) and are defined within the MARPOL Annex VI protocol (International Maritime Organization, 2019). In addition, emissions from ships are also regulated by national and international law, e.g. by EU regulations. Currently, these regulations focus on SO_2 and NO_x emissions. For inland ships, different regulations exist. In Europe, the first regulations were established by EU Directive 97/68/EC, later superseded by EU Regulation 2016/1628 (European Parliament and European Council, 1998, 2015). Appropriate monitoring systems are required to monitor compliance with these regulations.

In this thesis, the emissions of both, sea going and inland ships are investigated. The first main objective was to evaluate the performance of a newly developed long path DOAS (LP-DOAS) system, specifically designed to monitor ship emissions, and compare the new system to a scientific LP-DOAS. The comparison of both systems aims to determine whether the new instrument is suitable to monitor ship emissions and delivers similar data quality as the scientific instrument. For the comparison, both systems were set up at a measurement site at the river Elbe, close to Hamburg. At this point the Elbe serves as passage way from the North Sea and Kiel Canal towards the Hamburg harbour and vice versa. The second goal was to analyse the LP-DOAS data in the context of ship

emissions. A new method to derive emission rates of individual ship passages out of the data measured by the LP-DOAS instruments has been developed. The emission rates of sea going and inland ships have been derived using the new method and were analysed in regard to ship speed, ship size and ship type.
The third goal was to improve the newly developed method and to make it applicable for in-situ measurements. In this context, NO_x emission rates of inland ships have been derived from two in-situ measurement stations at the Rhine in North-Rhine Westphalia. In total, four years of measurements were successfully evaluated and over 33000 individual ship emission rates were derived and analysed in context of the ship type, direction of travel and ship speed.
Additionally, traffic statistics of inland ships have been derived for individual river segments of the river Rhine, and in conjunction with the emission rates allowed to establish a realistic high resolution emission register of inland ship emissions at the Rhine. As a proof of concept the total NO_x emissions of certain river segments have been computed for the year 2018 and were compared to NO_x emissions caused by different power plants.

Outline of this thesis

The thesis is structured as follows: In chapter 2, a brief introduction to the structure of the atmosphere, its chemical composition and air pollution is given. In the context of air pollution, the chemical reactions of NO_x and SO_2 within the atmosphere and a basic description of the modelling of the transport and dispersion of air pollutants is provided. In chapter 3, the importance of the shipping sector, ship emissions and the regulations regarding ship emissions are highlighted. Chapter 4 gives a brief introduction to Differential Optical Absorption Spectroscopy (DOAS). Chapter 5 describes the measurement site at the river Elbe and comprises the evaluation and comparison of the two LP-DOAS instruments, the description of the new method to derive emission rates and the analysis of the emission rates of inland and sea ships. In chapter 6, the measurement sites in North-Rhine Westphalia are introduced along with the improvements made to the algorithm for the derivation of ship emission rates. A dataset of four years of measurement for two in-situ measurement stations is analysed in the context of inland ship emissions. Additionally, a way to derive the traffic statistics from AIS (automated identification system) signals is presented. Ultimately, a new approach to combine traffic statistics and emission rates to establish a high resolution emission register of inland ship emissions is demonstrated. Chapter 7 presents the future challenges the shipping industry has to overcome to reduce the emissions of GHG and air pollutants. Finally, chapter 8 summarizes the findings of this thesis and gives an outlook on future tasks and developments.

2 Introduction

2.1 The Atmosphere

[1] The atmosphere is a gaseous layer attracted by Earth's gravitation, separating the surface of the Earth from space. The current composition is the result of an evolutionary process, which started when the planet was formed. Earth was formed 4.5 billion years ago by the accretion of small celestial bodies (planetesimals) that condensed from the solar nebula during its cooling. The first atmosphere was rapidly dissipated before the gases could be retained by strong gravitational fields. The secondary atmosphere formed out of the released volatile compounds from the planet itself. Earth's early atmosphere consisted mainly out of CO_2, N_2, H_2O and H_2, a mixture similar to the gases emitted by volcanoes. The water vapour condensed and formed the first oceans and seas. CO_2 was dissolved into the oceans and ultimately formed sedimentary carbonate rock. As N_2 is chemically inert and not soluble in water, it accumulated over geologic time scales and became the most abundant constituent. The atmosphere from 3 billion to 2.3 billion years ago was rich in reduced gases, e.g. H_2 and CH_4. About 2.3 billion years ago, O_2 levels increased, after cyanobacteria started to produce oxygen by photosynthesis. Even though cyanobacteria are believed to exist since at least 3 billion years, the increase in atmospheric oxygen levels was delayed by the oxidation of the continental crusts. Today, the concentration of O_2 is maintained by the production from photosynthesis and removal through respiration and decay of organic matter. In summary, the evolution of Earth's atmosphere depended on different factors and physical processes together with biological activity at the surface contributed to the evolution of Earth's atmosphere.

2.1.1 Chemical composition of the atmosphere

Today, the main constituents of the atmosphere are N_2, O_2 and Argon (Ar), which together account for more than 99.9 % of the atmospheric air volume. All other constituents occur in small abundances and are therefore called trace gases. Noble gases show a stable mixing ratio throughout the atmosphere, while other gases are highly variable on different time scales. CO_2 for example shows a seasonal variability due to the uptake and release from

[1] This chapter is based on Brasseur and Solomon (2005); Kraus (2004); Seinfeld and Pandis (2006); Wallace and Hobbs (2006)

Table 2.1: Composition of dry tropospheric air at a pressure of 1013 hPa (Wallace and Hobbs, 2006).

Gas	Chemical formula	Volume mixing ratio	Major sources
Nitrogen	N_2	78.084 %	Biological
Oxygen	O_2	20.946 %	Biological
Argon	Ar	0.934 %	Radiogenic
Carbon dioxide	CO_2	379 ppmv	Biological, oceanic, combustion
Neon	Ne	18.18 ppmv	Volcanic
Helium	He	5.24 ppmv	Radiogenic
Methane	CH_4	1.7 ppmv	Biological, anthropogenic
Hydrogen	H_2	0.56 ppmv	Biological, anthropogenic
Nitrous oxide	N_2O	0.31 ppmv	Biological, anthropogenic
Carbon monoxide	CO	40 - 200 ppbv	Photochemical, combustion, anthropogenic
Ozone	O_3	10 - 100 ppbv	Photochemical
Nitrogen species (NO + NO_2 + NO_3 + N_2O_5 + HNO_3 + PAN)	NO_y	10 pptv - 1 ppmv	Soils, anthropogenic, lightning
Ammonia	NH_3	10 pptv - 1ppbv	Biological
Sulphur dioxide	SO_2	10 pptv - ppbv	Photochemical, volcanic, anthropogenic
Hydroxyl radical	OH	0 - 0.4 pptv	Photochemical
Hydroperoxyl radical	HO_2	0 - 5 pptv	Photochemical

vegetation, with an additional increase due to anthropogenic release. Most chemical reactions in the atmosphere involve radicals (e.g. OH, NO, NO_2), which quickly react and their concentration is therefore also highly variable. Table 2.1 shows the chemical atmospheric composition at the surface.

2.1.2 Vertical structure of the atmosphere

Generally, the atmosphere shows a distinguished temperature profile and layers can be specified. The layers are the troposphere, stratosphere, mesosphere, thermosphere and exosphere.

The troposphere is the lowest layer extending up to 12 km on average. In colder conditions the vertical extent is lower, e.g. about 9 km at the poles, and in warmer climates such as the tropics it can reach up to heights of about 18 km. The height of the troposphere

also changes with season. The troposphere is characterized by a negative temperature gradient of about -6.5 $\mathrm{K\,km^{-1}}$. The gradient is caused by surface heating at the ground and adiabatic cooling due to the decreasing pressure at higher altitudes. Due to the temperature gradient, the troposphere is generally unstable, which means warmer (less dense) air parcels can rise. While rising, the air parcels cool down and moisture condensates, leading to cloud formation. Almost all known weather phenomena are happening in the troposphere. Also approximately 80 % of the mass of the whole atmosphere is concentrated in the troposphere. The upper boundary of the troposphere is the tropopause, where the temperature gradient changes its sign and temperature increases with height.

The troposphere can be further split up into the atmospheric boundary layer (ABL), also known as planetary boundary layer (PBL), and the free troposphere. The ABL is the part of the troposphere closest to the ground, with a thickness of a few meters to several km. On average the ABL reaches heights around 1 km, in colder conditions or during night it can be much less, on the order of around 100 m and under highly convective conditions, it can reach heights of about 3 km. Within the ABL strong mixing of air masses takes place, due to turbulence caused by heating of the ground surface and vertical wind shear caused by the friction on the ground. Vertical mixing in this layer takes place on small time scales, e.g. within minutes to hours. As a result there is a well mixed layer in the ABL, without strong gradients in the potential temperature, humidity, wind speed and pollutant concentration.

The ABL shows a diurnal cycle. Starting in the morning after sunrise, the surface temperature starts to increase due to absorption of incoming solar radiation. The air close to the surface heats up as well and starts to rise and in turn increases the height of the mixed layer. The maximum height is reached in the afternoon. The mixed layer is capped by the entrainment layer, which connects the ABL to the free troposphere. In this entrainment layer vertical movement is hindered due to a temperature inversion. In the evening, when the sun sets, the surface cools down due to radiative cooling and the convection breaks down. This results in a temperature inversion and the formation of a stable layer close to the ground with a residual mixed layer above. Some mixing still takes place due to vertical wind shear caused by the friction on the ground. As the stable layer is much shallower compared to a well developed mixed layer, the concentration of pollutants is usually the highest during night. Also during night there is no production of OH radicals, which react with pollutants and remove them from the atmosphere.

In cities the diurnal cycle is less pronounced, due to the urban heat island effect. Urban areas are compromised of high amounts of man made materials with a large heat capacity (e.g. concrete, asphalt). These materials store large amounts of heat during day and the surface cooling does not take place during night or is not as strong as in other places, resulting in a less frequent night time inversion of the temperature profile.

Similarly, the situation over the ocean is different to the situation on land. The large

thermal inertia of water dampens the effects and temperature changes occur on monthly rather scales rather than daily. The marine boundary layer (MBL) shows stable stratification when the water is cold and unstable mixed conditions when the water is warm.
The next layer above the troposphere is the stratosphere, which extents from the tropopause up to the stratopause in 50 to 55 km height. The stratosphere is very dry and rich in ozone, approximately 90 % of the atmospheric ozone is found here. Ozone absorbs UV radiation < 320 nm, and this absorption results in an increase of temperature. The maximum ozone mixing ratio is found at a height of about 35 km, caused by the decrease of O_2 concentration with higher altitudes and reduction of photons in the UV in lower altitudes.
The ozone concentration in the stratosphere can be described by the Chapman cycle, which can be described by a set of simple reactions:

$$O_2 \xrightarrow{hv} 2\,O(^3P) \tag{R 2.1}$$

$$O(^3P) + O_2 + M \longrightarrow O_3 + M \tag{R 2.2}$$

$$O_3 \xrightarrow{hv} O(^1D) + O_2 \tag{R 2.3}$$

$$O_3 \xrightarrow{hv} + O(^3P) + O_2 \tag{R 2.4}$$

$$O_3 + O(^3P) \longrightarrow 2\,O_2 \tag{R 2.5}$$

where M is a third molecule (N_2 or O_2) needed for the reaction. Modelling the Chapman cycle allows to get ozone distributions which resemble the real ozone distribution but are about a factor of two too high. Additional loss terms are needed to get to realistic values.
Within the stratosphere the temperature increases with height and reaches a maximum at the stratosphere. Vertical movement of air parcels is reduced and the stratopause can be considered as stable and stratified, hence the name stratosphere.
The next layer above the stratosphere is called mesosphere, which extends from the stratopause to the mesopause in 85 km height. The mesosphere is also the coldest layer of the atmosphere, with minimum temperatures of -90 to -100 °C. Due to the negative temperature gradient with height vertical mixing can occur again. The thermosphere extents from the mesopause up to the thermopause at 600 km height.

2.2 Air pollution

Air pollution generally describes the presence of substances at concentrations above their normal ambient levels that have a measurable effect on humans, animals, vegetation or materials (Seinfeld and Pandis, 2006). This definition includes any substance and does not differentiate between benign and noxious effects, but generally the effects are undesirable (Seinfeld and Pandis, 2006). Often times, the high concentrations are caused by

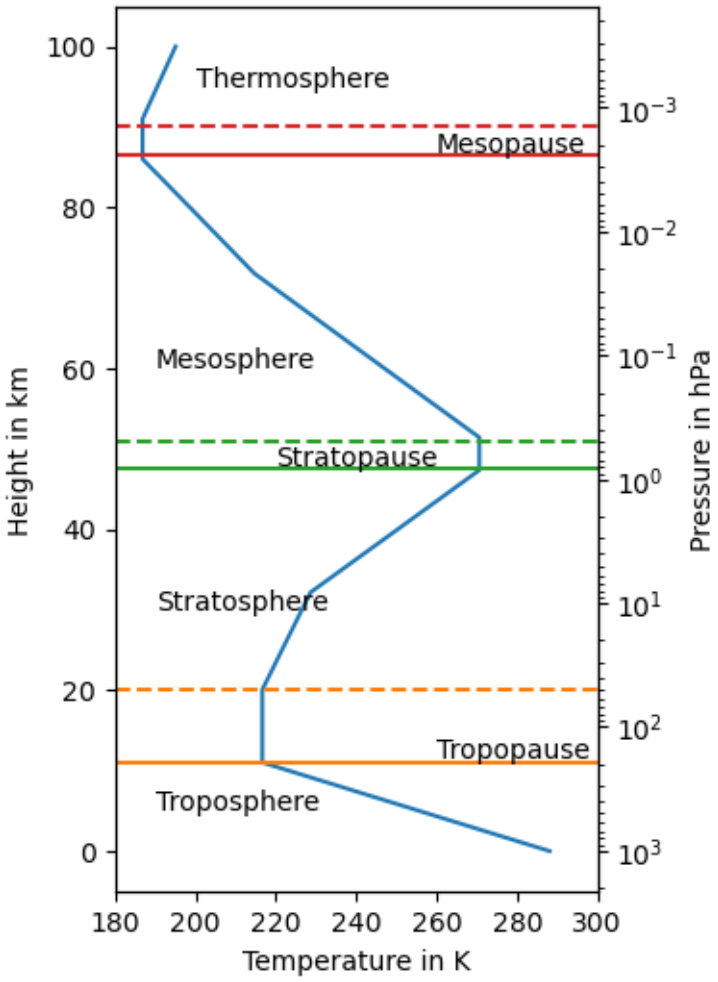

Figure 2.1: Vertical temperature profile of the US standard atmosphere 1976, values taken from Kraus (2004).

anthropogenic activities, e.g. fossil fuel combustion, biomass burning, industrial production, mining activities or intensive animal farming. But also natural air pollution exists, e.g. caused by forest fires or volcanic eruptions. Air pollutants have different lifetimes and can stay in the atmosphere from minutes to years (Naceur et al., 2016). Generally, air pollutants can be separated into primary pollutants, which are directly emitted and secondary pollutants, which are created in the air by chemical reactions. Some air pollutants can be classified as both, because the can be emitted directly, but also form from other substances in the atmosphere.

The World Health Organization (WHO) reports on six major air pollutants, particulate matter (PM), ozone, carbon monoxide, sulphur oxides, nitrogen oxides ($NO+NO_2 = NO_x$) and lead, but other chemical substances are classified as air pollutant as well, e.g. volatile organic compounds (VOC), polycyclic aromatic hydrocarbons (PAH) and dioxins (Manisalidis et al., 2020). Air pollution is great environmental threat to health, and can lead to stroke, heart diseases, lung cancer, chronic obstructive pulmonary diseases, respiratory infections and acute and chronic respiratory diseases (WHO, 2023). According to the WHO, almost all of the global population is exposed to high levels of pollutants, which exceed the WHO guideline limits. Low- and middle-income countries suffer from the highest exposures. Generally the WHO estimates that air pollution is responsible for about 7 million deaths globally per year (WHO, 2023). Next to health concerns, air pollution also has an influence on the environment and can lead to acidification of soils and water bodies and can cause damage to plants, e.g. stunted growth, premature ageing and necrosis.

Anthropogenic sources of air pollution are for example fossil fuel combustion in power plants, traffic and industrial processes, waste incineration, waste deposition and agriculture (e.g. manure management, soils). Figure 2.2 shows the yearly NO_x and SO_2 emissions of Germany. For SO_2 the strongest emissions were generated by fossil-fuel power plants. The strong decrease in SO_2 emissions is mainly caused by flue-gas desulfurization of fossil-fuel power plants, due to this, the relative contribution of other emissions increased. Generally, the SO_2 emissions in Germany decreased by 95.7 % compared to 1990 levels. The reduction of NO_x emissions are the result of the use of catalytic converters in vehicles, fuels with lower emission factors and the de-industrialization of eastern Germany. Generally, the NO_x emissions decreased by 66 %, with the strongest decrease in traffic emissions. Nevertheless, traffic still remains the most important source of NO_x emissions, followed by power plants and industrial plants. Also agriculture, especially agriculturally used soil is a relevant source of NO_x.

Within the EU there are regulations in place to protect humans and environment from harmful air pollutants. These regulations have different limits for different periods of time, e.g. hourly mean concentrations, daily mean concentrations and yearly mean concentrations. For Germany these limits can be found in the 39. BImSchV. For SO_2 the hourly

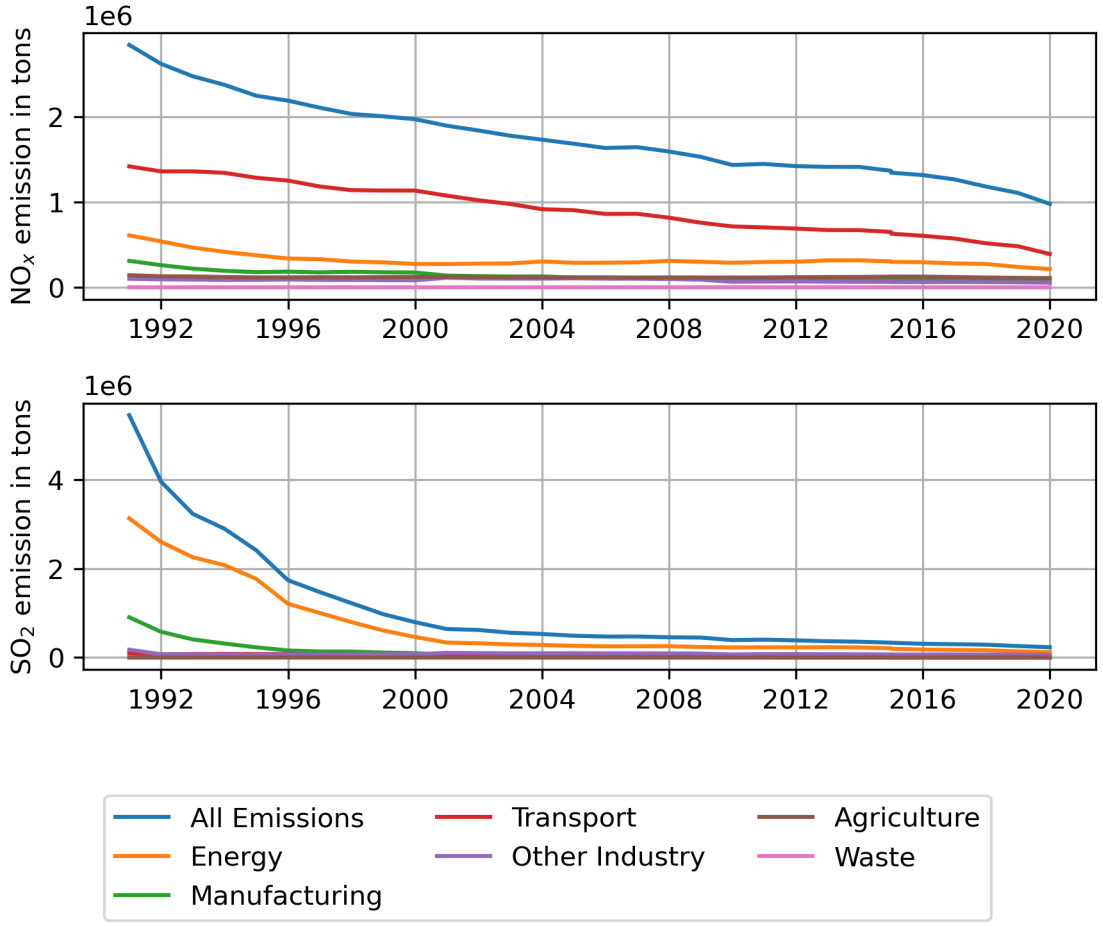

Figure 2.2: Trend of yearly NO_x and SO_2 emissions of Germany split by source (UBA, 2022).

mean concentration limit of 350 $\mu g\,m^{-3}$ is only allowed to be exceeded 24 times per year, the daily limit of 125 $\mu g\,m^{-3}$ is only allowed to be exceeded three times per year. For the protection of vegetation, there is also an annual mean threshold value of 20 $\mu g\,m^{-3}$. For NO_2, the hourly mean value is 200 $\mu g\,m^{-3}$, which is only allowed to be exceeded 18 times per year. The yearly mean value is 40 $\mu g\,m^{-3}$. To protect the vegetation, there is also a limit for the annual mean NO_x concentration (30 $\mu g\,m^{-3}$).
In this thesis, the SO_2 and NO_x emissions of ships are investigated. Therefore, the dominant sources, sinks and most important reactions of NO_x and SO_2 will be presented in the next two paragraphs. A more detailed look at the emissions of NO_x and SO_2 caused by shipping, the specific regulations regarding these emissions and an overview over the literature will be given in Chapter 2.

2.2.1 NO_x chemistry in the troposphere

[2] The major source of NO_x, which is the sum of NO and NO_2, in the atmosphere are anthropogenic combustion processes, e.g. in industrial production, traffic or biomass burning. Natural sources include bush fires, emissions from soil and lightning. NO_2 is a reddish-brown toxic gas with a distinctive smell, while NO is colourless. Due to their impact on health and the environment, both are routinely monitored in urban areas. NO_x is a precursor for Ozone, aerosol production and acid rain.
The main emissions of NO_x out of combustion processes is so called thermal NO_x, which is NO_x that is formed from atmospheric N_2 and O_2 during the combustion, while only a minor part stems from oxidation of organic nitrogen compounds contained in the fuel. Emissions of fuel NO primarily play a role when petroleum, coal or biomass is burned. Due to the high temperatures during the combustion process, atmospheric molecular nitrogen can react with oxygen to form thermal NO (Wallace and Hobbs, 2006). According to Wallace and Hobbs (2006) at temperatures below 4500 K the reactions are:

$$O_2 + M \rightleftharpoons 2\,O + M \tag{R 2.6}$$

$$2\,O + 2\,N_2 \rightleftharpoons 2\,NO + 2\,N \tag{R 2.7}$$

$$2\,N + 2\,O_2 \rightleftharpoons 2\,NO + O_2 \tag{R 2.8}$$

which can be summarized as:

$$O_2 + N_2 + M \rightleftharpoons 2\,NO + M \tag{R 2.9}$$

In these reactions, and the following reactions, M represents an inert molecule (usually N_2 or O_2) that absorbs excess molecular energies. Reactions R2.7 and R2.8 are highly

[2] This paragraph is based on Seinfeld and Pandis (2006); Wallace and Hobbs (2006)

temperature dependent and the resulting NO does not react back in the equilibrium reactions, as the combustion gases cool rapidly and drastically decrease the reaction rates of the reverse reactions. Consequently, the produced NO gets emitted into the atmosphere. After the emission, NO reacts with atmospheric O_3 and forms NO_2, which in turn gets photolysed rapidly by incoming radiation and an equilibrium is established. In this equilibrium there is no net production or removal of O_3, as NO and NO_2 constantly get converted into each other, thus these three chemicals form a null cycle. Consequently, NO and NO_2 are often summarized as NO_x.

$$NO + O_3 \longrightarrow NO_2 + O_2 \tag{R 2.10}$$

$$NO_2 \xrightarrow{h\nu\, \lambda < 420\,nm} NO + O(^3P) \tag{R 2.11}$$

$$O(^3P) + O_2 + M \longrightarrow O_3 + M \tag{R 2.12}$$

At night NO_x is only present as NO_2, because of reaction R2.10 and the lack of sunlight. During daytime, NO_x gets primarily removed from the atmosphere by dry and wet deposition as HNO_3:

$$NO_2 + OH + M \longrightarrow HNO_3 + M \tag{R 2.13}$$

The lifetime of NO_2 during daytime at the surface is about 1 day. NO_2 can also be further oxidized to NO_3.

$$NO_2 + O_3 \longrightarrow NO_3 + O_2 \tag{R 2.14}$$

During daytime NO_3 is rapidly photolysed again by incoming solar radiation and can either form NO or NO_2, depending on the wavelength.

$$NO_3 \xrightarrow{h\nu\, \lambda < 700\,nm} NO + O_2 \tag{R 2.15}$$

$$NO_3 \xrightarrow{h\nu\, \lambda < 580\,nm} NO_2 + O \tag{R 2.16}$$

Additionally, NO_3 can also react with NO.

$$NO_3 + NO \longrightarrow 2\,NO_2 \tag{R 2.17}$$

The lifetime of NO_3 at noon in sunlight is only about 5 seconds, but during night it can accumulate, and further react with a NO_2 molecule to form N_2O_5.

$$NO_3 + NO_2 + M \rightleftharpoons N_2O_5 + M \tag{R 2.18}$$

N_2O_5 can also thermally decompose to NO_2 and NO_3.

$$N_2O_5 + M \longrightarrow NO_2 + NO_3 + M \quad \text{(R 2.19)}$$

N_2O_5 can react with water to form HNO_3, which then consequently gets removed by wet and dry deposition.

$$N_2O_5 + H_2O\,(s) \longrightarrow 2\,HNO_3 \quad \text{(R 2.20)}$$

Together reactions R2.13 and R2.20 are the major pathways for the removal of NO_x from the atmosphere. This reaction is also a source of aerosols.

2.2.2 SO_2 chemistry in the troposphere

[3] Sulphur compounds exist in reduced and oxidised states, ranging from oxidation numbers of -2 to +6. In the atmosphere of the Earth, sulphur is generally oxidised to +4 and eventually to +6 oxidation numbers. Sulphur with an oxidation number of +6 is the stable form of sulphur in the presence of oxygen. The most important sulphur gases in the atmosphere are SO_2, H_2S, dimethyl sulphide (CH_3SCH_3 or DMS), COS and CS_2. The sources differ for the different sulphur compounds. DMS is released by the oceans, where it is produced by biological reactions. H_2S is emitted from soils, marshlands, volcanoes and oceans. CS_2 is of biogenic origin and in turn the source of COS, which results from a reaction of CS_2 with OH.
The natural sources of SO_2 are the oxidation of DMS and H_2S,

$$OH + H_2S \longrightarrow H_2O + HS \quad \text{(R 2.21)}$$

The resulting HS then reacts with O_3 or NO_2 and forms HSO, which is in turn rapidly converted to SO_2.

$$HS + O_3 \longrightarrow HSO + O_2 \quad \text{(R 2.22)}$$

$$HS + NO_2 \longrightarrow HSO + NO \quad \text{(R 2.23)}$$

$$HSO + O_3 \longrightarrow HSO_2 + O_2 \quad \text{(R 2.24)}$$

$$HSO_2 + O_2 \longrightarrow HO_2 + SO_2 \quad \text{(R 2.25)}$$

There are also direct sources of SO_2, e.g. volcanoes, biomass burning, smelting of sulphur-containing ores and fossil fuel combustion, which is the largest source. The amount of emitted SO_2 depends on the amount of sulphur in the burnt fuel.
In the atmosphere SO_2 is oxidized by the following reactions:

[3] This paragraph is based on Seinfeld and Pandis (2006); Wallace and Hobbs (2006)

$$OH + SO_2 + M \longrightarrow HOSO_2 + M \quad \text{(R 2.26)}$$

$$HOSO_2 + O_2 \longrightarrow HO_2 + SO_3 \quad \text{(R 2.27)}$$

$$SO_3 + H_2O \longrightarrow H_2SO_4 \quad \text{(R 2.28)}$$

SO_2 is also oxidized to H_2SO_4 in water, e.g. cloud droplets. Additionally, SO_2 is also soluble in water and forms H_2SO_3. H_2SO_4 and H_2SO_3 are both acids, consequently, SO_2 emissions contribute to the formation of acid rain. H_2SO_4 also acts as an aerosol and has a negative effect on radiative forcing.

2.2.3 Dispersion of pollutants in the atmosphere

In general, atmospheric dispersion and transport is rather complex due to the contribution of the different scales of turbulence, but nevertheless, simple approximations can be used to describe these processes. In this thesis a simplified look at dispersion processes of ship plumes is needed and therefore will be described and discussed here.

Emitted pollutants are transported and dispersed within the atmosphere by the atmospheric flow. Atmospheric flow is complex and many different scales of motion are superimposed onto each other (Wallace and Hobbs, 2006). The mean transport is according to the mean wind, while the dispersion happens due to turbulence. Turbulence is the random, three dimensional fluctuation at different scales smaller than the characteristic scale of the phenomenon, consequently, these are called sub scale fluctuations (Kraus, 2008). The random fluctuations can be imagined to be swirls within the mean flow and are often called eddies (Wallace and Hobbs, 2006). An illustration of the superimposed fluctuations is shown in Figure 2.3. Each individual eddy quickly disappears and is replaced by a succession of different eddies. Turbulence can be generated by different means, mechanically, thermally or inertially. Mechanically induced turbulence can form out of a shear in the mean wind, e.g. change in wind speed or direction with height. This shear can be caused by frictional drag or by wake turbulence, such as wind swirls behind obstacles (Wallace and Hobbs, 2006). Thermal turbulence consists of thermals of warm air that rise and cold air that sinks due to buoyancy (Wallace and Hobbs, 2006). Inertial turbulence is a special form of shear turbulence, where wind shear is generated by larger eddies and smaller eddies form at the edges of larger ones (Wallace and Hobbs, 2006).

A simple way to describe atmospheric transport, diffusion and dispersion of emitted pollutants of the atmosphere are the Gaussian-plume-model and the Gaussian-puff-model (Pasquill, 1968; Stutton, 1932). These models are based on analytical solutions of the diffusion equation, for a homogeneous wind field and diffusion coefficients which have have no variation in time or space (Zenger, 1998).

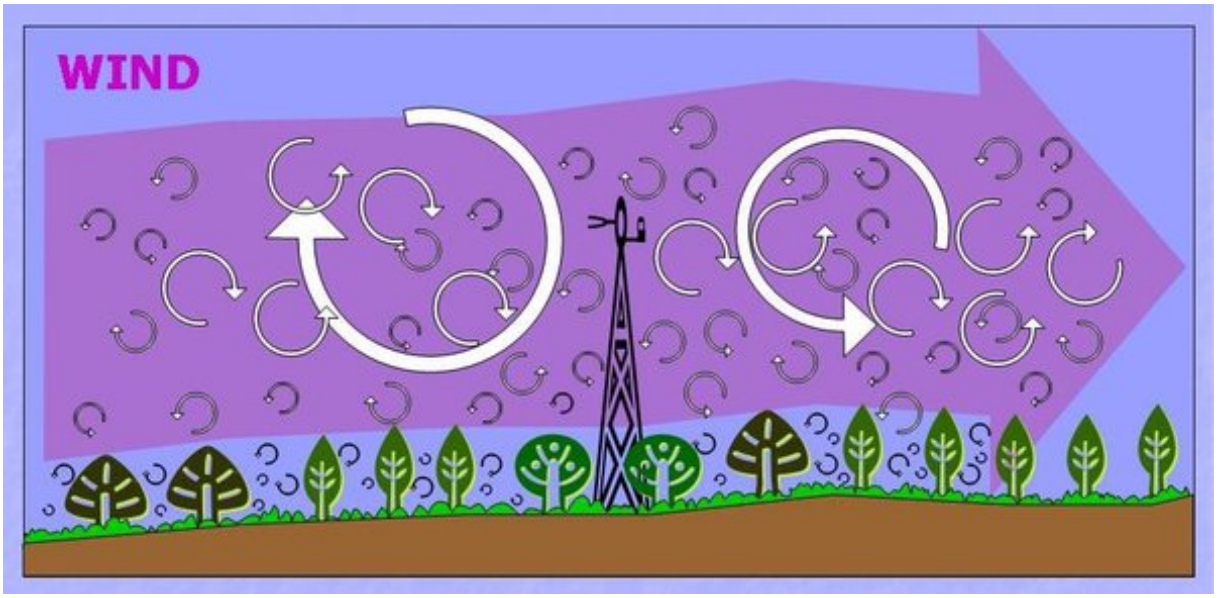

Figure 2.3: Illustration of eddies superimposed onto the mean wind (https://upload.wikimedia.org/wikipedia/commons/6/65/Py%C3%B6rrekovarianssi-tekniikan_kaaviokuva.jpg).

$$\frac{\partial C}{\partial t} = K_x \frac{\partial^2 C}{\partial x^2} + K_y \frac{\partial^2 C}{\partial y^2} + K_z \frac{\partial^2 C}{\partial z^2} + Q \tag{2.1}$$

Equation 2.1 describes how diffusion processes change the concentration over time (Fick's second law), where x, y and z are the spatial coordinates, K_x, K_y and K_z are the diffusion coefficients for the respective spatial coordinate, and Q is an additional source or sink. For long diffusion times, this can be transferred to turbulent mixing processes (Zenger, 1998).

The Gaussian-puff-model is a solution for equation 2.1 for the release of a point-shaped emission (a puff) of a fixed amount of pollutants Q_{tot} at x_0,y_0, H which has been transported for an amount of time t:

$$C(x,y,z,t) = \frac{Q_{tot}}{\sqrt{(4\pi t)^3 K_x K_y K_z}} \cdot exp - \left[-\frac{(x-x_0)^2}{4K_x t} + \frac{(y-y_0)^2}{4K_y t} + \frac{(z-H)^2}{4K_z t} \right] \tag{2.2}$$

The transport by the mean wind (U) can be considered by movement of the individual puffs by the wind. H is the effective stack height, which is the sum of the height of the stack h and the initial rise of the plume Δh (see Figure 2.6). Further the terms $K_{x,y,z}t$ can be simplified to the square of standard deviations $\sigma^2_{x,y,z} = 2K_{x,y,z}t$ of a Gaussian-distribution, which then results in the Gaussian-puff-model (Hanna et al., 1982; Zenger, 1998):

$$C(x,y,z,t) = \frac{Q_{tot}}{(2\pi)^{3/2}\sigma_x(t)\sigma_y(t)\sigma_z(t)} \cdot \exp\left(-\frac{1}{2}\cdot\left[\left(\frac{x-Ut}{\sigma_x(t)}\right)^2 + \left(\frac{y}{\sigma_y(t)}\right)^2 + \left(\frac{z-H}{\sigma_z(t)}\right)^2\right]\right) \tag{2.3}$$

where x now is aligned with the mean wind direction. This model still only considers an instantaneous release of pollutants and not continuous emission. Continuous emission can be realised as subsequent emission of individual puffs with a constant emission rate and consistent time steps. Q_{tot} of an individual puff would then be (Qdt), where dt is the duration of time to release a single puff and Q is the emission rate. For long distances downwind, the Gaussian plume can reach the ground, and would even penetrate into it. To correct for this, the model has to be modified so that the plume does not penetrate into the ground, but considers the reflection at the ground. Within Gaussian dispersion models, the reflection of the plume at the ground is modelled using a second, identical source in negative height ($z = -H$). Both plumes will then overlap and the concentration where they overlap will be the sum of both (see also Figure 2.4). Further simplification and assuming that each $\sigma_{x,y,z}(t)$ is constant during the modelled period of time, leads to the following equation:

$$C(x,y,z) = \sum_{i=1}^{N} \frac{(Qdt)_i}{(2\pi)^{3/2}\sigma_x\sigma_y\sigma_z} \cdot \exp\left(-\frac{(x-Ut)^2}{2\sigma_x^2}\right) \cdot \exp\left(-\frac{y^2}{2\sigma_y^2}\right) \cdot \left[exp\left(-\frac{(z-H)^2}{2\sigma_z^2}\right) + exp\left(-\frac{(z+H)^2}{2\sigma_z^2}\right)\right] \tag{2.4}$$

where the concentration at a point $(C(x,y,z))$ can be described as the sum over all released puffs $((Qdt)_i)$, and the concentration distribution of each puff is a function of the emission rate (Q), the dispersion due to atmospheric stability (σ_x, σ_y, σ_z), the length of time of the emission (dt) at a certain source point (x=0, y=0, z=H), the total transport time (t) and the wind speed (U).

To further simplify 2.4 a continuous emission can be considered as a series of puffs with infinitely small emission time, which move with mean wind and overlap with each other. For the case of a stationary state ($\partial C/\partial t = 0$) and when the effects of diffusion in x-direction can be considered to be small compared to advection in x-direction, the Gaussian-plume-model can be derived (Hanna et al., 1982; Zenger, 1998):

$$C(x,y,z) = \frac{Q}{2\pi U\sigma_y\sigma_z} \cdot \exp\left(-\frac{y^2}{2\sigma_y^2}\right) \cdot \left[exp\left(-\frac{(z-H)^2}{2\sigma_z^2}\right) + exp\left(-\frac{(z+H)^2}{2\sigma_z^2}\right)\right] \tag{2.5}$$

where time is not a free variable any more, but connected to the distance from the source via the mean wind speed. The resulting plumes can vary in shape, depending on

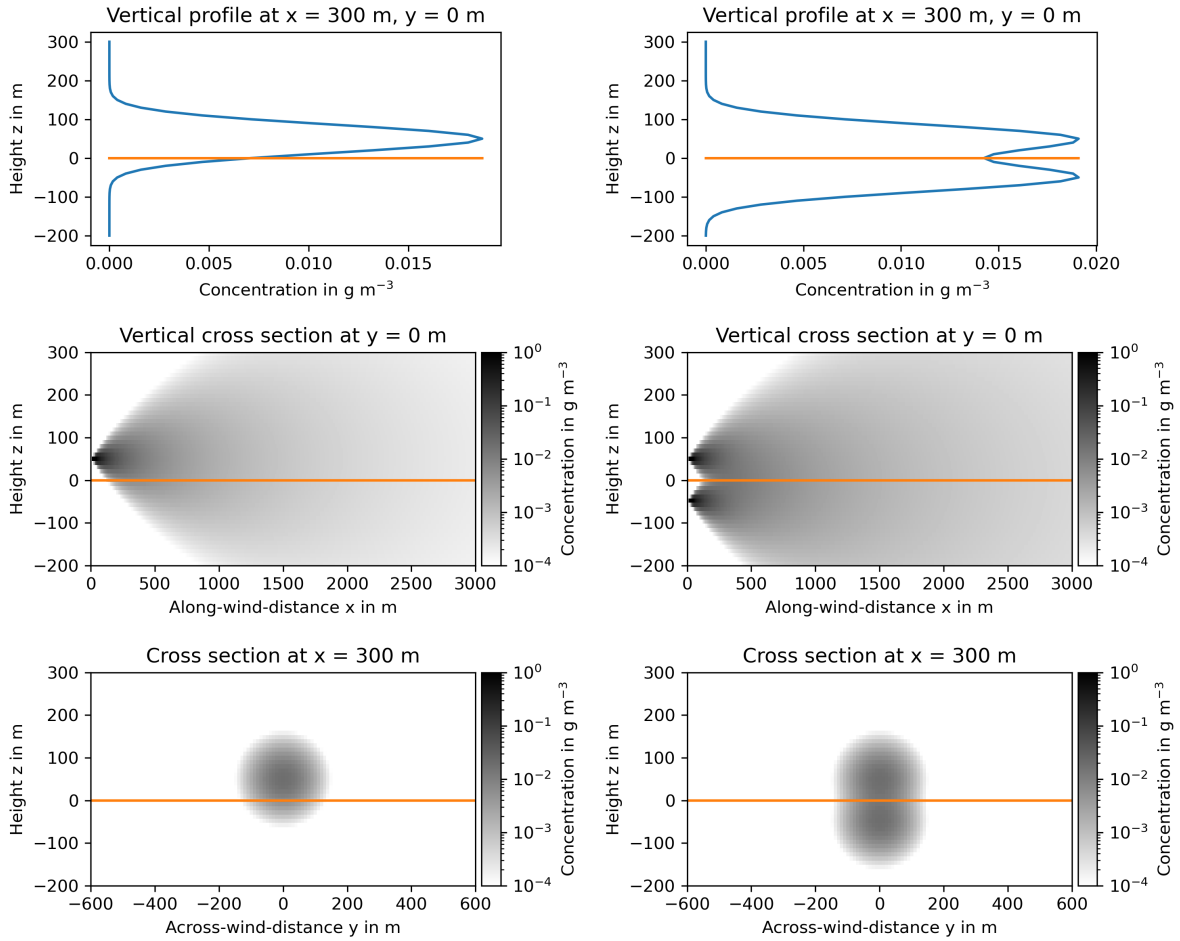

Figure 2.4: Dispersion of a plume of pollutants modelled with a Gaussian-plume-model for a pollutant source at x=0, y=0 and z=50 m under unstable conditions (stability class B). The plots on the left show the model approach without considering reflection at the surface. The plots on the right show the same situation, but now the reflection at the surface is considered by the use of a second identical source at $z = -H$.

Table 2.2: Atmospheric stability classification scheme based on surface wind speed and solar insulation for day time conditions and cloud cover during night time conditions (Pasquill, 1968). Ranging from very unstable (A) to moderately stable (E).

Surface wind speed 10 m a.g.l. ($m\,s^{-1}$)	Daytime solar radiation			Night time cloud cover	
	Strong	Moderate	Slight	>= 4/8 clouds	<= 3/8 clouds
< 2	A	A - B	B	-	-
2-3	A - B	B	C	E	F
3-4	B	B - C	C	D	E
4-6	C	C - D	D	D	D
> 6	C	D	D	D	D

the atmospheric stability. Under stable conditions, the plume disperses more horizontally than vertically, while under unstable conditions the plume also has a large vertical extent. The atmospheric stability is considered within the dispersion parameters (σ) used in the model. The dispersion parameters are chosen according to the wind speed and incoming solar radiation (during day) or cloud cover (during night) at the modelled site. Table 2.2 shows a simple classification scheme for the stability classes and Table 2.3 shows the respective dispersion parameters. Some examples for plumes modelled by a Gaussian-plume model for different stability classes are shown in Figures 2.7, 2.8 and 2.9.

The plumes modelled by Gaussian-plume and Gaussian-puff models are smooth and represent the time averaged plume. Real plumes are much more variable and irregular, and also evolve with time, because of the turbulence within the plume. Averaging the observations of a plume emitted by stack would result in a smooth plume, similar to the results obtained from the Gaussian-plume or Gaussian-puff models. Consequently, these models can only be used as an approximation for short time scales, and only for long time scales and stationary conditions, the models resemble the average plume. However, the model is still useful, as it agrees with experimental data, is fairly easy to use and consistent with the random nature of turbulence (Hanna et al., 1982). For more detailed analysis of the turbulent flow within a plume and for modelling purposes nowadays Lagrangian particle models and Large Eddy Simulations (LES) are used. A description of these models is beyond the scope of this thesis.

Gaussian-plume and Gaussian-puff models use several simplifications to model atmospheric dispersion. The different dispersion parameters (σ) parameters to describe the dispersion in the spatial directions, are considered to be constant with time and space, which leads to an increase of those parameters proportional to $\sqrt{t}$, which for small t is in contrast to observations. To overcome this, empirical dispersion parameters can be used, consequently this approach is not an analytical solution of equation 2.1 any more (Zenger,

Table 2.3: Atmospheric dispersion parameters σ_y and σ_z for different stability classes in dependence of distance (x) from source in meter. For the puff model σ_x is assumed to be identical to σ_y. For intermediate cases such as A - B the average of both values has been taken (Briggs, 1973).

Stability class	$\sigma_y(x)$	$\sigma_z(x)$
	open country	
A	$0.22x(1+0.0001x)^{-0.5}$	$0.20x$
B	$0.16x(1+0.0001x)^{-0.5}$	$0.12x$
C	$0.11x(1+0.0001x)^{-0.5}$	$0.08x(1+0.0002x)^{-0.5}$
D	$0.08x(1+0.0001x)^{-0.5}$	$0.06x(1+0.0015x)^{-0.5}$
E	$0.06x(1+0.0001x)^{-0.5}$	$0.03x(1+0.0003x)^{-0.5}$
F	$0.04x(1+0.0001x)^{-0.5}$	$0.016x(1+0.0003x)^{-0.5}$
	urban environment	
A	$0.32x(1+0.0004x)^{-0.5}$	$0.24x(1+0.001x)^{-0.5}$
B	$0.32x(1+0.0004x)^{-0.5}$	$0.24x(1+0.001x)^{-0.5}$
C	$0.22x(1+0.0004x)^{-0.5}$	$0.2x$
D	$0.16x(1+0.0004x)^{-0.5}$	$0.14x(1+0.003x)^{-0.5}$
E	$0.11x(1+0.0004x)^{-0.5}$	$0.08x(1+0.00015x)^{-0.5}$
F	$0.11x(1+0.0004x)^{-0.5}$	$0.08x(1+0.00015x)^{-0.5}$

Figure 2.5: Plume of a power plant in Bremen.

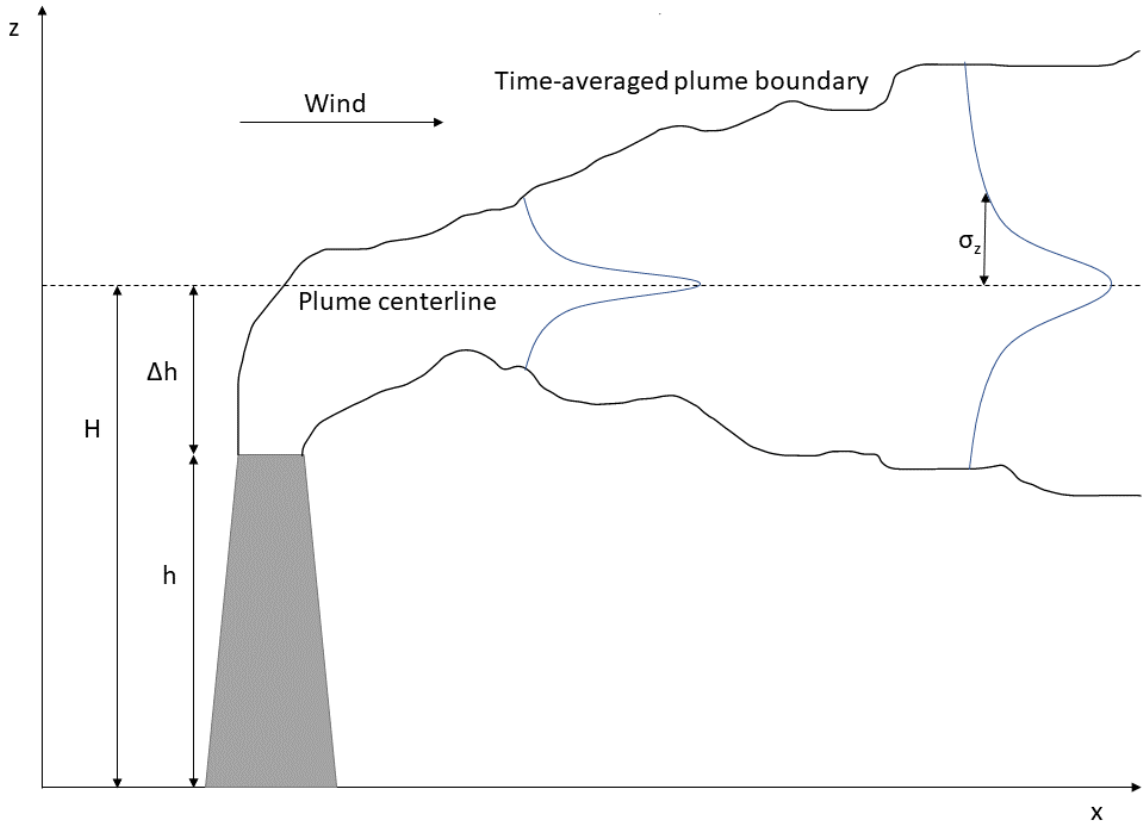

Figure 2.6: Sketch of plume dispersion idealised within a Gaussian-plume-model. H is the effective stack height, which is the sum of the stack height (h) and an additional plume rise term (Δh). The shape of the plume can be approximated by Gaussian distributions where the mean is at the plume centerline ($z = H$). The plume broadens with distance to the source according to the standard deviations of the Gaussian distributions (only shown for the z-coordinate as σ_z).

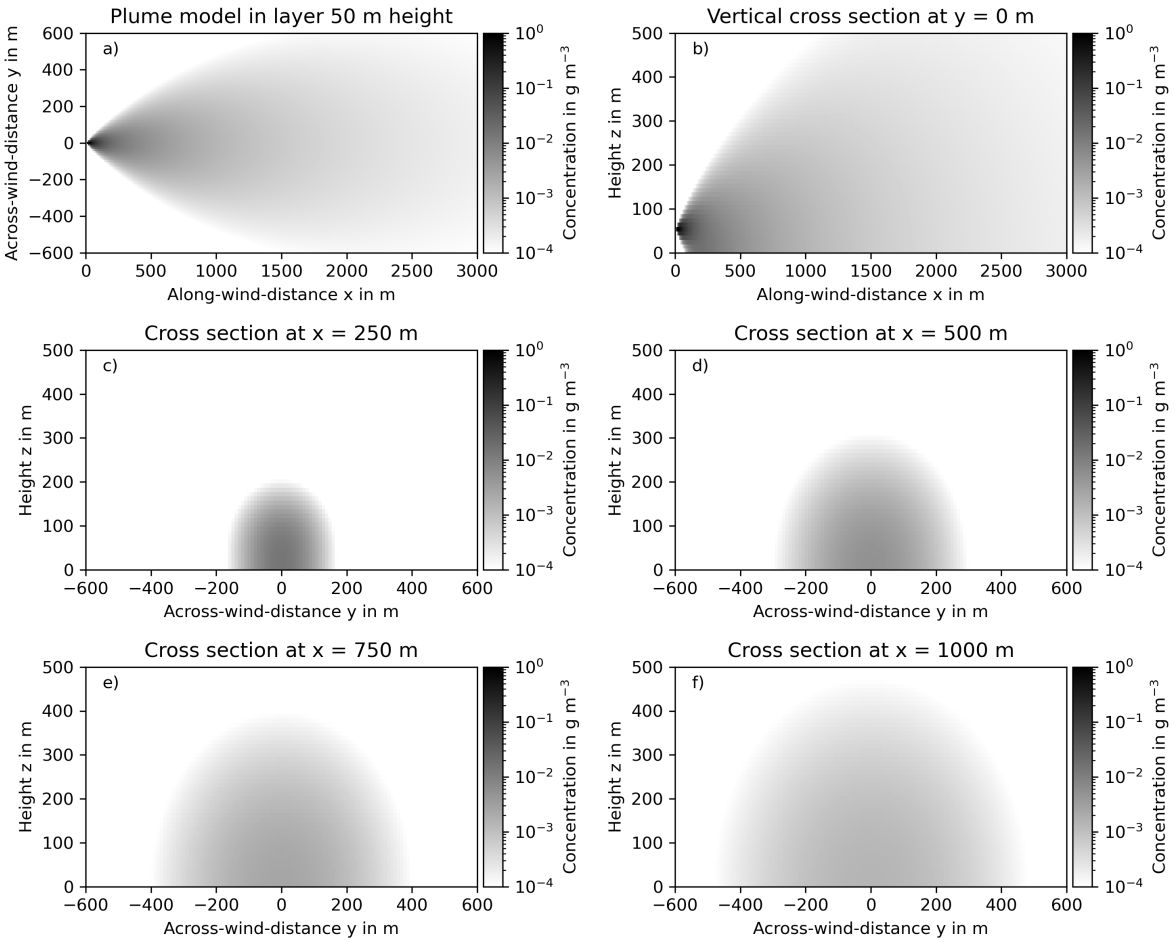

Figure 2.7: Dispersion of a plume of pollutants modelled with a Gaussian-plume-model for a pollutant source at x=0, y=0 and z=50 m under unstable conditions (stability class A). Panel a) shows a horizontal slice through the plume. Panel b) shows the vertical profile of the plume at y=0. Panels c) to f) show cross sections through the plume in the yz-plane at different distances to the source.

1998). Additionally, σ are dependent on the modelled height, because the turbulent diffusion coefficients increase with height, where more eddies contribute to the turbulence (Zenger, 1998). Furthermore, the dispersion parameters can only be considered constant in homogeneous flat terrain. In areas with complex topographies and differences in surface roughness these assumptions are violated. Also the assumption of an homogeneous wind field is a simplification, in reality, the wind field can be more complex due to channelling effects or local variations in the wind field, e.g. around large buildings.

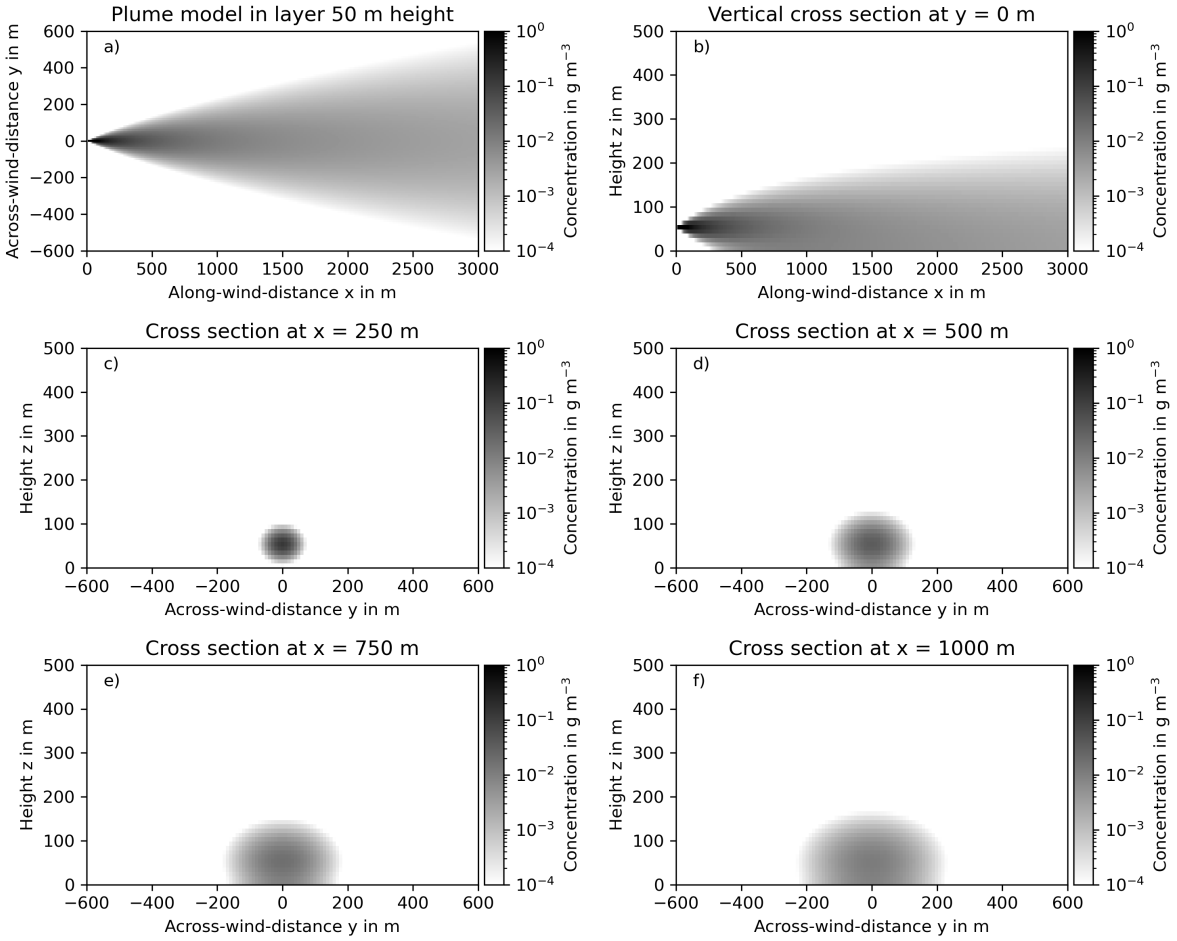

Figure 2.8: Dispersion of a plume of pollutants modelled with a Gaussian-plume-model for a pollutant source at x=0, y=0 and z=50 m under neutral conditions (stability class D). Panel a) shows a horizontal slice through the plume. Panel b) shows the vertical profile of the plume at y=0. Panels c) to f) show cross sections through the plume in the yz-plane at different distances to the source.

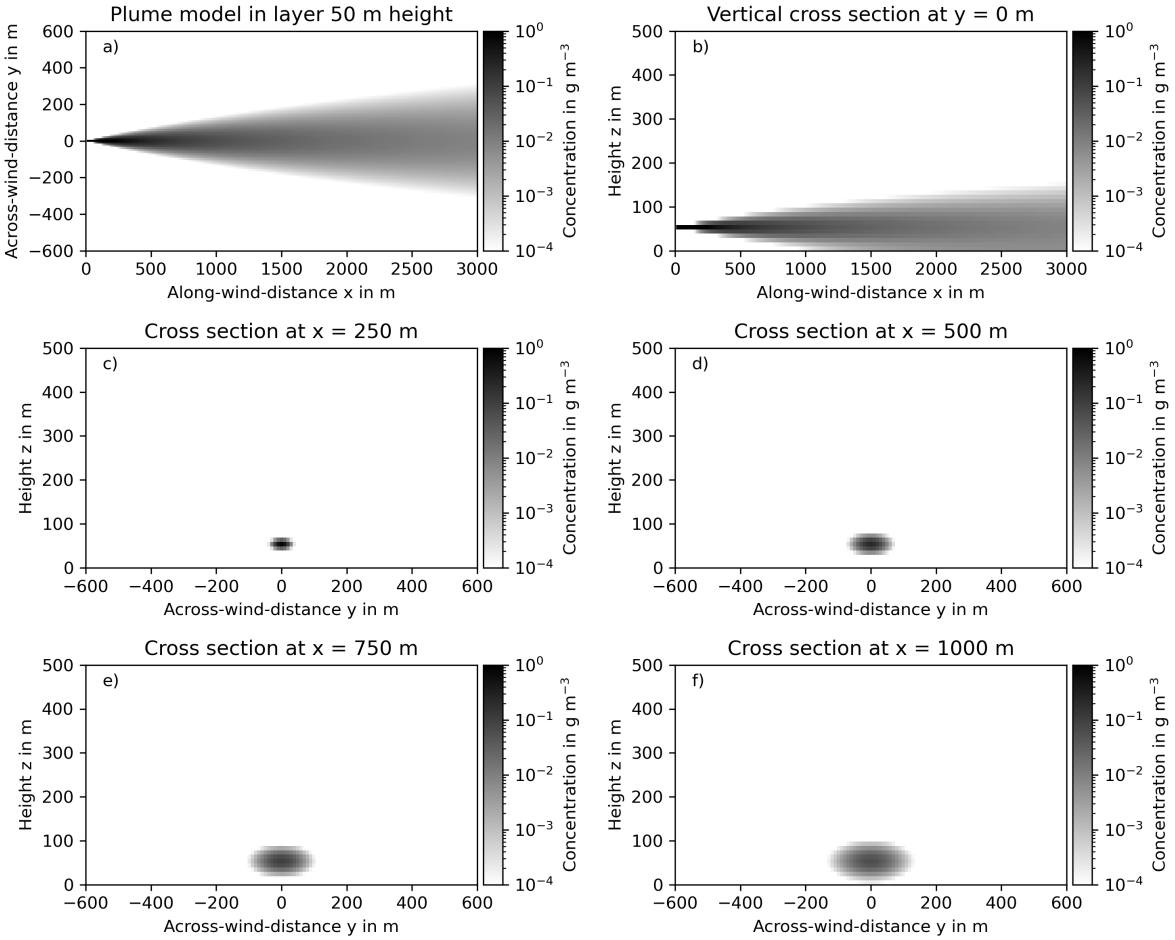

Figure 2.9: Dispersion of a plume of pollutants modelled with a Gaussian-plume-model for a pollutant source at x=0, y=0 and z=50 m under stable conditions (stability class F). Panel a) shows a horizontal slice through the plume. Panel b) shows the vertical profile of the plume at y=0. Panels c) to f) show cross sections through the plume in the yz-plane at different distances to the source.

3 Shipping

Shipping has always been an important way to transport goods around the world. Since 1970 the freight statistics show that the total amount of transported goods by ship has more than quadrupled (Löschke, 2021). Today, approximately 80 to 90 % of the world trade is transported by ships, which corresponds to approximately 11.1 billion tons of cargo or 811 million Twenty-foot Equivalent Units (TEU)[1] in the year 2019 (UNCTAD, 2021). For the year 2020 this slightly decreased to 10.6 billion tons of cargo, due to the COVID-19 pandemic (UNCTAD, 2022c).

The main shipping routes span from East Asia to Europe and the United States. For one third of the worldwide ship traffic, the port of departure or port of destination lies within the EU. In 2020, 66 % of all transported goods were discharged in ports in Asia, while only 41 % were loaded in Asian ports (UNCTAD, 2022c). Historically, the transport patterns were still as in colonial times, developing nations would export large amounts of resources and raw materials and only import a relatively small amount of consumer goods. This changed approximately 20 years ago and many of the developing countries now also import raw materials and participate in the trade of end products (Löschke, 2021).

The global shipping fleet is increasing in size every year since 1990, with the highest growth rate around 2010. Between 2000 and 2020, the available freight volume has more than doubled. At the beginning of 2021 approximately 99800 sea ships with a gross tonnage above 100 tons were operating around the globe, with a total carrying capacity of about 2.13 billion dead-weight tons.

About 42 percent of the whole fleet is older than 20 years, 10 % is between 15 to 19 years old and only 11 % is younger than 4 years. The age distribution varies between different countries, older ships are generally those in the least developed countries. Generally, the ageing of the fleet is a concern, as older ships are less efficient and generate higher emissions. Also, the average size of the ships increased throughout the years. The number of mega-container ships (container capacity greater than 10000 TEU) rose from 6 % in 2011 to almost 40 % in 2021 (UNCTAD, 2022a).

In addition to the merchant fleet, the number of cruise ships also increased and since the 1990s, cruise ship tourism has become the fastest growing travelling sector (Löschke, 2021). International cruise tourism increased from 3.8 million passengers in 1990 to 28.5

[1] TEU is the standard-sized metal container used to transport goods.

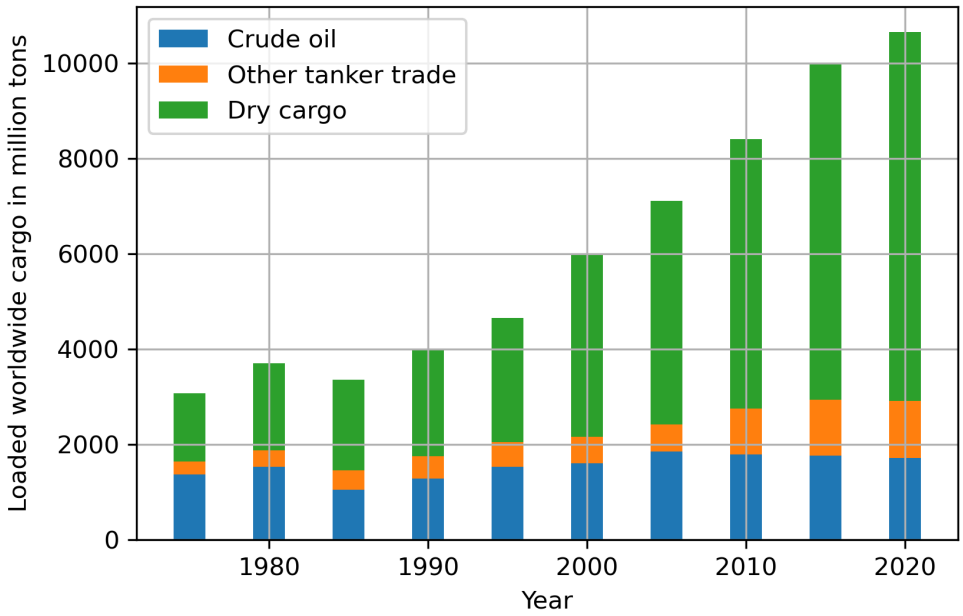

Figure 3.1: Historical development of transported worldwide cargo by type. Dry cargo is defined as cargo that is usually not carried in tanker, e.g. coal, ores, grains, pallets, bags, crates and containers. Other tanker trade refers to all trades usually carried in tankers except of crude oil, e.g. refined petroleum products, gases and chemicals. Numbers taken from (UNCTAD, 2022c).

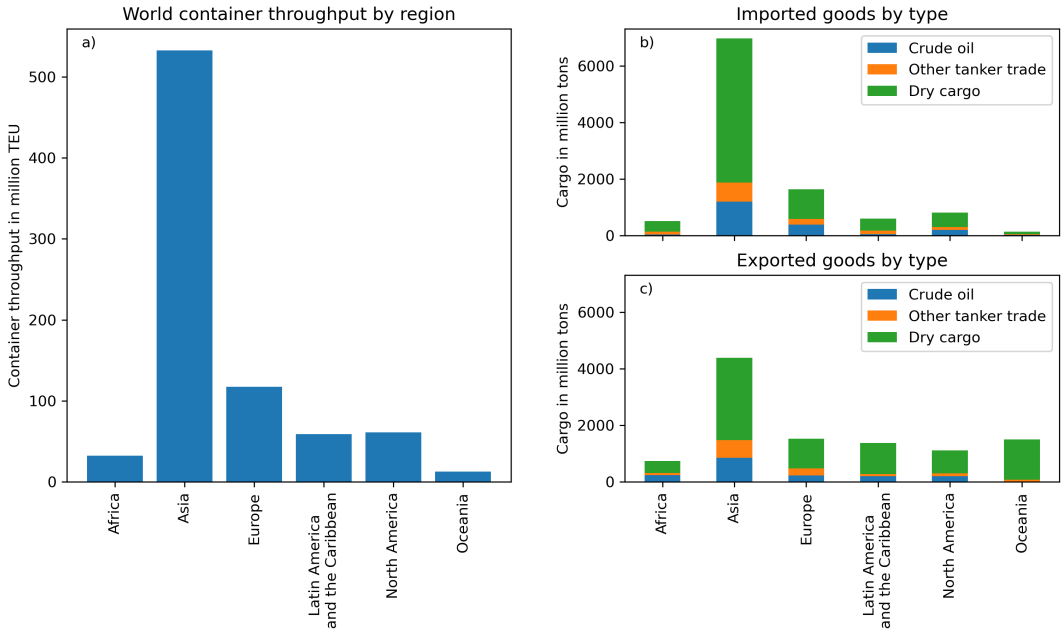

Figure 3.2: Transported worldwide cargo by type and region in 2020. Imported goods are goods discharged and exported goods are goods loaded in the region. Dry cargo is defined as cargo that is usually not carried in tanker, e.g. coal, ores, grains, pallets, bags, crates and containers. Other tanker trade refers to all trades usually carried in tankers except of crude oil, e.g. refined petroleum products, gases and chemicals. Numbers taken from (UNCTAD, 2022a).

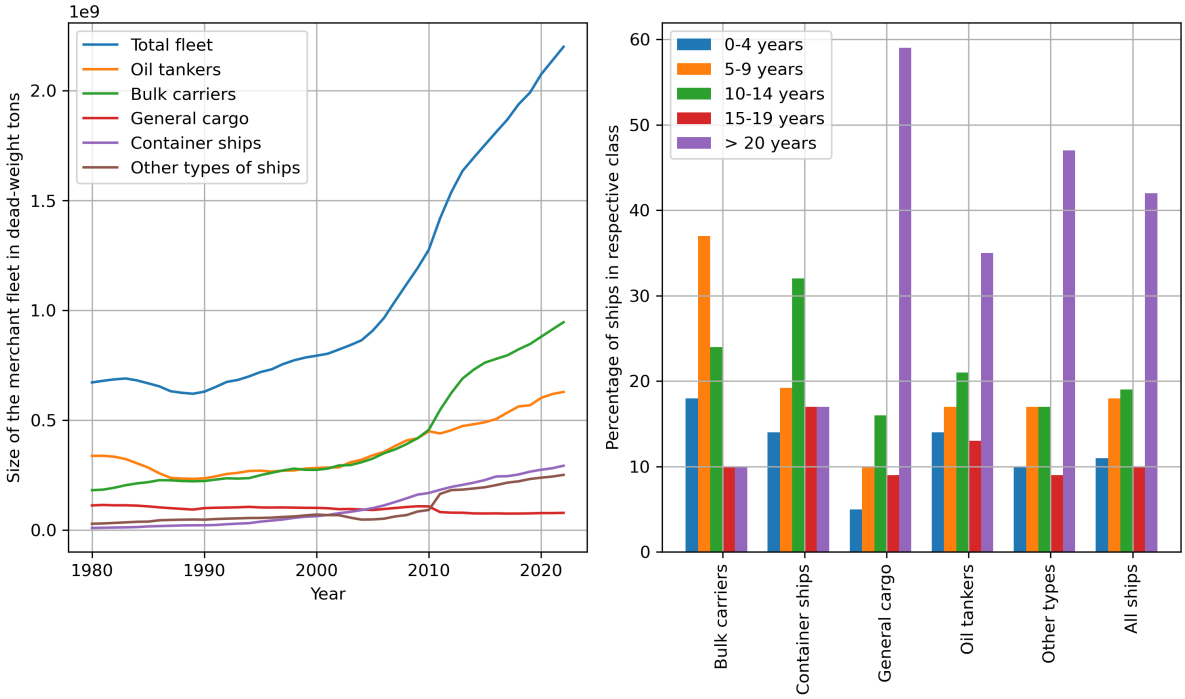

Figure 3.3: Size of the merchant fleet (all ships above a gross tonnage of 100 tons) as a function of time and age of ships for different ship types. Numbers taken from (UNCTAD, 2022a)

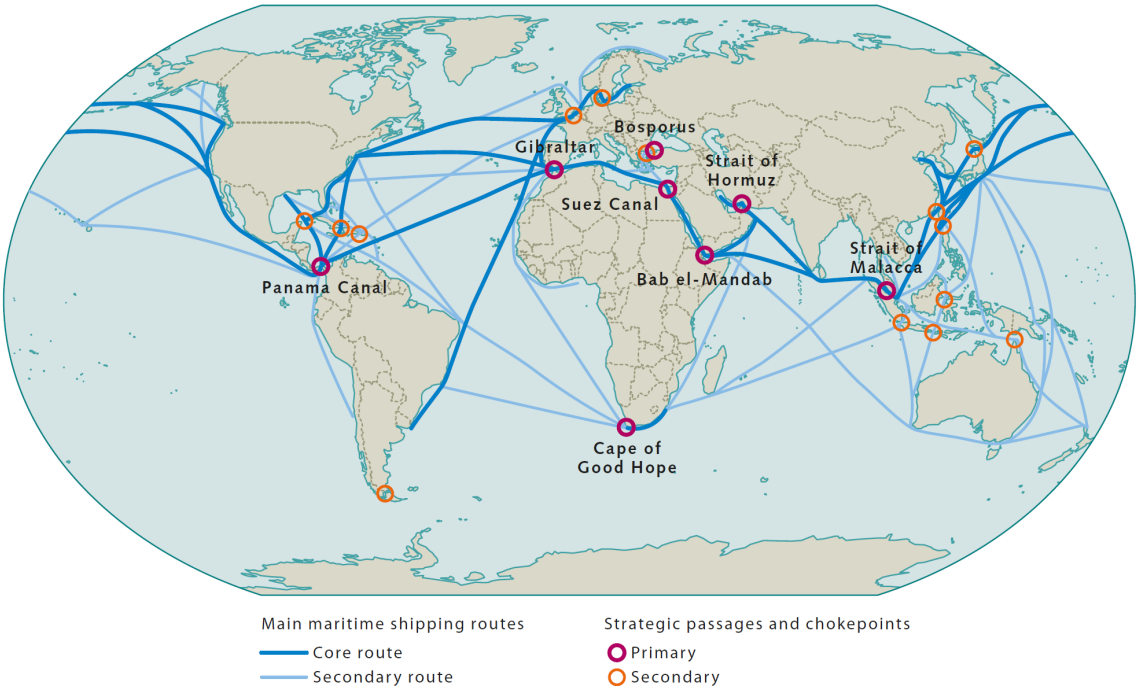

Figure 3.4: Map of the most important shipping routes taken from Löschke (2021).

million in 2018 and continued to grow until the COVID-19 pandemic, where the number of passengers fell to about 7 million in 2020. Primary operating areas are the Mediterranean and Caribbean Seas, but there was a significant increase in Asia, Europe and the polar regions until 2020 (Löschke, 2021).
Inland shipping plays a different role and is in direct competition with rail and road transport. In the EU road transport accounts for about 75 % of the whole inland freight transport, while rail accounted for 18.7 % and inland waterway transport for about 6 % in 2018 (Attivissimo et al., 2020). Looking at individual EU countries, the shares can be different, for example in the Netherlands, approximately 42 % of transport happens on the inland waterways, whereas in Lithuania and Latvia railway transport dominates, with shares of 64.7 % and 56 %, respectively. Belgium, Germany, France, the Netherlands and Romania account for approximately 92 % of the transported goods on waterways within the whole EU. Each year approximately 800 million tons of cargo are transported on the waterways of these country. The cargo consists mostly of metal ores, coke and refined petroleum products, chemicals, rubber, plastic and nuclear fuel (Attivissimo et al., 2020). Since 2018 there is a slight decline in the total number of transported goods. In 2018 this was attributed to the low water levels in the second half of the year, in 2019 to the slowed down world trade because of tariffs on grain, steel, cars and a general reduction of industrial production and in 2020 due to the impacts of the COVID-19 pandemic (Kriedel et al., 2019, 2020, 2021).

3.1 Ship emissions

For most of the history of mankind sailing ships were used for transport. In the 19th century a transition to coal powered steam ships and in the 20th century to ships using fuels from crude oils has taken place. With the change from sailing ships to fossil fuels, shipping also became one of the major sources of greenhouse gases and air pollutants. While shipping is a more efficient way of transport than rail, road or air transport, the large number of transported goods leads to a overall high contribution of the shipping sector to the emissions caused by humans. Approximately 932 million tons of CO_2 were emitted by ship traffic in 2015, this corresponds to 2.6 % of the whole CO_2 emission for that year. In 2018 this amount grew to 1056 million tons, which is approximately 2.89 % of the global anthropogenic emissions. Between 2012 and 2018 the dominant source of the greenhouse gas (GHG) emissions of shipping were container ships, bulk carriers and oil tankers. Other important ship types were chemical tankers, general cargo ships and liquefied gas tankers, in total these six ship types accounted for 86.5 % of the total GHG emissions caused by shipping (Faber et al., 2021). The primary demand for energy on ships is used for propulsion. For some ship types, e.g. cruise ships, refrigerated bulk cargo ships and fishing ships, the auxiliary energy demand can be as high as the energy

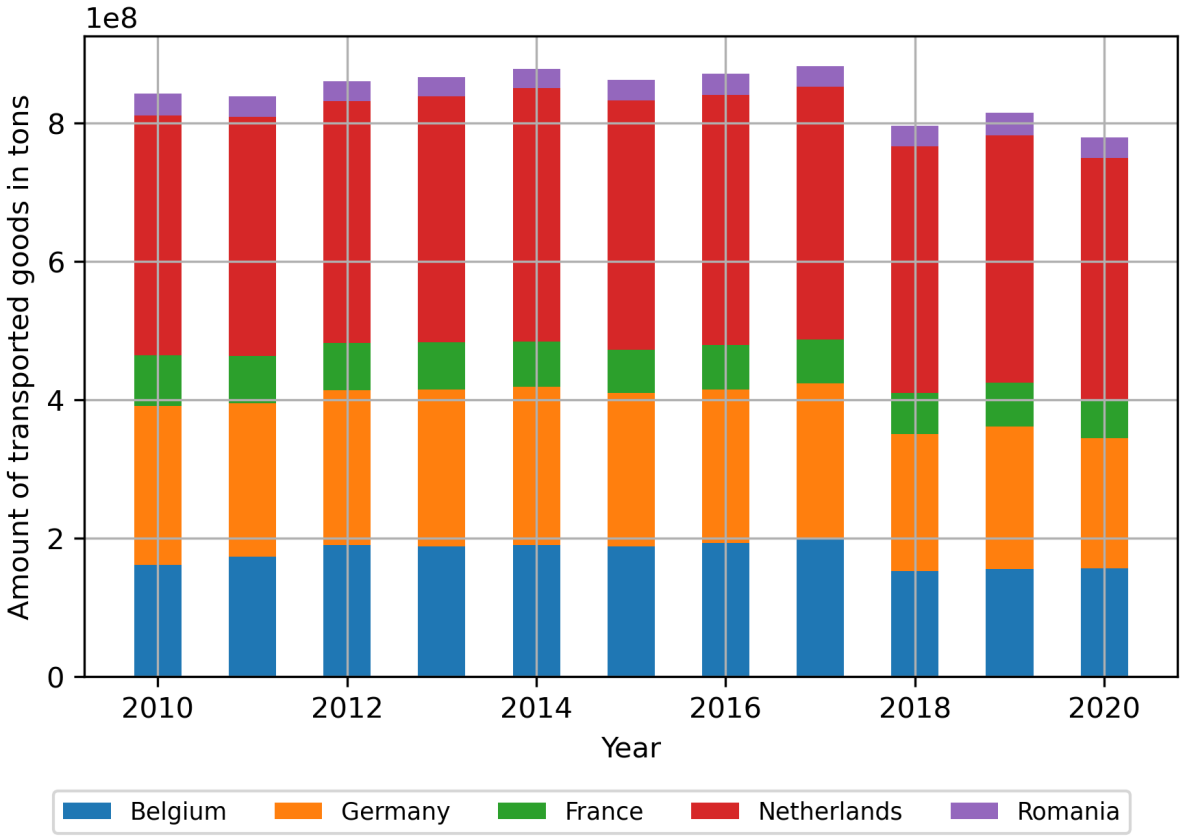

Figure 3.5: Amount of goods transported on inland waterways in the EU. The five countries shown account for 92 % of all inland waterway cargo in the EU.

demand for propulsion (Faber et al., 2021). The average ship size and installed engine power increases, resulting in higher fuel consumption per ship. At the same time the increase in fuel consumption was lower from 2012 to 2018 compared to the increase in installed engine power. This can be attributed to a general trend of continued reduction in operating speeds and reduction in the average number of days at sea (Faber et al., 2021; Smith et al., 2015). As operating speeds are not fixed by the technical specifications they are highly susceptible to the fluctuation of the market. The operating speeds therefore remain one of the main drivers for the emission growth and are highly uncertain. A lower speed also reduces the amount of emitted pollutants (Boersma et al., 2015).
Additionally to the emission of GHG shipping is also a source of SO_2, NO_x, black carbon, volatile organic compounds (VOC), PM and other pollutants which influences human health and the environment. Most emissions caused by international shipping take place within 400 km of land and therefore have an impact on coastal air quality and human health (Corbett et al., 1999; Eyring et al., 2010).
The SO_2 emissions of ships stem from the sulphur contained in the burnt fuel. Traditionally sea ships use heavy fuel oil (HFO), which is a viscous waste material of the refinery process of crude oil. Heavy fuel oil is rich in heavy metals, sulphur, aromatic and polycyclic hydrocarbons. In order to be used as fuel, HFO needs to be warmed and cleaned of metals, which requires additional processing steps and energy on board the ships. In 2018 HFO contributed 79 % of the total fuel consumption of ships by energy content (Faber et al., 2021)
Alternative fuels to HFO exist, e.g. Marine diesel oil (MDO), biofuels, liquefied gases, hydrogen and alcohols. These fuels have a lower fuel sulphur content than HFO and therefore decrease the SO_2 emissions by shipping. Liquefied natural gas (LNG) as a fuel for ships has shown its potential in decreasing the CO_2 emissions by 20 %, NO_x emissions by up to 85 % and particle emissions up to 99 % compared to regular HFO usage. At the same time LNG consists of methane which has a higher greenhouse effect than CO_2 and when used on a large scale for the whole shipping industry, leakages in the LNG supply could increase the global warming effect of the shipping industry. For short distances, such transportation on inland waters or in coastal regions, electric motors are also viable. In general, all the alternative fuels are more expensive than HFO and in most cases they have a lower energy density per volume (see Figure 3.6). Also, currently many ports lack the infrastructure to provide sufficient volumes for commercial use.

3.2 Regulations for sea ships

The emissions of NO_x and SO_2 of sea going ships are limited by the International Maritime Organization (IMO) MARPOL Annex VI protocol (International Maritime Organization, 1998), which defined limits for the fuel sulphur content (in % m/m) and NO_x engine power

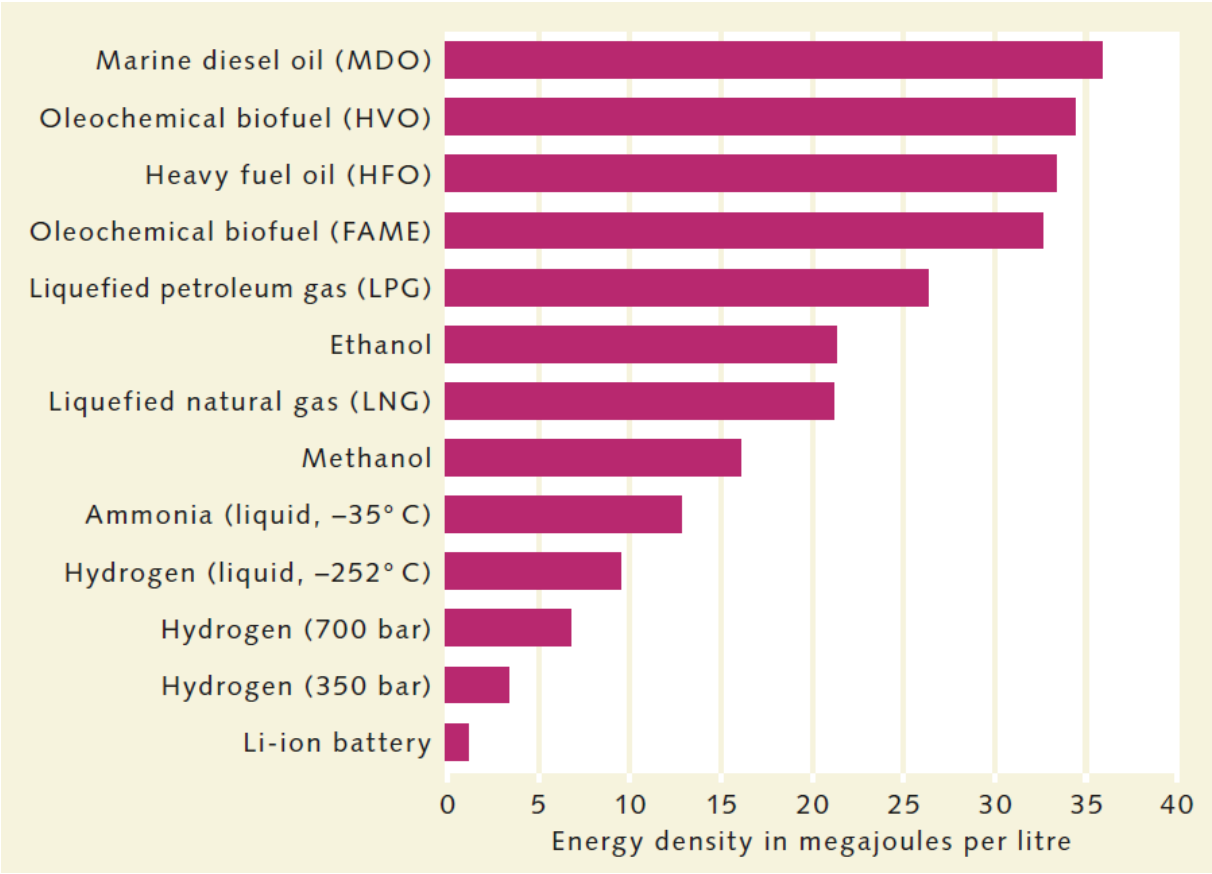

Figure 3.6: Energy density of different fuel types. Taken from Löschke (2021).

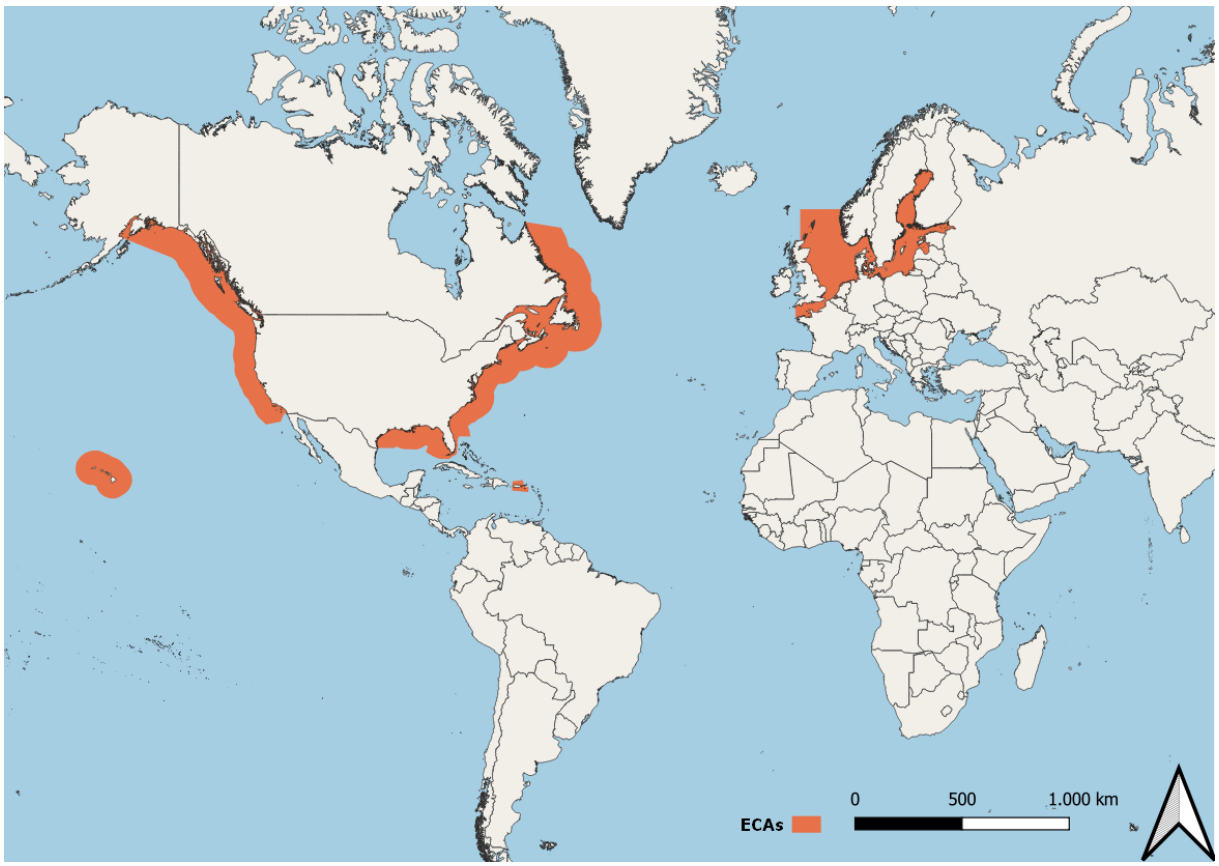

Figure 3.7: Existing emission control areas (ECAs) established by the IMO. Base map from European Commission, Eurostat (ESTAT), GISCO (2020).

weighted emission rate. Annex VI entered into force in May 2005 and was revised in 2010, with even stricter regulations. The global limit of the sulphur fuel content was set to 4.5 % in 2005, 3.5 % in 2012 and 0.5 % in 2020. Additionally, emission control areas (ECA) have been established in some regions, enforcing even stricter rules of 1.5 % in 2005, 1.0 % in 2010 and 0.1 % in 2015. The first sulphur emission control area (SECA) was established in the Baltic Sea in 2006, in 2007 the North Sea and the English Channel were designated as SECA as well. In 2012, the coasts of the US and Canada and ultimately in 2014 the coast waters around Puerto Rico and the United States Virgin Islands followed (see Figure 3.7). Additionally to the ECAs established by the IMO, ECAs are also established by countries themselves, e.g. the Chinese government established an ECA around its coastal waters, as well as inland ECAs in the Yangtze River and Xi Jiang River. South Korea also implemented SECAs in specified port areas, e.g. Incheon, Pyeongtaek-Dangjin, Yeosu-Gwangyang, Busan and Ulsan. To comply with the sulphur fuel content regulations, alternative fuels with a low sulphur content have to be used. Alternatively, as the ultimate goal is the reduction of SO_2 emissions, ships can also be equipped with scrubber systems to remove sulphur compounds from the exhaust gases. There are different kinds of scrubbers systems. Dry scrubbers use chalk granulate to remove the SO_2 molecules from the exhaust gas stream, wet scrubbers use either sea or fresh water to wash out the SO_2.

PM is not directly regulated, but indirectly by the SO_2 regulations, as SO_2 has an influence on particle formation.

Most of the NO_x formed during combustion consists of atmospheric nitrogen and oxygen and only a minor part stems from nitrogen compounds that are present in the fuel. The amount of NO_x formed is temperature dependent and higher temperatures lead to higher amounts of NO_x. The combustion temperature is related to the rotational speed of the engine crankshaft, i.e. the crankshaft revolutions per minute. The MARPOL Annex VI regulations are therefore also related to the rotational speed of the engine (Table 3.1). The NO_x limits are separated into different levels (Tiers) of control, based on the date of the ship construction. While Tier I and II apply globally, Tier III only applies in ECAs. Nowadays all emission control areas also enforce the Tier 3 NO_x limits, but the Baltic Sea NECA and North Sea NECA have been delayed for several years and only came into effect in January 2021.

To survey the CO_2 emissions, the IMO implemented an amendment to MARPOL Annex VI in 2018. Ships of a size of 5000 gross tonnage or above are required to submit data on the ship type, their size, power output of all (main and auxiliary) engines, fuel consumption and type of consumed fuel, as well as methods used for determining fuel consumption to the states they are registered in. This data is then subsequently transferred to the IMO Ship Fuel Oil Consumption Database, for each calendar year. In 2015 the EU already implemented a similar, but more detailed system, for all ships entering or leaving EU harbours (European Parliament and European Council, 2015).

The IMO has set a target to reduce the overall GHG emissions by 50 % and the CO_2 emissions by 70 % compared to the emissions of 2008, until the year 2050. To reduce the GHG emissions of ships, the International Maritime Organization (IMO) implemented the Energy Efficiency Design Index (EEDI) and the Ship Energy Efficiency Management Plan (SEEMP). The EEDI is a technical measure for new ships, that promotes the use of energy efficient equipment. It requires a minimum energy efficiency level per capacity mile for different ship types. Starting from 1 January 2013 new ships need to meet the reference level for their ship type. The choice of technologies used to achieve the goals is up to the ship designers and builders. The requirements are tightened every five years.

The SEEMP is an operational measure, that aims to improve the energy efficiency of existing ships. These measures include guidelines and tools for fuel efficiency for example through optimizing the speed of the vessel and optimizing shipping routes, as well as installation of energy recovery methods or hull cleaning. Energy recovery installations aim to improve the efficiency of the engine and reduce the amount of energy lost by heat transfer, while hull cleaning reduces the friction of the ship's hull in water. Also more unconventional methods to decrease the fuel consumption are tested, e.g. the shipping company Maersk installed Flettner rotors on one of their tankers, which are vertically installed rotating cylinders on the ships deck. Wind flowing past these turning cylinders

Table 3.1: NO_x emission limits according to MARPOL Annex VI.

Tier	Ship construction date	Total weighted cycle emission limit ($g\,kWh^{-1}$) n = engine's rated speed (rpm)		
		n < 130	n = 130 - 1999	n ≥ 2000
I	1 January 2000	17.0	$45n^{-0.2}$	9.8
II	1 January 2011	14.4	$44n^{-0.23}$	7.7
III	1 January 2016	3.4	$9n^{-0.2}$	2.0

Table 3.2: Overview of NO_x emission limits, according to CCNR (CCNR, 2020) and EU regulations (European Parliament and European Council, 2016), in both cases given in units of $g\,kWh^{-1}$.

Regulation	in effect since	Engine power (kW)	NO_x+HC ($g\,kWh^{-1}$)
CCNR I	2002	P > 130	9.2
CCNR II	2007	P > 130	6.0
EU RL2016/1629	2019	130 < P < 300	2.1
EU RL2016/1629	2019	P > 300	1.8

propels the ship at right angles to the wind. In the first year after the installation these rotors helped to reduce the fuel consumption by 8.2 % (Löschke, 2021).

3.3 Regulations for inland ships

There are also regulations specifically aimed at the reduction of the emissions of inland ships. In Europe, the first regulations were implemented by EU Directive 97/68/EC (European Parliament and European Council, 1998), later superseded by EU Regulation 2016/1628 (European Parliament and European Council, 2016). Additionally, other agreements between states can apply, for example the Central Commission for Navigation on the Rhine (CCNR) is an international organisation which is enabled to address issues concerning inland navigation on the Rhine. The fuel sulphur content for inland ships is limited to 0.001 %, which is the same as for diesel fuel used by trucks. The NO_x emissions are regulated in a similar manner to the NO_x regulations for sea ships. Regulations only apply for new engines, i.e. new ship construction or replacement of older engines. Engines already in service are subject of grandfathering, which means they do not have to comply with new regulations but only with the ones already in place for their year of construction. Table 3.2 gives an overview over the combined NO_x and hydrocarbon (HC) emission regulations. NO_x and hydrocarbons are combined for simplicity, as often used chemiluminescence sensors for NO_x have cross sensitivity to hydrocarbons. PM emission are regulated in a similar manner to the NO_x emissions and also depend on installed engine power.

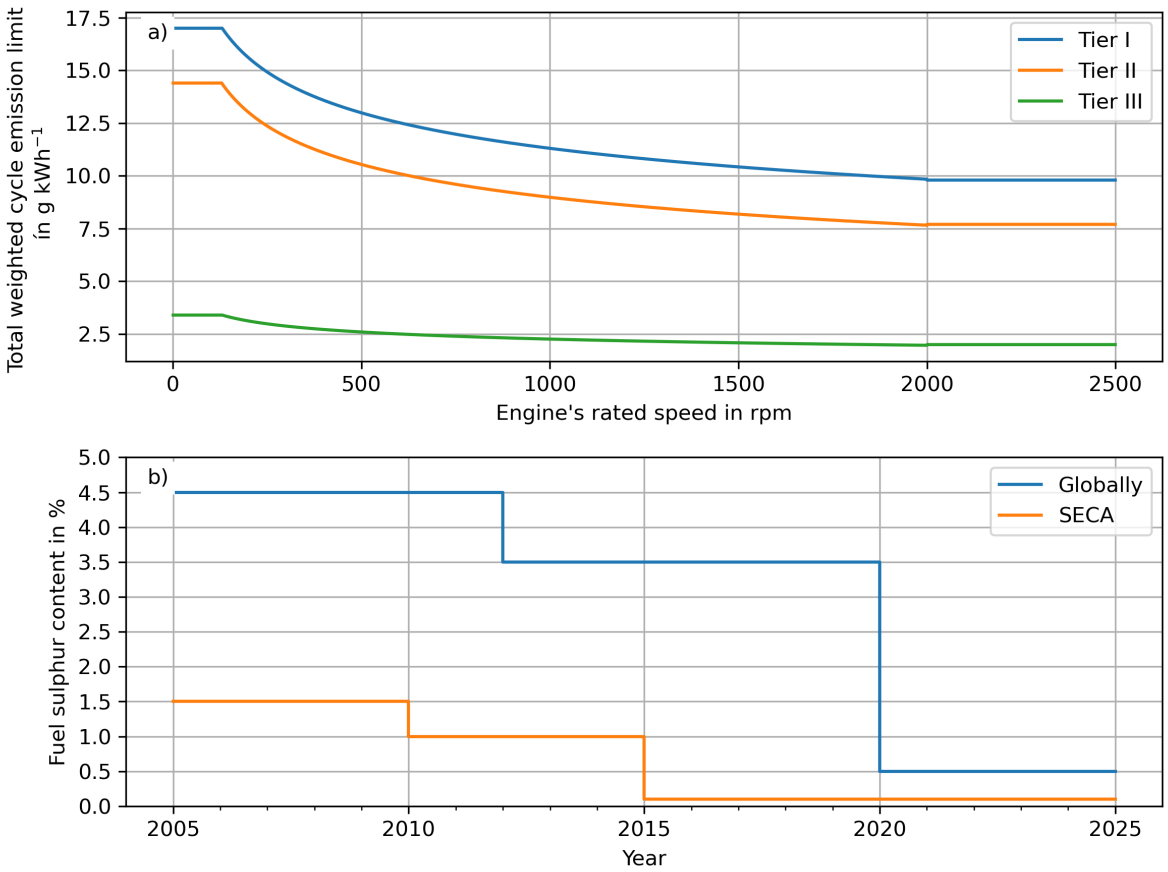

Figure 3.8: a) NO_x emission limits as a function of engine's rated speed according to MARPOL ANNEX VI. b) Fuel sulphur content limits inside emission control areas and globally.

3.4 Studies and measurements of ship emissions

In the past years, the focus point of studies regarding ship emission measurements were the SO_2 emissions and the compliance with the fuel sulphur content limits, but also studies investigating NO_x and PM were undertaken.

One of the most common approaches to study ship emissions is the use of in-situ instruments, where air is sucked into the instrument and analysed for specific trace gases. These instruments can be used in various ways, e.g. the instrument can be set up on the shoreline downwind of a shipping lane and measure the ship plumes which are transported by the wind towards the measurement site. These measurements can then be used to determine emission factors for ships. Emission factors are a coefficient which describes the rate a which a pollutant is released into the atmosphere by a certain activity, e.g. the amount of NO_x emitted per kg of burnt fuel.

Diesch et al. (2013) used in-situ instruments at the river Elbe close to Hamburg, Germany, to investigate ship emissions of passing vessels. During five days of measurements 139 ship plumes were identified with sufficient quality, analysed and emission factors for particles, SO_2, NO_x, black carbon, and polycyclic aromatic hydrocarbons (PAH) were determined. The emission factors for particle number and PM_1 mass were found to increase with the fuel sulphur content. Additionally, the emission factors of black carbon, PAH and particle number decrease with gross tonnage, while SO_2, NO, NO_2, NO_x and PM_1 mass concentration were found to increase with gross tonnages.

Kattner et al. (2015) presented an on-shore measurements of ship plumes using in-situ instruments from a measurement site on the Elbe close to Hamburg. A method to calculate the fuel sulphur content out of measured SO_2 and CO_2 was presented and successfully applied to the data. The method proved to be reliable and could easily detect ships that do not comply with fuel sulphur limits.

Kurtenbach et al. (2016) investigated the NO_x, CO_2 and PM emissions of ships on the Rhine in Germany. Again NO_x and CO_2 measurements were combined to derive emission factors in $\mathrm{g\,kg^{-1}}$. An average NO_x emission factor of $54 \pm 4\ \mathrm{g\,kg^{-1}}$ was found and a comparison with the regulations showed, that all investigated ships exceeded the threshold values, while the PM emissions were just below the limits.

Another approach is to directly use in-situ instruments on board of individual vessels. This allows a more detailed analysis of emissions, as measurements can be carried out at different engine speeds and specified conditions. However, this also limits the number of ships that can be surveyed. Zhang et al. (2016) determined emission factors using on-board measurements on three different ships using diesel engines. The measurements showed, that more than 80 % of the emitted NO_x was emitted as NO and that the NO_x emissions are higher at low speed compared to high speed and that acceleration manoeuvres lead to higher emission factors.

Beecken et al. (2014) investigated SO_2, NO_x and particle emissions with airborne measurements using in-situ instruments installed in aircraft. In this study 174 ship plumes of 158 different ships were investigated and an average SO_2 emission factor of 18.8 $\pm$ 6.5 $g\,kg^{-1}$ was found, which corresponds to 1 % fuel sulphur content. The benefit of this airborne approach is that the platform can adjust to changing wind directions and that particles and gases in the plume can be measured at different distances from the ship. The downside are the high cost of operation and the very short time the plumes are measured during the transect flights.

Remote sensing, such as differential optical absorption spectroscopy (DOAS), can also be used to measure and investigate ship emissions.

Seyler et al. (2017) used multi-axis DOAS (MAX-DOAS) to investigate shipping emissions in the German Bight from 2013 to 2016. More than 2000 individual ship plumes were identified and their SO_2/NO_2 emission ratios were determined. On 1 January 2015 a stricter fuel sulphur content limit (from 1 % m/m to 0.1 % m/m) came into action. The average SO_2/NO_2 ratio for 2013 and 2014 was found to be 0.3 and decreased significantly in 2015 and 2016, presumably due to the lower fuel sulphur content limit.

MAX-DOAS retrieves the so called slant column density (SCD), which is the concentration of an absorber integrated along the light path. Consequently, a measurement will not only include a ship plume but also unpolluted atmosphere. Seyler et al. (2019) presented a new application of the so called "onion-peeling" approach in MAX-DOAS measurements. In this approach the different light paths of UV and visible radiation are used to locate the approximate ship plume position and study horizontal inhomogeneities of NO_2 above shipping lanes in the German Bight. Using this approach it was possible to derive in-plume NO_2 volume mixing ratios for ships passing the measurement site at distances of several kilometres.

Another use of DOAS to investigate shipping emissions was presented by Berg et al. (2012), where SO_2 and NO_2 were measured by a DOAS system mounted to an aircraft and a helicopter. From these measurements emission rates (in $kg\,h^{-1}$) were derived. The derived emission factors were analysed and compared to on-board measurements of a passenger ferry and showed good agreement.

Ship emission can not only be measured by ground based or airborne remote sensing, but also by satellites. NO_2 measurements of different satellites allow to observe global shipping ways. For example GOME allowed to observe shipping in the Indian Ocean (Beirle, 2004), SCIAMACHY enabled observations in the Indian Ocean and the Red Sea (Richter et al., 2004). Additional ship tracks were identified in GOME-2 data (Richter et al., 2011). With TROPOMIs high spatial resolution, new ship lanes were detected in European waters, which have not been detected with other satellites before (Riess et al., 2022). Generally, the increase in spatial resolution over the past years, increased the capabilities of satellites to detect ship emissions. With TROPOMIs high spatial resolution

it is also possible to detect individual ship plumes from space (Georgoulias et al., 2020). Airborne measurements are not only restricted to instruments on board of aircraft and helicopters, but also unmanned aerial vehicles (UAVs) are used. Use of UAVs decreases the costs compared to larger airborne vehicles and also allows to get closer to the chimney of the ship. Examples for UAV use can be found in Zhou et al. (2019, 2020), where a UAV was used to monitor fuel sulphur content of ships. Measurements were carried out using in-situ instruments and during the measurement procedure the UAV was moved into the plume to measure CO_2 and SO_2, the fuel sulphur content is then calculated.
The influence of shipping emissions on environment and health is often investigated using models, which allow to describe the current state and impact of shipping emissions (e.g., Feng et al., 2019; Tang et al., 2020) or can be used to investigate future scenarios with new regulations and developments in place (e.g., Eyring et al., 2005a; Ramacher et al., 2020).
For these modelling studies, information about the amount of ship traffic and emission factors for different ships is needed. The information is summarized in the form of ship emission inventories, which can be used in chemical transport models. To obtain these inventories, two approaches exist. In the bottom-up approach, ship emissions are characterized from the individual vessel upwards to a higher level of organisation, e.g. the entire commercial merchant fleet (e.g., Corbett et al., 1999; Eyring et al., 2005b; Johansson et al., 2017). In the top-down approach, the order is inverted, e.g. the fleet for a specified harbour is approximated by the knowledge of the emission behaviour of the global shipping fleet. In both cases, knowledge about emission factors and traffic statistics is needed.
The implementation of regulations does not necessarily lead to a decrease of the total emissions. Faber et al. (2021) reported that from 2012 to 2018 the regulations for sea ships had mixed results on a global scale. The overall NO_x emissions increased at a lower rate than the fuel consumption, which means less NO_x was emitted per amount of burnt fuel. This was found to be consistent with the increased number of ships that comply with Tier II and Tier III regulations. However in total the NO_x emissions still increased, as the total amount of burnt fuel also increased. At the same time the global SO_x and PM emissions increased, even though more SECA were designated throughout this time. This was attributed to the increase in average fuel sulphur content in HFO, which at that time could still be used outside of SECAs. In total this increase outweighed the reduction achieved within the SECAs. Also in most cases MDO and LNG were used in SECAs to comply with the regulations, but in turn this increased the overall methane emissions of shipping by 87 %.

4 Differential optical absorption spectroscopy

4.1 Absorption spectroscopy

Atmospheric absorption spectroscopy is based on Lambert-Beer's law, which describes the absorption of electromagnetic radiation by matter:

$$I(\lambda) = I_0(\lambda) \cdot exp(-\sigma(\lambda) \cdot c \cdot L), \tag{4.1}$$

where $I(\lambda)$ is the intensity of light after passing through a medium of thickness L, $I_0(\lambda)$ is the intensity of the light source, $\sigma(\lambda)$ is the absorption cross-section at a given wavelength λ and c the concentration of the absorber present in the medium. Molecules can exist in different states, ground state and excited states, e.g. electronic, vibrational and rotational excited states. Excited states can be entered by absorbing electromagnetic radiation. The energy levels of the excited states depend on the molecule type and consequently, each molecule absorbs electromagnetic radiation at different wavelengths.

4.2 Basic principle of DOAS

In the atmosphere, the intensity of light is not only reduced by absorption of a single species but by absorption of several species. Additionally, the light is scattered and two types of broadband scattering can be distinguished. Rayleigh scattering is the scattering of light on particles smaller than the wavelength, e.g. air molecules and small aerosols. Mie scattering is the process of scattering on particles larger than the respective wavelength, e.g. aerosols and cloud droplets. Rayleigh scattering is approximately proportional to λ^{-4}, while Mie scattering is proportional to $\lambda^{-1...3}$, with a typical value of $\lambda^{-1.3}$ (Platt and Stutz, 2008). Although these are not absorption processes, the light scattered out of the probing light beam will usually not reach the detector and for the context of measurements can be treated in a similar way to absorption processes. Including these aspects, the Lambert-Beer law can be expanded to the following equation:

$$I(\lambda) = I_0(\lambda) \cdot exp\left[-L \cdot \left(\sum(\sigma_j(\lambda) \cdot c_j) + \varepsilon_R(\lambda) + \varepsilon_M(\lambda)\right)\right] \tag{4.2}$$

where $\varepsilon_R(\lambda)$ is the Rayleigh scattering coefficient, $\varepsilon_M(\lambda)$ is the Mie scattering coefficient and $\sigma_j(\lambda)$ is the absorption cross section of absorber j. Determination of the abundance of a particular absorber would need knowledge about all other factors influencing the measured light intensity, which is impossible for the atmosphere (Platt and Stutz, 2008). Scattering processes usually show broadband behaviour, meaning a slow variation with wavelength, while absorption processes vary rapidly with wavelength, typically with absorption features with widths narrower than 10 nm (Platt and Stutz, 2008). Figure 4.1 shows some example cross sections for different species.
The separation of broad- and narrowband structures forms the foundation of Differential Optical Absorption Spectroscopy (DOAS):

$$\sigma_j(\lambda) = \sigma_{j0}(\lambda) + \sigma'_j(\lambda) \tag{4.3}$$

$\sigma_{j0}(\lambda)$ denotes the absorption and scattering structures that vary slowly with wavelength, while $\sigma'_j(\lambda)$ shows the rapid variations with wavelength. $\sigma'_j(\lambda)$ is also called differential cross section.
Inserting 4.3 into 4.2 yields:

$$\begin{aligned} I(\lambda) = I_0(\lambda) \cdot exp\left[-L \cdot \left(\sum_j (\sigma'_j(\lambda) \cdot c_j)\right)\right] \\ \cdot exp\left[-L \cdot \left(\sum_j (\sigma_{j0}(\lambda) \cdot c_j) + \varepsilon_R(\lambda) + \varepsilon_M(\lambda)\right)\right] \end{aligned} \tag{4.4}$$

where now the first exponential describes the narrow structured absorption features and the second exponential describes the slowly varying absorption and scattering processes. Additionally to scattering and broad band absorption instrumental effects can also show a broad-band variation with wavelength. In DOAS, all broad-band spectral features are described by a polynomial and only narrow-band absorption features are used to determine the number density of the absorbers along the light path.

$$I(\lambda) = I_0(\lambda) \cdot exp\left[-L \cdot \left(\sum_j (\sigma'_j(\lambda) \cdot c_j)\right)\right] \cdot exp\left[-\sum_p a_p \lambda^p\right] \tag{4.5}$$

Taking the logarithm and rearranging to the optical density $\tau(\lambda) = ln(I_0(\lambda)/I(\lambda))$ yields the so-called DOAS equation:

$$\tau(\lambda) = ln\left(\frac{I_0(\lambda)}{I(\lambda)}\right) = L \cdot \left(\sum_j (\sigma'_j(\lambda) \cdot c_j)\right) + \sum_p a_p \lambda^p \tag{4.6}$$

Separation of broad band and narrow band spectral structures and the separation of various absorbers require the measurement of the intensity at multiple wavelengths, at

least as many as the combined number of absorber and polynomial coefficients. In most cases, the number of wavelengths is much larger.
The use of an extended wavelength range has advantages. The transmission of optical instruments typically shows broad spectral features, but as these terms show up in $I_0(\lambda)$ and $I(\lambda)$ these cancel out in the DOAS equation and no calibration of these properties is needed. Additionally, using a larger number of wavelengths allows the unique identification of traces gases, even for extremely weak absorptions (Platt and Stutz, 2008).
To obtain the number density of each absorbing species along the light path ($c_j \cdot L$), a least squares fit is performed on the measured optical density, for each wavelength step λ_k:

$$\sum_k r_k^2 \rightarrow min \quad with\ r_k = (\tau_{meas}(\lambda_k) - \tau_{fit}(\lambda_k)) \tag{4.7}$$

The differences r_k for all λ_k form a residual spectrum and contain all spectral structures which have not been accounted for in the DOAS fit and in best case only compromise of the measurement noise. To quantify the quality of the fit the root mean square of the residual spectrum,

$$RMS = \sqrt{\frac{1}{N}\sum_k^N r_k^2} \tag{4.8}$$

or the χ^2,

$$\chi^2 = \sum_k r_k^2 \tag{4.9}$$

can be used. In real measurements χ^2 can never become zero, even if all significant absorbers are accounted for, as the detector and photon noise of the measurement system will remain.
DOAS devices can be separated into active and passive systems. Passive DOAS systems use reflected sunlight, while in active DOAS systems an artificial light source is used. For passive DOAS systems the light path is not exactly known by the experimental set up, because the light is scattered somewhere in the atmosphere, while for active DOAS systems, the light path is known by the experiment set up. With active DOAS systems, the mean concentration of each absorbing species c_j can be calculated because L is known, while for passive DOAS instruments L needs to be estimated by other methods.

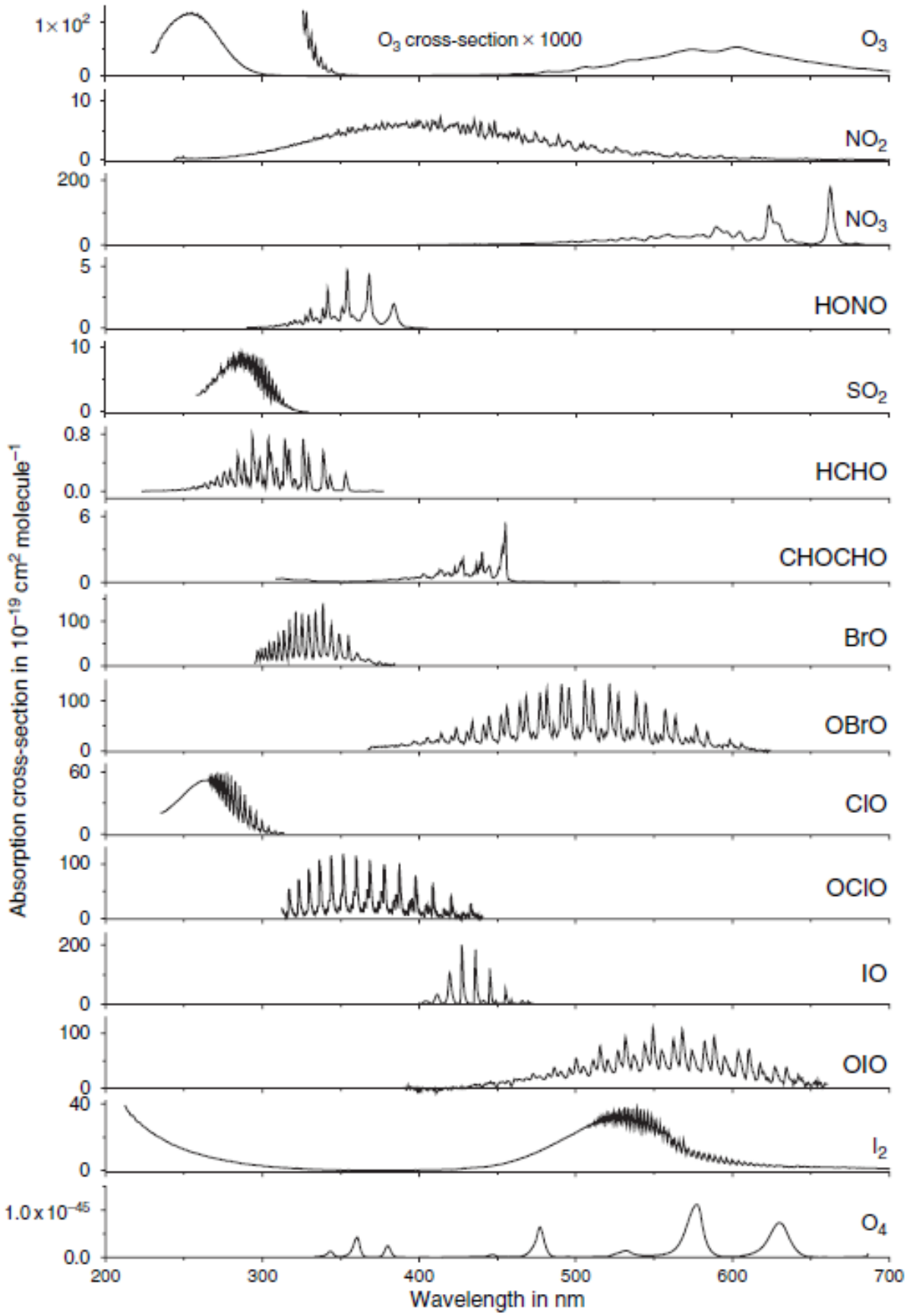

Figure 4.1: Examples of some absorption cross sections for different species as a function of wavelength in nm. Taken from Platt and Stutz (2008).

5 Measurements of shipping emissions at the Elbe in Wedel

[1] In this chapter, a newly developed LP-DOAS system of the company Airyx GmbH is evaluated and compared to a scientific grade LP-DOAS instrument of the university of Heidelberg. The comparison was made to evaluate, if a more simplified, more convenient to control and smaller instrument can reach the same quality level as the scientific instrument, and whether the new instrument is suitable to monitor ship emissions. In this comparison, the similarities and differences between both systems are highlighted, and the data measured by both systems is compared and validated. Subsequent to the comparison, a method to derive SO_2, NO_2 and NO_x emission rates of individual ship passages from LP-DOAS data is presented. The method has been applied to the data of one of the instruments and the derived emission rates were analysed in the context of ship type (inland or seagoing) and ship speed over ground. In total 233 days of measurements and about 7400 ship passages have been successfully evaluated.

5.1 Measurement site

Measurements made in this study were carried out in Wedel, a small town close to Hamburg, which is located on the river banks of the river Elbe. The river serves as the entrance route to the port of Hamburg and is well frequented by different types of ships going from or to Hamburg through the North Sea or the Kiel Canal. Most ships are container vessels, tankers, bulk carriers or reefer vessels. The measurement site is located on the northern banks of the river Elbe on the premises of the Waterways and Shipping Office (WSA) (53.570° N, 9.69° E) and is operated by the Federal Maritime and Hydrographic Agency (BSH) to monitor shipping emissions compliance according to MARPOL Annex VI. The standard instrumentation consists of in situ instruments to measure concentrations of SO_2, CO_2, NO_x and O_3. Those measurements are supplemented by an AIS (automatic identification system) receiver to obtain information about the passing ships, as well as meteorological measurements. All instruments are located close to the main shipping lane with a line of sight distance to the ships steaming from or to the port of Hamburg of 300 to 500 m. The port of Hamburg is located 10 km upriver from the measurement site and

[1] Parts of this chapter are based on Krause et al. (2021).

the ships still or already use their main engine. The prevailing wind directions in the area, which are from the south, are such that the emissions from shipping are often blown towards the measurement site. The southern river bank is rural and sparsely populated without large sources of air pollution. A detailed description of the in situ instruments used on site can be found in Kattner et al. (2015) who used these data to derive fuel sulphur content for passing ships.

5.2 DOAS Instruments

To monitor shipping emissions by optical remote sensing, two LP-DOAS instruments were set up on the northern river bank. The first one is a scientific LP-DOAS instrument built by the IUP Heidelberg and was set up in April 2018, the second one is a newly designed instrument, specifically developed to measure trace gases emitted by ships, especially NO_2, SO_2 and O_3. The new system was developed by the Airyx Gmbh and was set up in October 2018. Both systems comprise a telescope unit which is connected to a spectrometer and an artificial light source via optical fibres, and an array of retro reflectors. A schematic representation of the setup is shown in Figure 5.3. The technical details of both systems are shown in Table 5.1. In direct comparison the newer Airyx instrument is much smaller than the Heidelberg instrument. Additionally, the Airyx instrument, once set up and started, can be controlled completely via software, while the Heidelberg instrument uses mixed hardware and software controls.

Both instruments use an commercially available Laser Drive Light Source (Energetiq EQ99), which supplies energy to a xenon plasma with an infra-red laser. These light sources have a high brightness across the whole emitted spectrum (280 - 500 nm).

The Airyx system uses a fully enclosed telescope box, which is fixed in position. The telescope itself consists of a spherical mirror with a diameter of 20 cm and a focal length of 80 cm. Close to the focal point there is a front post with a small angled mirror, which reflects the light coming from the light source onto the main mirror. The position of the small mirror can be adjusted, so that the light beam can be aimed directly at the retro reflectors, while the telescope itself does not move. Inside the telescope there is a small heater and drying agent to prevent condensation of water vapour. Light is only able to enter or leave the telescope through a fused silica window. Also the instrument is equipped with a video camera, which allows to survey the light path during measurement. The whole telescope unit is weatherproof and does not need additional housing. Light source, spectrometer and control hardware are also placed inside weatherproof boxes. Only the laptop which is used to control the device and to save the measured data is not weatherproof and needs to be placed inside.

In contrast, the instrument of the IUP Heidelberg is larger and has a telescope with a diameter of 30 cm and 150 cm focal length. This telescope is not fully closed and light

Figure 5.1: Telescope unit of the Airyx LP-DOAS instrument.

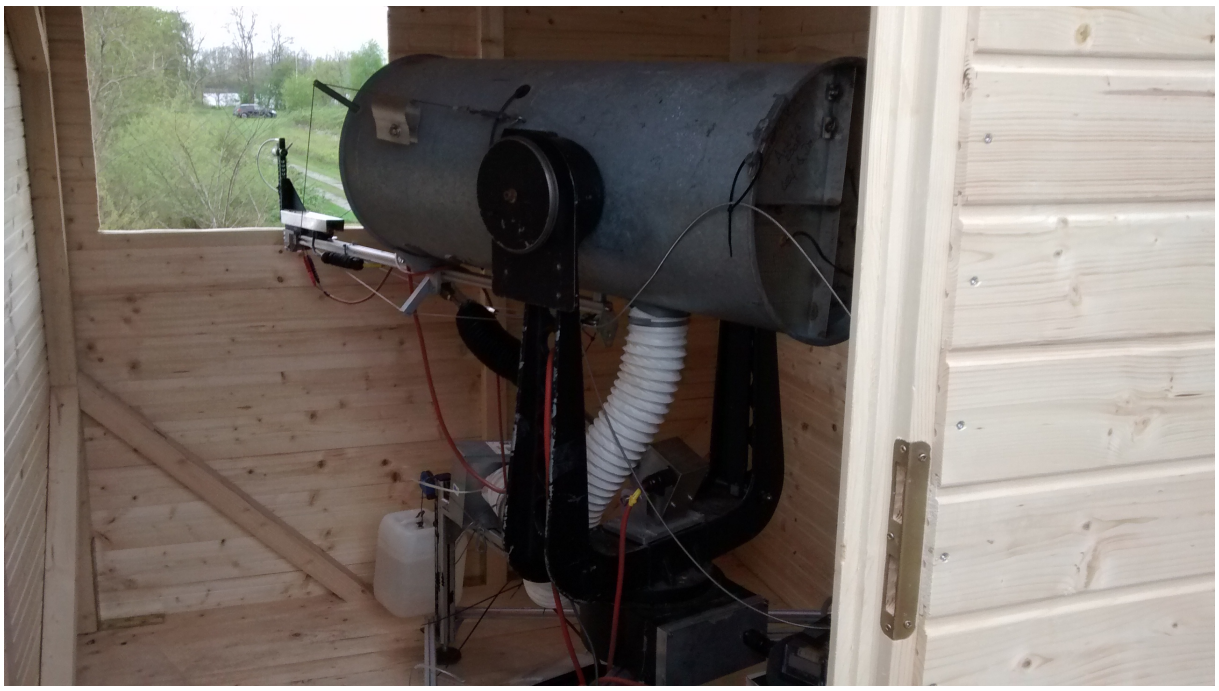

Figure 5.2: Telescope unit of the IUP Heidelberg LP-DOAS instrument.

Table 5.1: Characteristics of the LP-DOAS system.

Component	IUP Heidelberg	Airyx
Light source	Laser-Driven light source Energetiq EQ99	Laser-Driven light source Energetiq EQ99
Optical fibres	200 μm, 800 μm	200 μm, 800 μm
Telescope mirror	Diameter 0.3 m, focal length 1.5 m	Diameter 0.2 m, focal length 0.8 m
Spectrometer	Acton Spectra Pro 300i	Avantes UV-VIS
CCD	2048×512 pixel Roper scientific back-illum.	2048×64 pixel Hamamatsu back thinned
Measured wavelengths	280 – 362 nm, 0.53 nm resolution	280 - 445 nm, 0.76 nm resolution

enters through a hole in the front of the telescope. To aim at the retro reflectors, the whole telescope unit is moved. Also here a video camera is installed to help operating the system. All components need to be placed inside a weatherproof location.

For both instruments, the light which enters the telescope is transmitted to the spectrometer by six 200 μm optical fibres, which are coupled to the telescope in such a way, that they surround the emitting fibre in a circular manner (see Figure 5.3). These six fibres are then coupled to a single 800 μm fibre, which is used for mode mixing and increases the quality of the derived spectra. For both instruments, the temperature of the spectrometers can be regulated to a certain degree, which decouples them from the ambient temperature and increases the quality of the measured spectra.

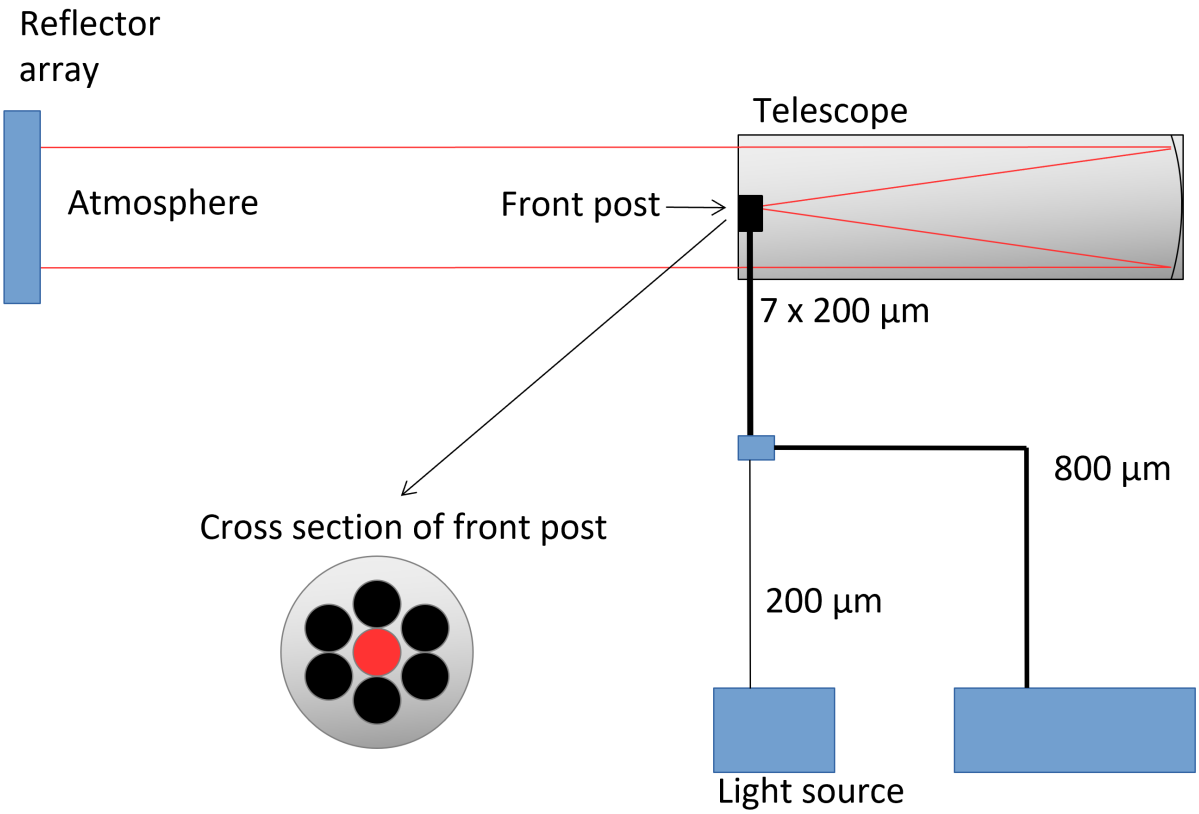

Figure 5.3: Schematic representation of the Long Path DOAS systems. The system itself consists of a telescope, a y-shaped fibre bundle, a light source, a spectrometer and a reflector array. The emitting fibre is shown in red, while the receiving fibres are shown in black.

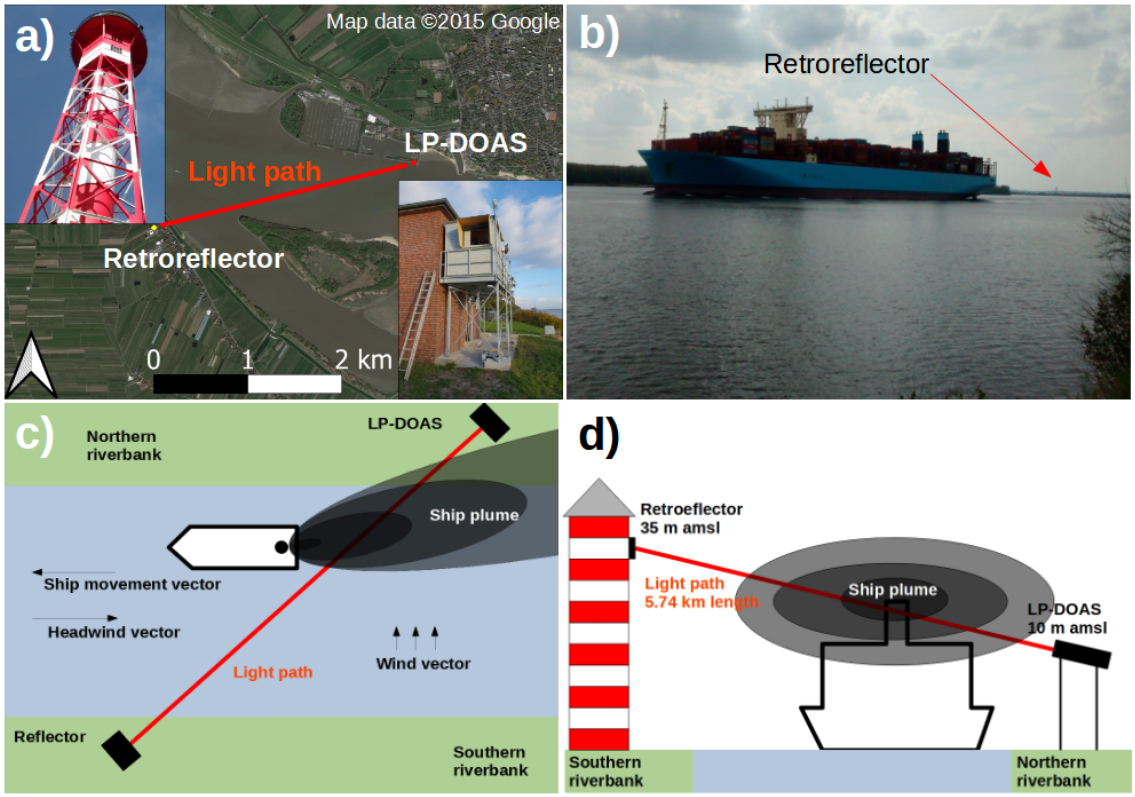

Figure 5.4: a) Satellite image of instrument location, with LP-DOAS marked as a red dot on the northern river bank and retro reflector position marked as yellow dot on the southern river bank. b) Image of a passing container ship next to the measurement site. c) Schematic overview of the measurement geometry of the LP-DOAS for a passing ship leaving Hamburg towards the North Sea, seen from above. d) same as c) but seen from the port of Hamburg. Note that c) and d) are not to scale.

5.3 Comparison between the two DOAS-Systems

The scientific system of the IUP Heidelberg has been used as a reference system to evaluate the performance of the Airyx system. Both measured simultaneously and use the same measurement principle, but there are differences in the hardware. The Airyx system uses a smaller telescope with a smaller mirror and consequently receives less light than the IUP Heidelberg system. Also the Airyx system uses a smaller spectrometer and CCD, which at the same time cover a larger wavelength region. The fitting windows for both systems are slightly different for each trace gas and are shown in Table 5.2.

Figure 5.5 shows a first comparison of both systems, for each system a NO_2 and a SO_2 fit was performed in their respective fitting window. The general shape and the finer peak structures are similar for both systems. The negative values of NO_2 time series of the Airyx system are caused by low light intensity (e.g. cases where a ship blocked the

Table 5.2: DOAS fit settings for the retrieval of SO_2, NO_2 and O_3.

Trace gas	SO_2	NO_2	O_3
Fit window IUP Heidelberg	297.0 - 309.0 nm	334.5 - 356.5 nm	282.0 - 314.5 nm
Fit window Airyx	296.4 - 319.5 nm	395.4 - 444.7 nm	282.5 - 322.5 nm
Polynomial degree	3	3	3
Cross sections	NO_2 298 K (Vandaele et al., 1996) O_3 293 K (Serdyuchenko et al., 2014) SO_2 294 K (Vandaele et al., 1996) HCHO 297 K (Meller and Moortgat, 2000)	NO_2 298 K (Vandaele et al., 1996) O_3 293 K (Serdyuchenko et al., 2014) O_4 293 K (Thalman and Volkamer, 2013) HCHO 297 K (Meller and Moortgat, 2000) HONO 296 K (Stutz et al., 2000)	NO_2 298 K (Vandaele et al., 1996) O_3 293 K (Serdyuchenko et al., 2014) SO_2 294 K (Vandaele et al., 1996) HCHO 297 K (Meller and Moortgat, 2000)

light path), which were not automatically filtered out before the DOAS fit was performed. Both systems generally show a similar time series of NO_2 and SO_2, but there are some differences.

The smaller telescope of the Airyx instrument ultimately results in a lower amount of received light, which leads to a smaller signal to noise ratio, especially for the UV wavelengths used in the SO_2 fit. Also the fused silica window of the Airyx system reduces the amount of incoming light that reaches the spectrometer. Another influence was the way the telescope was mounted, which lead to stray light reflected from lamp which could reach up to 12 % of the received intensity in the UV wavelengths, depending on the exact conditions. The uncertainty of the derived SO_2 time series of the Airyx instrument was up to 40 % larger due the factors mentioned.

Differences in NO_2 between both systems originate mainly from the different fitting windows. NO_2 has stronger absorption features in the visible wavelength region than in the UV region, consequently, the fit is performed in the visible wavelengths. Generally, in the visible wavelengths more light is available, which reduces the relative contribution of stray light from the telescope unit to the total signal measured by the CCD.

For both instruments and all fitted trace gases, the quality of the fits can be improved by temporal averaging of the individual spectra before the DOAS fit is applied. This increase in the quality of the fits comes at the cost of temporal resolution.

A regression analysis for data measured by both systems, between 16th November 2018 and 4th March 2019 showed a good agreement between them, with R^2 of 0.97 for SO_2 and 0.96 for NO_2, respectively (Figure 5.6). The slope of the linear regression is not one but slightly below it with values of 0.86 for SO_2 and 0.89 for NO_2. The standard error of the slope is several magnitudes smaller than the slope itself and are therefore not shown. Additionally in Figure 5.6, histograms of the ratio (Airyx/Heidelberg) of the derived trace gas slant columns are shown, for NO_2 there is a well defined peak, with a median ratio of 0.97. For SO_2 the distribution is broader, with a median ratio of 0.87.

Figure 5.7 shows the histograms of the derived NO_2 and SO_2 slant columns for both instruments. The SO_2 slant columns are low most of the time and only in a low percentage of time, there are higher values. For NO_2 the slant columns show a broader distribution with a wider spread from low to high values. The measured NO_2 signal stems from different sources, e.g. passing ships, old diluted ship plumes, the plume of a nearby power plant and the plume of the city of Hamburg, which depending on wind direction have varying contribution to the measured NO_2. For SO_2 the only significant source are the emissions of passing ships.

Generally, the new Airyx system is well suited to measure ship emissions and is comparable to the IUP Heidelberg LP-DOAS. After this initial comparison phase, the Airyx instrument was mounted in a new position, which fixed the stray light problem. The Airyx instrument is now routinely measuring while the Heidelberg instrument has been

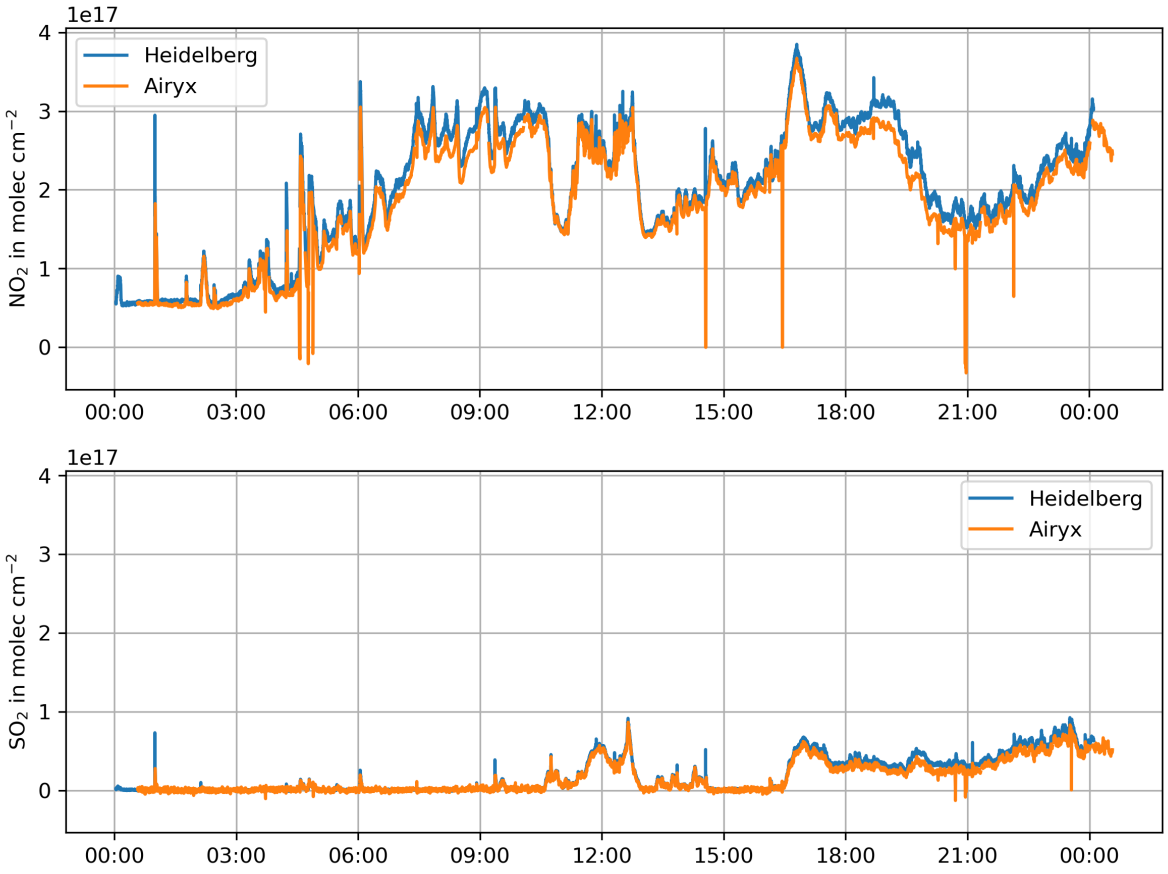

Figure 5.5: Comparison of derived SO_2 and NO_2 slant columns for both systems for a single day.

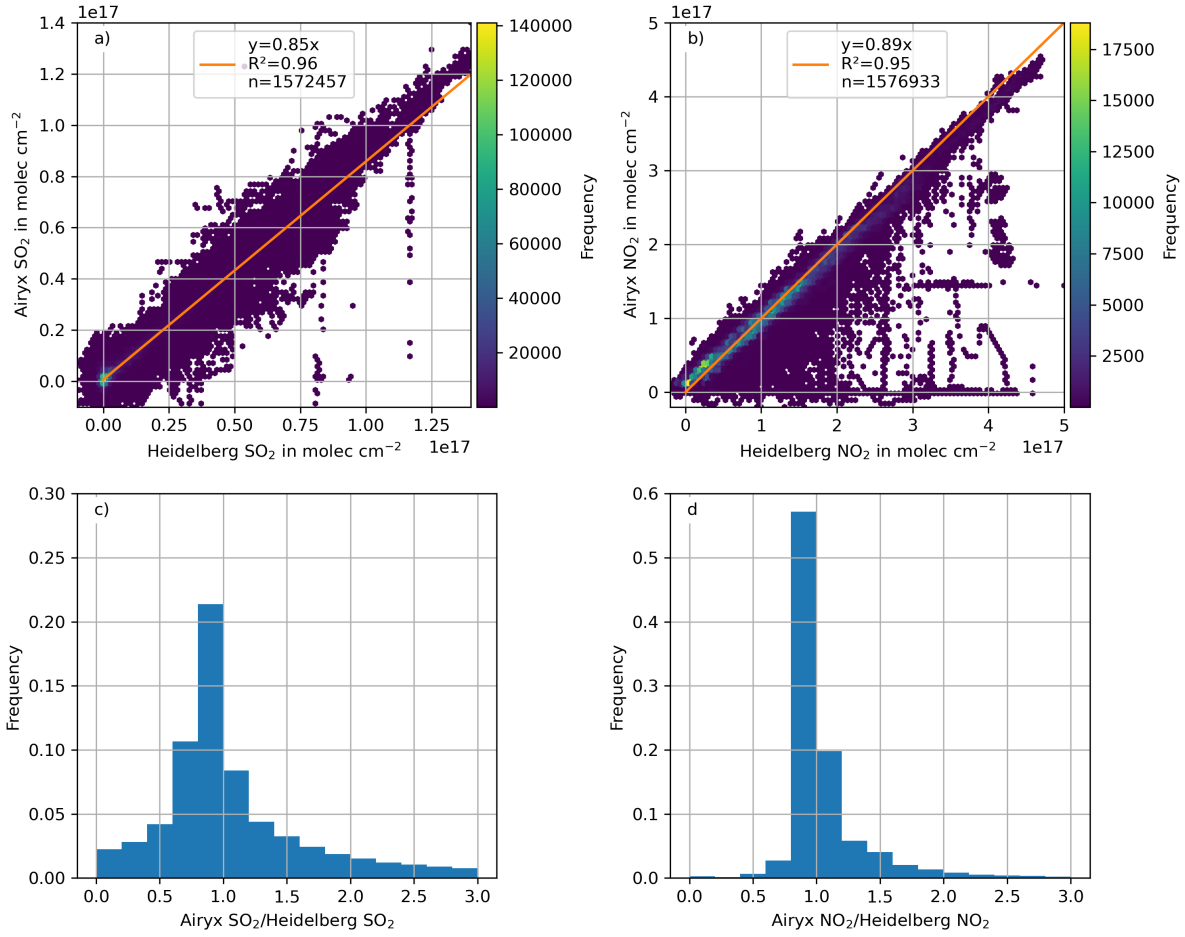

Figure 5.6: Scatter plots of derived SO_2 and NO_2 between both instruments. Orange line shows the result of the linear regression.

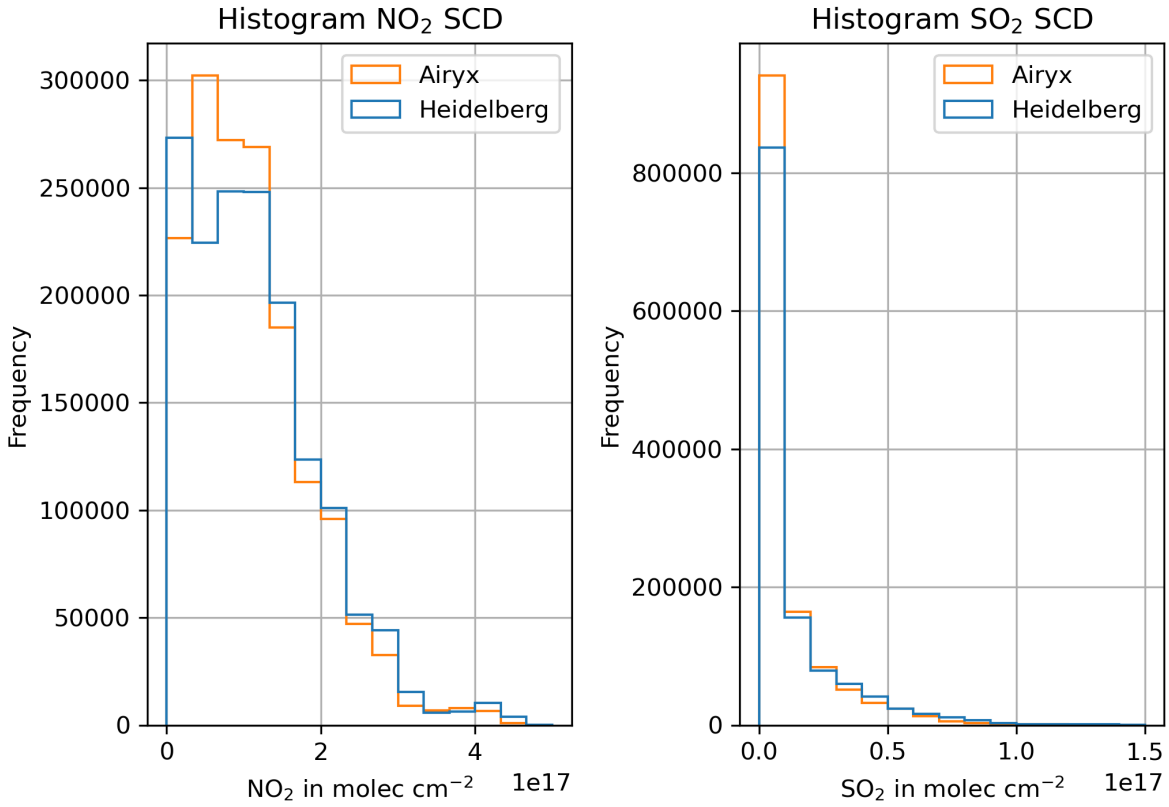

Figure 5.7: Histograms of derived SO_2 and NO_2 slant columns.

dismantled.

5.4 Analysis of ship plumes using LP-DOAS measurements

As an example for the application of LP-DOAS measurements in the context of ship emissions, the measurements made by the IUP Heidelberg instrument will be presented and evaluated in the following sections.

To analyse the measured NO_2, SO_2 and O_3 time series with regard to ship emissions and their influence on these specific trace gases, individual ship plumes have to be identified. For the analysis of the plumes caused by individual ship passages, several steps are needed. First of all the measured spectra are analysed using the DOAS technique to determine the concentration of the absorbing gas along the light path. Secondly, the individual contribution of a ship plume to the total measured integrated concentration of a pollutant along the light path is determined and assigned to the respective source ship.

Each emission plume can be identified by enhancements (peaks) found in the NO_2 and possibly SO_2 time series, additionally the O_3 time series shows a minimum (dip), when a ship plume passes through the light path. The peaks and dips are identified using a low

pass filtered time series. The low pass filtered time series is calculated using a running median with a window size of five minutes. The low pass filtered time series represents the background concentration including influences by meteorological factors, but excludes the short term variations caused by plumes of passing ships. In order to identify the peaks and dips, the low pass filtered time series is subtracted from the original time series. The result is a time series which is close to zero on average, but still contains several peaks, which occur on small time scales. To differentiate a peak caused by some sort of emission from noise in the measurements, it is checked whether the peaks exceed a predefined threshold. Every peak that exceeds this threshold is marked as a valid increase in the trace gas concentration by an emission source, e.g. a passing ship. In this study the threshold was set to four times the DOAS fit error of the respective trace gas measurement. The analysis was carried out separately for each trace gas of interest (NO_2, SO_2 and O_3).

An example of a fitted trace gas time series is shown in Figure 5.8. Blue lines show the fitted trace gas time series and the orange lines show the mean detection limit for the respective trace gas. The gray dashed lines mark passing ships that have been assigned to a peak or dip. The green lines, often overlaying the blue lines, show the estimated background concentration, i.e. the concentration not caused by recent emission of a passing ship. Following Stutz and Platt (1996), the DOAS measurement error was defined as two times the DOAS fit error and the detection limit for each trace gas was defined as two times the measurement error (four times the DOAS fit error). The median detection limits are 190 pptv for NO_2, 59 pptv for SO_2 and 253 pptv for O_3, respectively. Before further analysis individual DOAS fits with a RMS higher than 0.01 are removed from the dataset, as these usually indicate a ship blocking the light path partly.

The time series for the different trace gases do not show the same behaviour, even though they are measured by the same instrument at the same time. All passing ships cause a peak in NO_2, but the increase in SO_2 might be too low to cause a peak that can be identified. Additionally, the peaks of NO_2 and SO_2 might not occur at the same time, as ships mostly emit NO which reacts with O_3 in the ambient air and gets converted to NO_2. Even thought this is a fast reaction, the NO_2 peak can occur after the respective SO_2 peak.

In order to cause a peak in the measured time series, the plumes have to cross the light path. For small ships this means, the plume needs to rise from water surface upwards through the light path. For large ships, the emission can take place above the light path and downward mixing is required, e.g. caused by the turbulence generated by the movement of the ship.

The height and form of the measured peak depend on several factors. Most importantly is the viewing geometry. Largest peaks are found when the plume is parallel to the light path, while the smallest peaks are found when the plume is orthogonal to the light path. Also the light path of the DOAS instrument covers large volumes of clean air, which

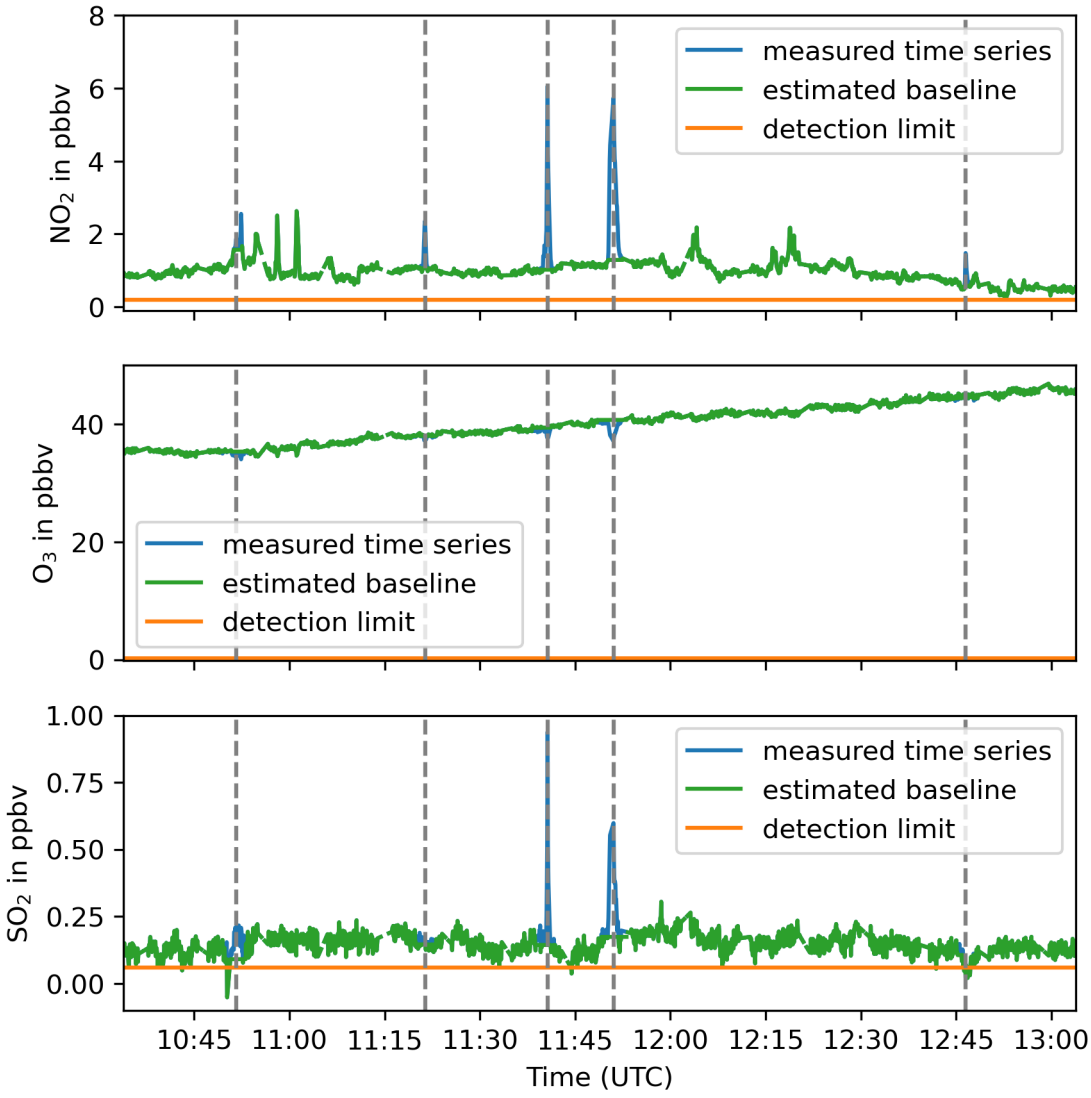

Figure 5.8: Example time series of the fitted trace gases from 19th August 2018 between 10:30 and 13:00 UTC. In each plot the blue line shows the fitted time series of the respective trace gas and the orange line shows the respective median detection limit. The grey dashed lines mark passing ships, that have been assigned to a peak in the time series. The green line shows the calculated background.

are not part of the plume itself. The DOAS instruments derive the mean concentration along the light path and usually only a small part of the light path is affected by a plume, while unpolluted air has a much larger contribution to the measured mean. Consequently, sometimes the increase in a trace gas slant column might be hard to notice.

In the next step, the identified peaks are assigned to their respective source ship. The assignment uses AIS data of passing ships. The AIS data contains the current position, speed and heading of the ship. Additionally, more general information about the ship is also transmitted (length, width, type, destination, ...). The AIS data is transmitted in regular intervals, usually between two to thirty seconds. For this analysis the AIS signals were interpolated to a one second time resolution, using linear interpolation between two received AIS signals, to better track the position of the ship while being close to the instrument light path. For each detected peak (or dip) in the trace gas time series it is then checked, if there was a ship in a position close to the light path, which may have caused the increase in the trace gas concentration causing the peak. If there is an individual ship in a position that could be the source of the enhancement of the trace gas, this ship is assigned to the respective peak. The assignment is based on position and time. Each peak or dip occurs at a time t_{peak}. For each peak occurrence, a time window of $(t_{peak} - \Delta t_{before}) < (t_{peak} + \Delta t_{after} + \Delta t_{dyn})$ is defined, where Δt_{before} is set to 30 and Δt_{after} is set to 120 seconds, and Δt_{dyn} is calculated as the length of the ship divided by the speed of the ship. The time window starts before the peak occurrence to accommodate for ship plumes that are transported by the wind through the light path before the ship itself passed through. The windows are extended dynamically by size and speed of the ship to consider that larger ships may need a longer time to pass through the light path. Due to the length of the defined time window, several positions of an individual ship may be a possible source position. The final assignment is based on the distance to the light path as well as course and length of the ship. The first position where the ship could have fully passed (with its full length) the light path is assigned as the respective source position responsible for the trace gas peak. The median time difference between measurement of the peak maximum and the assigned AIS position is 20 seconds. This approach fails if the traffic density is too high, making the unambiguous attribution of a plume to a particular ship impossible. Neglecting the additional criterion of a full pass and using stricter time windows around each peak, a higher number of peaks could be attributed to ships, but this also increases the chance of mismatches and the assignment of mixed plumes of several ships to a single ship.

5.4.1 SO_2/NO_2 ratios of individual ship passages

To get a first impression about the emission behaviour of individual ships, SO_2/NO_2 ratios were calculated. Most of the emitted nitrogen oxides are thermal NO_x, therefore,

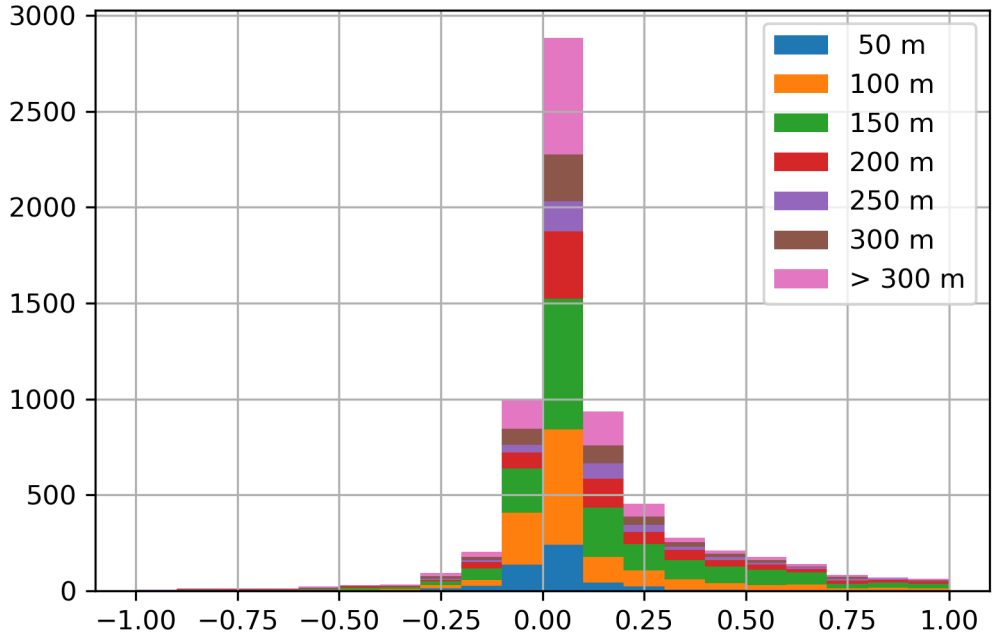

Figure 5.9: Histogram of SO_2/NO_2 ratios derived from the data measured by the IUP Heidelberg LP-DOAS instrument for data measured between May 2018 to April 2019. Ratios were classified by ship length.

the amount should be independent of the used fuel type. The amount of emitted SO_2 however depends on the fuel sulphur content. Ships using a sulphur rich fuel consequently should have a higher SO_2/NO_2 ratio than ships using less sulphur rich fuels. These ratios were calculated out of the integrated peak values for each SO_2 and NO_2 and are shown in Figure 5.9. The histogram shows a normal distribution of SO_2/NO_2 ratios with a median of about 0.06. Negative values are caused by low SO_2 peak values, which are close to the detection limit and the background correction can cause slightly negative values. Before the reduction of the fuel sulphur content in SECAs, ratios were considerably higher in the German Bight, with a mean of 0.30 and a median of 0.26, while after the reduction the median was found to be 0.013 (Seyler et al., 2017). The difference between both ratios can be explained by the chemical reactions taking place, that convert emitted NO to NO_2. In Wedel, fresh plumes are observed and the reaction from NO to NO_2 is still taking place, while Seyler et al. (2017) observed well mixed plumes at larger distances to the measurement site, where the conversion could have already taken place.

5.4.2 Estimation of emission rates SO_2, NO_2 and NO_x of individual ships

For a more detailed analysis of ship emissions, emission rates for individual ship passages have been derived from the LP-DOAS measurements and were analysed. These emission rates describe the emission behaviour of individual vessels and potentially could be used as input for additional studies, e.g. model studies investigating the influence of ship emissions on air quality or for emission inventories. Usually this information comes from in situ measurements, either on-board the ship or onshore. In both cases the statistics are limited, on-board measurements being restricted to a small number of ships, and onshore measurements depending on favourable wind conditions, to transport the emitted substances to the measurement site. Remote sensing techniques such as LP-DOAS can help to supplement in situ measurements, as the technique enables ship plumes, containing pollutants to be measured independent of meteorological conditions. To calculate the emission rates, several steps are needed. In the first step, enhancements of NO_2 and SO_2 were assigned to the respective source ship, which has already been described in the previous section.

As the LP-DOAS instrument does not measure the concentration of the trace gases at the stack, a model has to be applied to estimate the emission from the concentration enhancement found for a given light path. This conversion is based on the assumption that the plume of a single ship can be described by a simple Gaussian plume model (Pasquill, 1968) and can be expressed mathematically by Equation 2.5. Using this equation, a three dimensional field of concentrations is calculated. The dispersion parameters depend on x, the atmospheric stability and the surrounding environment, which differs for open country and urban conditions. A simple classification scheme for the stability classes is shown in Table 2.2, while the corresponding dispersion parameters are listed in Table 2.3. To determine atmospheric stability at the measurement site, the wind speed measurements of the in situ instruments are used, while incoming global radiation and cloud coverage are taken from a nearby measurement station of the German Weather Service located at the Hamburg-Airport (DWD Climate Data Center, 2022a,b).

To calculate the emission rate of a ship during its passage, the model is evaluated once using an arbitrary but constant emission rate (Q_{model}), using the ship's position as the starting point of the plume. The effective height of the plume is set to the height of the funnel above the mean water level, assuming the plume quickly bends down due to the wind and the movement of the ship. The height of the stack above water level is unfortunately not transmitted in the AIS signals, instead, the height of the stack is estimated from pictures of the respective ship, preferably taken by the camera of one of the instruments, or otherwise by pictures uploaded to marinetraffic.com (MarineTraffic, 2021). The dispersion parameters σ_y, σ_z are chosen according to atmospheric stability

and for open country site. To account for the movement of the ship, the wind direction and wind speed have been combined with the movement of the ship to an apparent wind speed and apparent wind direction (Berg et al., 2012):

$$U_{aw} = \sqrt{(v_{wind\,N} + v_{ship\,N})^2 + (v_{wind\,E} + v_{ship\,E})^2} \tag{5.1}$$

$$\theta_{aw} = -\text{atan2}[(v_{wind\,E} + v_{ship\,E}),\ (v_{wind\,N} + v_{ship\,N})] \tag{5.2}$$

where $v_{wind\,E}$, $v_{ship\,E}$ and $v_{wind\,N}$, $v_{ship\,N}$ are the eastern and northern velocity components of the wind vector and ship movement vector, respectively. Equation 5.2 uses the commonly available atan2 variation of the arctangent function which returns the inverse tangent of the first and second argument to the function (Berg et al., 2012).

As the real emission rate at the ships chimney (Q_{meas}) is unknown, this model run only gives insight into the dispersion of the emitted species. To retrieve the desired emission rate for a certain species emitted by the ship, the measured concentration (C_{meas}) is compared to the modelled concentration (C_{model}) along the light path. C_{meas} represents only the enhancement (the peak) of the measured trace gas concentration above the respective background. In order to remove the background from the measured peaks, the mean concentration 30 seconds before and after the peak was calculated and subtracted from the peak itself. The low-pass filtered time series used to identify the peaks was not used as a background, because it can overestimate the background concentration in cases of high traffic density. C_{model} is obtained by averaging all model grid cells along a path through the model grid, which corresponds to the light path during the measurement.

The LP-DOAS instrument measures not only the pure emission of the start point, but also older parts of the plume at the same time. The modelled region covers an area of approximately 2800 m x 700 m and the assigned ship position is always very close to the light path. Therefore the slightly different time of emission is neglected for simplicity and it is assumed that the measured plume is the result of the pure emission at the start point. As the time between emission and measurement by the LP-DOAS is on the order of seconds, possible effects of NO_2 photolysis are small and are neglected. Assuming all parameters are estimated correctly, the only difference between modelled concentration and measured concentration is caused by a different emission rate. Therefore Q_{meas} can be estimated by the following equation:

$$Q_{meas} = \frac{C_{meas}}{C_{model}} \cdot Q_{model} \tag{5.3}$$

This approach assumes that the motion vector of the ship and the emission rate is constant for the time between emission and measurement of the enhanced concentration.

Estimation of NO_x from measured NO_2

Ships emit NO_x, but the Heidelberg LP-DOAS, being restricted to the wavelength range between 280 and 360 nm is only able to measure NO_2. Part of the NO_2 is directly emitted while other parts are the result of the reaction of emitted NO with atmospheric ozone:

$$NO + O_3 \longrightarrow NO_2 + O_2 \tag{R 5.1}$$

To estimate the total NO_x emission, a simple approach is used to convert the measured NO_2 concentrations to NO_x concentrations using the NO_2/NO_x ratio. The correct NO_2/NO_x ratio can be obtained by summing the NO_2 and O_3 signals and plotting this sum against the measured NO_x concentration (Clapp, 2001; Kurtenbach et al., 2016). This kind of analysis has been carried out using data from the in situ measurements which provide NO_x, NO_2 and O_3 observations and results in a mean NO_2/NO_x ratio of 0.138 (see Figure 5.10) which agrees with previous studies Cooper (2001). This means most of the emitted NO_x is emitted as NO and only a smaller fraction is directly emitted as NO_2. The NO_2 peak observed by LP-DOAS can then be converted to NO_x using the following formula:

$$NO_x = \frac{(\Delta NO_2 + \Delta O_3)}{NO_2/NO_x ratio} \tag{5.4}$$

where ΔNO_2 is the increase in NO_2 caused by the ship and ΔO_3 is the decrease in O_3 caused by the reaction of emitted NO with atmospheric O_3 and is also measured by the LP-DOAS. ΔO_3 is negative, as O_3 is consumed in the reaction with NO to form NO_2. Using this approach, the total amount of measured NO_2 is corrected for the NO_2 that formed during transport in the atmosphere, and the remaining NO_2 is the amount primarily emitted by the ship. The primarily emitted NO_2 is then used to estimate the amount of emitted NO_x using the NO_2/NO_x ratio. It is assumed that the NO_2/NO_x ratio is the same for all ships and that no other species are emitted which could impact on the NO_2 production or O_3 removal. Based on the compact correlation found (shown in Figure 5.10), these assumptions appear to be justified. Also, there is no indication for further dependencies of the NO_2/NO_x ratio on the position of the source ship, the wind direction or age of the measured plume.

The NO_2/NO_x ratio has been derived from in situ measurements and is assumed to be the same for the LP-DOAS measurements. Comparison of the in situ measurements and the DOAS measurements is not straight forward, because both systems measure different air masses. The in situ measurements only rely on the transport of air masses to the measurement site, whereas the LP-DOAS measures the integrated number density of the respective trace gas along the light path. Only a small portion of the light path is affected by a plume and most of the signal comes from relatively clean air masses. Consequently,

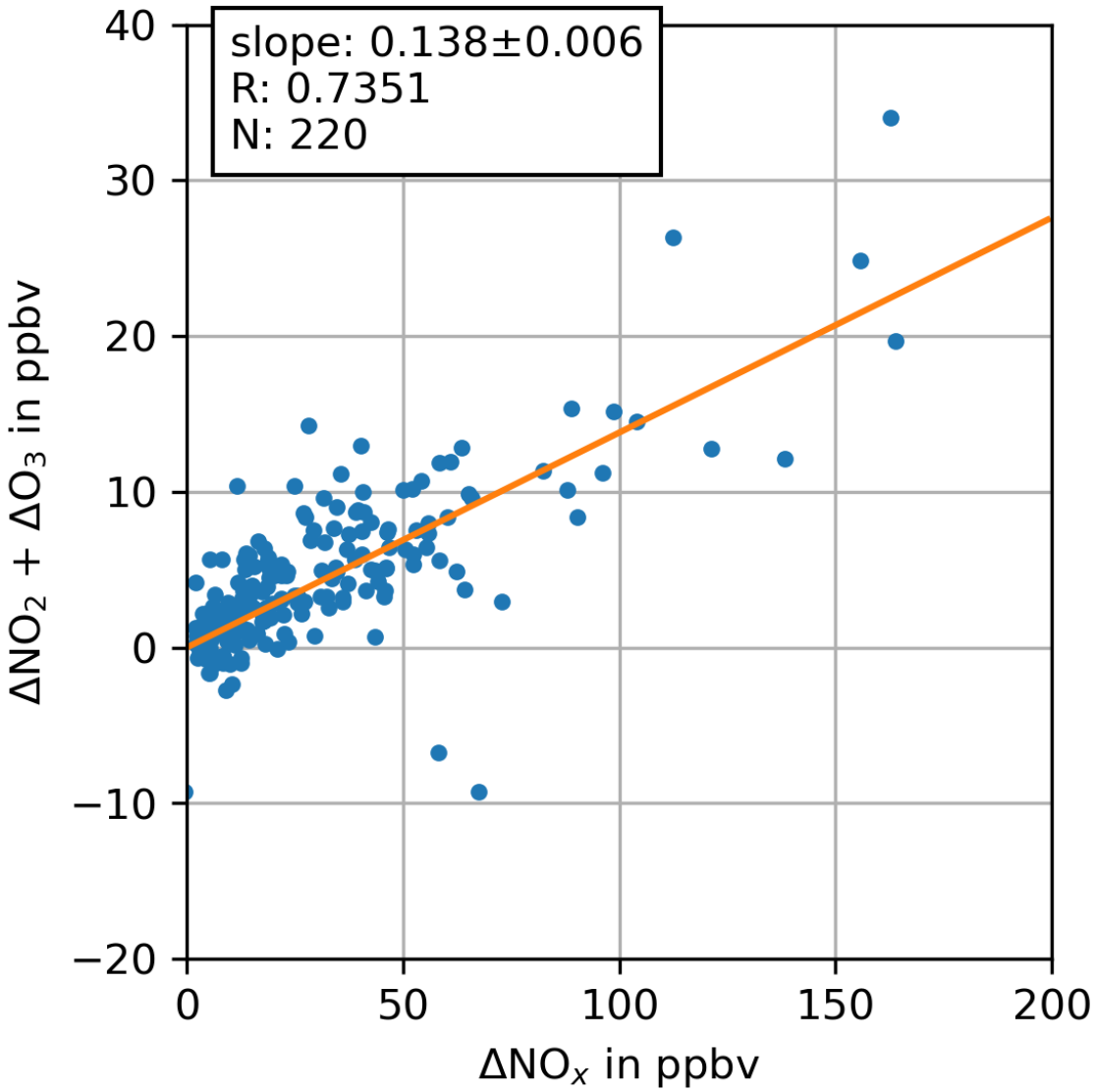

Figure 5.10: Plot of $\Delta NO_2 + \Delta O_3$ against ΔNO_x from peaks measured with the in situ instruments between April 2018 and May 2019. ΔO_3 is always smaller than zero, as it represents the O_3 that is consumed in the reaction with NO to form NO_2 (R 5.1). All concentrations have been corrected for background concentrations. For this analysis, 220 manually quality checked peaks were used. This results in a slope (a NO_2/NO_x ratio) of 0.138 with a respective standard error of 0.006.

the enhancements of NO_2 and SO_2 are lower in the time series measured by the DOAS instrument than in the in situ data. Nevertheless both measurements agree and show similar concentrations of NO_2 and SO_2(e.g. Figure 5.11).

Uncertainty of the derived emission rates

The uncertainty of the emission rate is given by:

$$\sigma_Q = \sqrt{\left(\frac{\partial Q_{meas}}{\partial C_{meas}} \cdot \sigma_{C\,meas}\right)^2 + \left(\frac{\partial Q_{meas}}{\partial C_{model}} \cdot \sigma_{C\,model}\right)^2} \tag{5.5}$$

where $\sigma_{C\,meas}$ is the uncertainty of the measured trace gas concentration and $\sigma_{C\,model}$ the uncertainty of the modelled trace gas concentration. In case of NO_x, $\sigma_{C\,meas}$ consists of the uncertainty of the NO_2 concentration, the uncertainty of O_3 and the uncertainty of the NO_2/NO_x ratio.

To calculate $\sigma_{C\,model}$, Monte-Carlo-Simulations are performed for each individual passing ship, where U_{aw}, θ_{aw}, atmospheric stability, latitudinal- and longitudinal position of the ship and the funnel height of the ship are varied within their respective uncertainty range. The assumed uncertainty for each parameter is shown in Table 5.3. This results in a set of simulations for every input parameter, and for each simulation in the respective set, the concentration along the artificial light path is determined. A set for a single input parameter (j) is then summarized as mean concentration ($mean_{C\,j}$), the respective standard deviation ($\sigma_{C\,j}$), minimum ($min_{C\,j}$) and maximum value ($max_{C\,j}$). The model uncertainty is then calculated as:

$$\sigma_{C\,model} = \sqrt{\sigma^2_{C\,U\,aw} + \sigma^2_{C\,\theta\,aw} + \sigma^2_{C\,stability} + \sigma^2_{C\,lon} + \sigma^2_{C\,lat} + \sigma^2_{C\,H}} \tag{5.6}$$

where each $\sigma_{C\,j}$ is the standard deviation of the modelled trace gas concentrations of the Monte-Carlo-Simulations with respect to changes of an individual parameter j. As the parameters are changed individually, possible interactions between changes of more than one parameter at a time are neglected.

The largest source of uncertainty is the uncertainty of the position of the emission source, as it has a large impact on which part of the plume is assumed to be measured, and consequently has a large impact on the derived C_{model}. The position is determined by the transmitted AIS signals, which have an average uncertainty of 10 m or less in longitudinal and latitudinal direction. However, the AIS signal only reports the position of the AIS transmitter and the location of the funnel in relation to the position of the transmitter is not known. Therefore, the positional uncertainty also depends on the dimension and orientation of the ship. Generally, it is assumed that the emission source is located at the position given by the AIS signal. The transmitter is assumed to be close to the bridge of the ship and that the funnel is also in close proximity. For smaller ships, e.g. inland

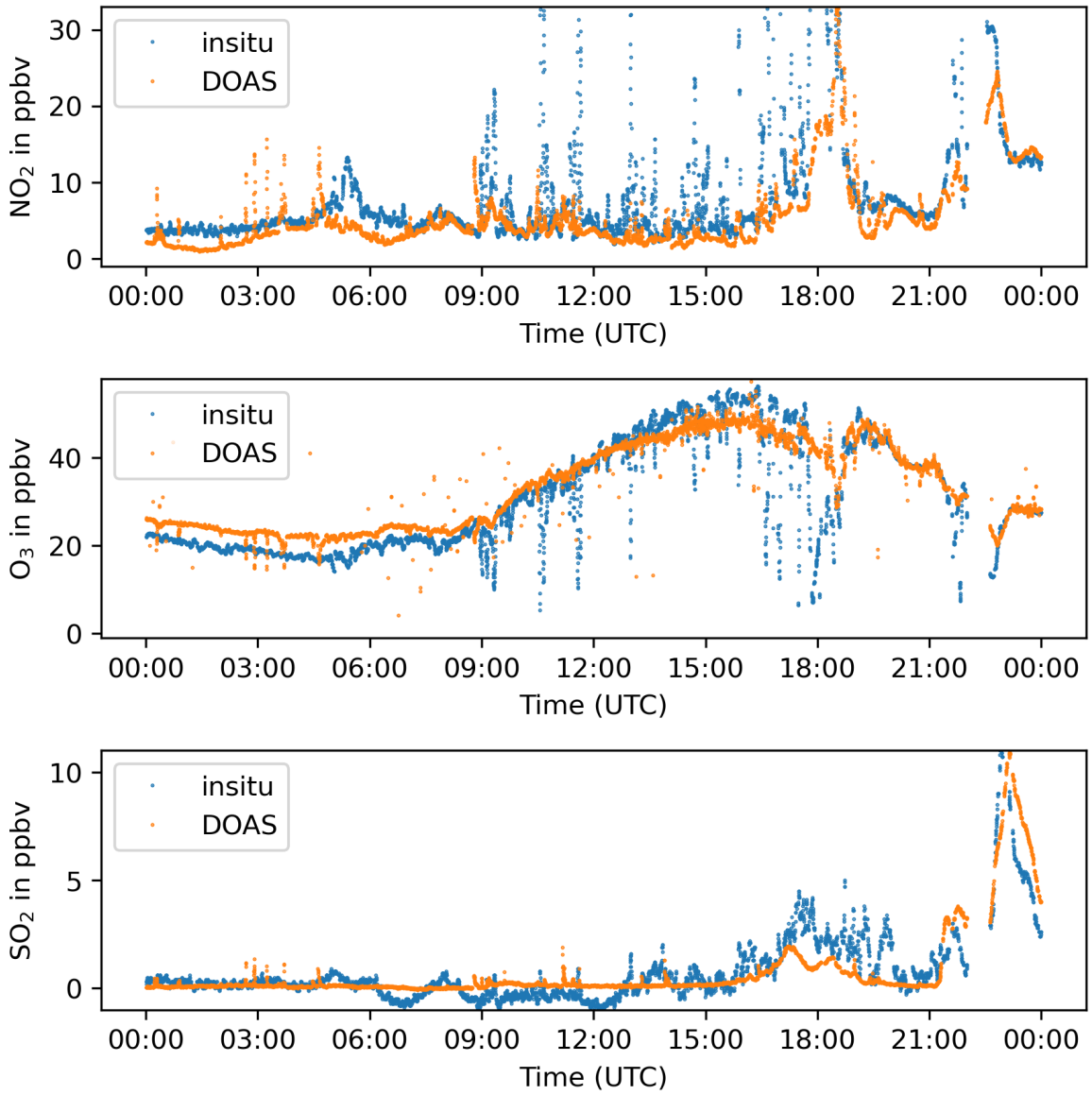

Figure 5.11: Time series of NO_2, O_3 and SO_2 measured by the in situ instruments (blue) and the IUP Heidelberg LP-DOAS (orange) on 20th July 2018.

ships, this is certainly true, due to the small dimensions of the ship. For larger (sea) ships such as tankers and container ships, different designs exist. Also here it is assumed that the transmitter is close to the bridge and that the main exhaust is not further away from the transmitter than half the ship width or length.The height of the emission source depends on the stack height above the water level and the water level itself. The stack height is estimated from pictures of the ship which has an initial uncertainty of the value. Additionally, the height above water level depends on the draft of the ship, which is also transmitted by the AIS. The water level depends on the discharge of the Elbe river and the tide. Generally, the water level is assumed to be between the long-term mean high and long-term mean low water level.
Second largest source of uncertainty is the apparent wind direction and apparent wind speed used in the model. The apparent wind itself is calculated from the horizontal wind velocity vector and the ship movement vector. In most cases, the magnitude of the ship movement vectors is large compared to the wind velocity vector. Consequently, the uncertainty of the apparent wind is dominated be the uncertainty of the ship's speed and course.
The smallest source of uncertainty is the uncertainty of the measured trace gases. For NO_x, the uncertainty of the derived NO_2/NO_x ratio is another important factor for the overall uncertainty of the derived emission rate. As the NO_2/NO_x ratio is in the denominator of equation 5.4, even a small uncertainty of the ratio can lead to significant changes in the estimated NO_x concentration. Generally it is assumed the NO_2/NO_x ratio is the same for all ships, which is also supported by the compact correlation found in Figure 5.10. However, the ship type and operation mode of the engine could possibly also have an influence on this ratio.

Results

Between April 2018 and May 2019 a total of 7402 passing ships were identified and assigned to a peak in the NO_2 time series measured by the Heidelberg LP-DOAS. For SO_2 the amount of detected peaks is smaller, because not all ship passages (e.g. passages of inland ships) cause an increase in SO_2 which is detectable as a peak. In this time period there were only 233 days of measurements, due to technical problems with the instrument, e.g. overheating light source during the summer months. Additionally on some days measurements were not possible due to storms or thick fog. Most of the measurements took place between June 2018 and February 2019, while before and after there were only individual days of measurements.
For each ship passage, the emission rates of SO_2, NO_2 and NO_x were calculated. This dataset has then been filtered to remove non-physical results, e.g. very high emission rates of several tons per second. These non-physical results are obtained under circumstances where the assumptions made for the Gaussian plume model do not reflect the situation

Table 5.3: Uncertainties of the input parameters used in the Monte-Carlo-Simulations.

Abbreviation	Name	Calculation of value
σ_{lon}	ship extent in longitudinal direction	$\frac{1}{2} \cdot (\lvert length \cdot \sin(heading) \rvert + \lvert width \cdot \cos(heading) \rvert)$
σ_{lat}	ship extent in latitudinal direction	$\frac{1}{2} \cdot (\lvert length \cdot \cos(heading) \rvert + \lvert width \cdot \sin(heading) \rvert)$
σ_H	plume height	$\sqrt{\sigma_{fh}^2 + \sigma_{wl}^2}$
σ_{fh}	funnel height	estimated: 5 m
σ_{wl}	water level	mean high water level - mean low water level
σ_{aw}	apparent wind speed	$\sqrt{\sigma_{v_{wind\,N}}^2 + \sigma_{v_{ship\,N}}^2 + \sigma_{v_{wind\,E}}^2 + \sigma_{v_{ship\,E}}^2}$
$\sigma_{v_{wind\,N}}$	wind speed	standard deviation of northern wind component
$\sigma_{v_{wind\,E}}$	wind speed	standard deviation of eastern wind component
$\sigma_{v_{ship\,N}}$	ship speed	estimation based on 0.514 $\mathrm{m\,s^{-1}}$ uncertainty in speed and 10° uncertainty in heading
$\sigma_{v_{ship\,E}}$	ship speed	
$\sigma_{\theta_{aw}}$	apparent wind direction	estimated: 10°
$\sigma_{stability}$	stability	atmospheric dispersion parameters of class with lower stability and higher stability than the assigned class
σ_{NO_2/NO_x}	NO_2/NO_x ratio	standard error of the slope (0.006)
$\sigma_{c_{meas}}$	DOAS measurement error	individual DOAS measurement error for each trace gas mean value for NO_2 1.5 % mean value for SO_2 17.7 % mean value for $O_3 < 0.1$ %

during the measurement and the shape of the calculated plume does not match the real plume.

To eliminate such cases before further investigation, three criteria have been defined. If one of these criteria is violated for a single input parameter j for a given individual measurement, the derived emission rate is omitted from the further analysis. The criteria are:

1) $mean_{C\,j}/C_{model}$ has to be between 0.8 and 1.2, to eliminate cases where the uncertainty introduced by the input parameter systematically leads to too high or low derived concentrations.

2) $\sigma_{C\,j}/C_{model}$ has to be lower than 0.4, to eliminate cases that have a high variability if input parameters are varied within their uncertainties.

3) The difference between $max_{C\,j}/C_{model}$ and $min_{C\,j}/C_{model}$ has to be smaller than 1, to eliminate cases with a large spread between minimum and maximum value.

After this quality check a total of 886 NO_x, 1069 SO_2 and 1375 NO_2 emission rates were left for further analysis. The mean uncertainties of the emission rates is 43 % and the median uncertainty is 35 %.

The total number of ships differs because the assignment of a ship to a peak in the trace gas time series is carried out for each trace gas individually, which leads to some differences between SO_2 and NO_2 signal strength. The sulphur content of shipping fuel is limited to 0.10 % S M/M for seagoing and $1{\times}10^{-5}$ % S M/M for inland ships, resulting in ship passes which clearly cause a peak in NO_2 while the enhancement in SO_2 is too low to be detected as a peak. For NO_x the concentrations of ΔNO_2 and ΔO_3 are summed and under circumstances with a high temporal variability within those trace gas concentrations, the background correction for the individual peaks might be erroneous and thus the sum can be zero or even negative. In such cases the NO_x emission rate is not calculated. As an example, Figure 5.12 shows the difference between the unfiltered and filtered dataset for NO_x emission rates for different ship length classes as box plots.

The unfiltered data set shows a large variability, indicated by the large boxes, while the filtered data set clearly shows a lower variability and a narrow distribution around the median of the respective length class. An exception is the 150 m length class, which still shows a high variability. This variability for this length class is caused by dredging ships and will be discussed in more detail in one of the next paragraphs.

Several ships passed the measurement site multiple times or on a regular basis. This allowed to summarize the emission rates for these ships under different measurement conditions (different wind speeds and directions, different stability classes and different water levels). Examples of SO_2 and NO_2 emission rates for ships that passed the measurement site several times are shown in Figure 5.13 as box plots. Generally the 25 % and 75 % percentiles are close to the respective median values, which indicates that the estimation method works consistently. Larger variability of the emission rates of an individual ship

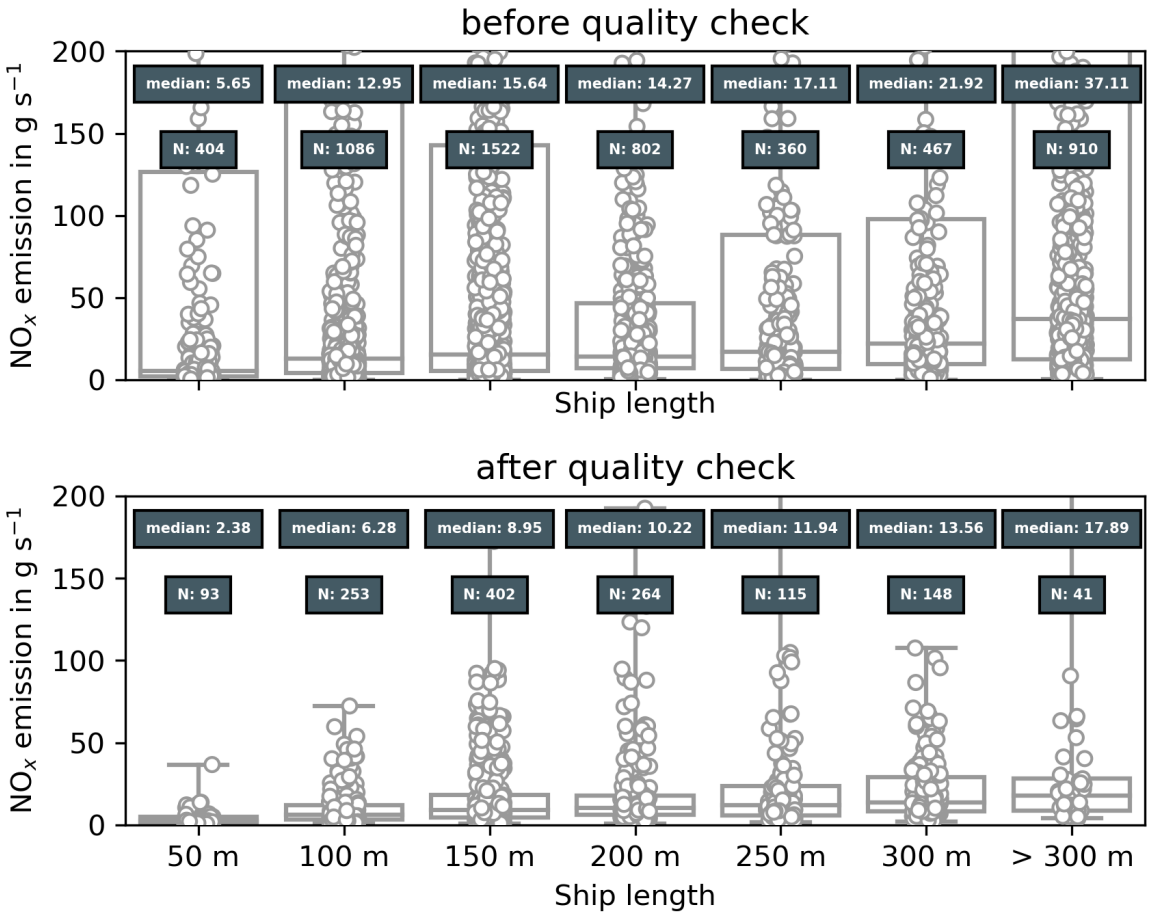

Figure 5.12: Box plot of NO_x emission rates in $g\,s^{-1}$ for different ship sizes. Boxes indicate the 25% and 75% percentile, the line in the middle is the median and the bars show minimum and maximum values. Dots show individual measurements. Dark grey boxes show the median emission rate and total number of observations for this length class.

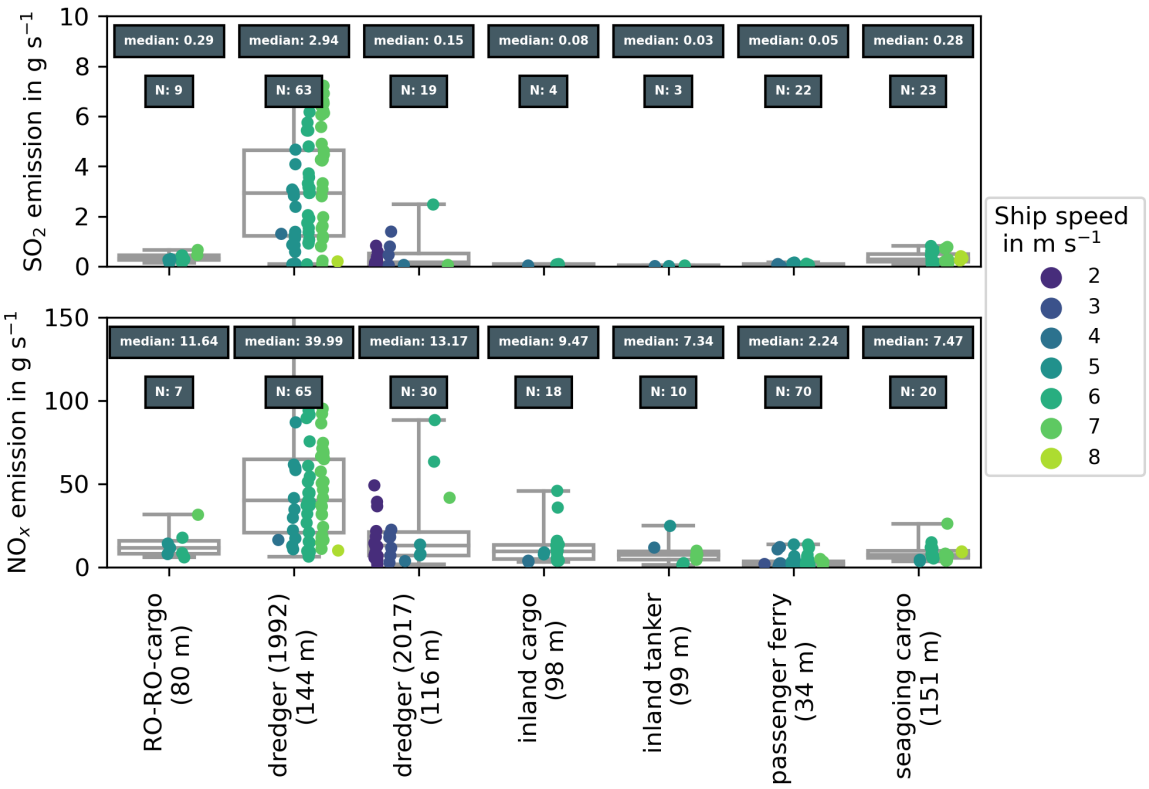

Figure 5.13: Box plot of SO_2 and NO_x emission rates in $g\,s^{-1}$ for individual ships, their respective length is given in brackets. Boxes indicate the 25% and 75% percentile, the line in the middle is the median and the bars show minimum and maximum values. Dots show individual measurements and are colour coded by corresponding ship speed. Dark grey boxes show the median emission rate and total number of observations for this ship.

usually indicate special operating conditions. For example there were two dredging ships, which show a large variability in Figure 5.13. Dredging ships can operate under varying conditions, they do not necessarily only pass by, but can excavate material from the bottom of the river. This additional work might lead to higher engine loads in general or imply the usage of additional auxiliary engines, which in turn increase the total emission of those ships. At other times, these ships might just steam through the light path without carrying out additional work, which explains the low emission rates observed on some passes. The combination of these different operating conditions leads to the high spread seen in the box plots.

Differences in the emission rates of inland and sea ships can be seen in Figure 5.14. The dredging ships have been separated from the other two classes, due to their unique properties described in the previous section. Generally, sea going ships tend to have higher emission rates, with a median of $5.23 \pm 14.0\ g\,s^{-1}$ for NO_x and $0.28 \pm 0.87\ g\,s^{-1}$ for SO_2, while for inland ships the median is $1.93 \pm 8.17\ g\,s^{-1}$ for NO_x and $0.06 \pm 0.19\ g\,s^{-1}$ for SO_2. The differences in SO_2 can be attributed to two different factors. First of all, inland

ships use a fuel with a much lower fuel sulphur content, which automatically decreases the amount of SO_2 emitted per amount of burnt fuel. Secondly, inland ships are much smaller and consume less fuel per unit time. In combination these two factors explain the lower SO_2 emission rates found for inland ships. The difference in the emission rates NO_x can be explained be the difference in size as well as by the different regulations for sea and for inland ships. Most of the NO_x formed during combustion consists of atmospheric nitrogen and oxygen. The amount of NO_x formed is temperature dependent, higher engine temperatures leading to higher amounts of NO_x (Alföldy et al., 2013). For inland ships, there already was a limit for the NO_x emissions in place, while for sea ships there was none at the time the measurements took place. This can also be seen in Figure 5.15, where the NO_x emission rate is categorized for different ship size classes and the median emission rate increases with size. Additionally, the emission rates are also correlated to ship speed, faster ships generally having a higher emission rate (see Figure 5.16). The decrease in the SO_2 emission rate for ship speeds larger than 7 $\mathrm{m\,s^{-1}}$ is probably caused by the low number of observations, which only include a single individual ship, that is not representative for the general fleet.

The determined median SO_2 emission rate for inland ships is larger than the expected SO_2 emissions by those ships. A simple calculation of the expected SO_2 emission rate can be made by multiplying the fuel sulphur content with the amount of fuel used per unit of time. Table 5.5 shows those calculations for inland diesel fuel and fuel which qualifies for the SECA limit of 0.10 % S M/M. The observed median SO_2 emission rate for inland ships is 0.06 $\mathrm{g\,s^{-1}}$, which is considerably higher than the expected SO_2 emission rate (0.0009 $\mathrm{g\,s^{-1}}$) for the typical fuel consumption of an inland ship and still too high when assuming the typical fuel consumption of a much larger ship. However, it has to be kept in mind that the SO_2 emission rates, especially for inland ships, are biased towards high emitters, as some ships can only be identified in the NO_2 time series, while there is no detectable peak in the SO_2 time series. Ships with low SO_2 emissions are therefore under-represented in the data set. In order to calculate a more representative mean SO_2 emission rate for inland ships, the total number of observed inland ships has to be taken from the NO_2 dataset instead, and all cases without an associated SO_2 emission rate are treated as zero SO_2 emission. The total number of observed inland ships would then be 296 (identified from the NO_2 peaks and with valid NO_2 emission rate) and 220 of them would be treated as zero SO_2 emitters. This results in a mean SO_2 emission rate of 0.03 $\mathrm{g\,s^{-1}}$ with and median emission rate near zero, which means the SO_2 emissions for inland ships are often below the detection limit of the LP-DOAS instrument. For sea going ships the method works better and the median SO_2 emission rate (0.28 $\mathrm{g\,s^{-1}}$) lies in the range estimated in Table 5.5.

For 26 individual ship passages (excluding dredging ships), the derived SO_2 emission rates are above the upper limit estimated in Table 5.5, which possibly indicates that those ships

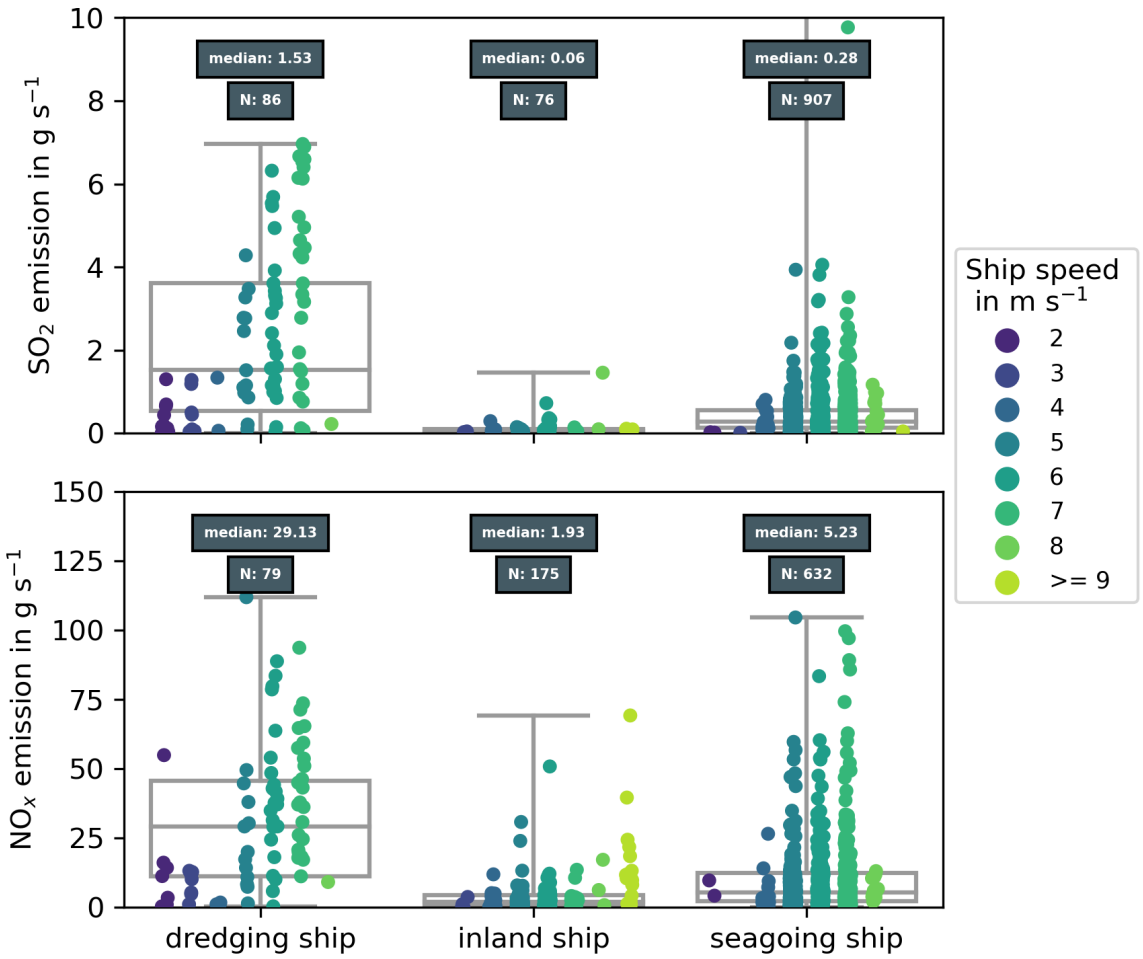

Figure 5.14: Box plot of SO_2 and NO_x emission rates in $g\,s^{-1}$ for different ship types. Boxes indicate the 25% and 75% percentile, the line in the middle is the median and the bars show minimum and maximum values. Dots show individual measurements and are colour coded by corresponding ship speed. Dark grey boxes show the median emission rate and total number of observations for each ship type.

use fuel which does not comply with the SECA limit of 0.10 % M/M or indicates a very large fuel consumption.

In most cases emission factors are reported instead of emission rates. Emission factors specify the mass of released air pollutant per mass of burnt fuel. To compare these two different quantities, further knowledge of the fuel consumption is required. In Table 5.4 the derived emission rates are compared to emission factors of other studies under the assumption of two different fuel consumption scenarios. The lower value describes the typical fuel consumption of an inland ship (about 165 $kg\,h^{-1}$) and the upper value describes the fuel consumption of a large container ship, with carrying capacity of roughly 14.000 TEU, at a speed of 7 $m\,s^{-1}$ (2000 $kg\,h^{-1}$) (Notteboom and Vernimmen, 2009). The largest ships have a mean speed of 6 $m\,s^{-1}$, therefore the assumed high fuel consumption

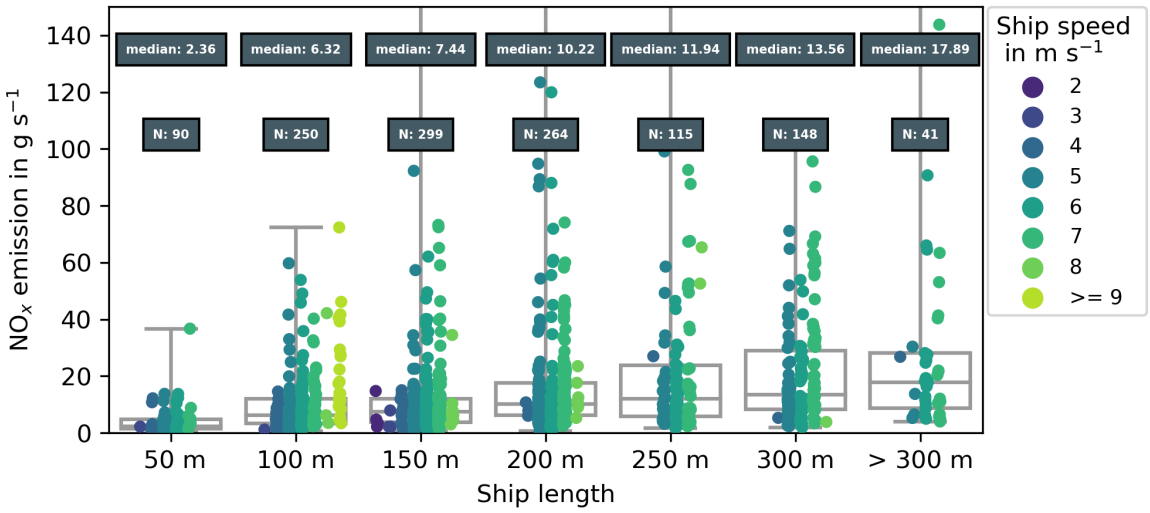

Figure 5.15: Box plot of NO_x emission rates in $g\,s^{-1}$ for different ship lengths. Boxes indicate the 25% and 75% percentile, the line in the middle is the median and the bars show minimum and maximum values. Dots show individual measurements and are colour coded to corresponding ship speed. Dark grey boxes show the median emission rate and total number of observations for this length class. Data of dredging ships has been excluded.

scenario should be interpreted as an upper limit of the fuel consumption.

In all cases the median of the derived emission rates lies within the range estimated using the emission factors of other studies, although always closer to the lower bound. This is reasonable, as most of the passing ships are sea ships with a higher fuel consumption than inland ships, consequently exceeding the estimate of the low fuel consumption scenario. At the same time most of the ships do not belong to the largest ship size class with the highest fuel consumption and consequently are below the estimated upper limit.

A direct comparison of the derived emission rates in this study to the derived emission rates of Berg et al. (2012). shows larger differences. Berg et al. (2012) found a mean emission rate of $11.4 \pm 7.8\ g\,s^{-1}$ for NO_2 and $14.6 \pm 9.1\ g\,s^{-1}$ for SO_2, while in this study the mean NO_2 emission rate is $1.5 \pm 2.9\ g\,s^{-1}$ and the mean SO_2 emission rate is $0.6 \pm 1.1\ g\,s^{-1}$. Berg et al. (2012) observed transects of ship plumes on the open seas, where the fuel sulphur limit at the time was 1.0 % M/M, which is a factor of 10 higher than the fuel sulphur limit relevant for the measurements in this study. Consequently, the emission rates of SO_2 should also be higher by roughly a factor of ten. Additionally, ships on the open seas travel at higher speeds than at the measurement site in Wedel, which increases the fuel consumption und consequently also increases the SO_2 emission rates. Considering the different fuel sulphur content and different speeds, both mean emission rates agree within their respective uncertainties.

The differences in the NO_2 emission rates can be explained by the age of the observed

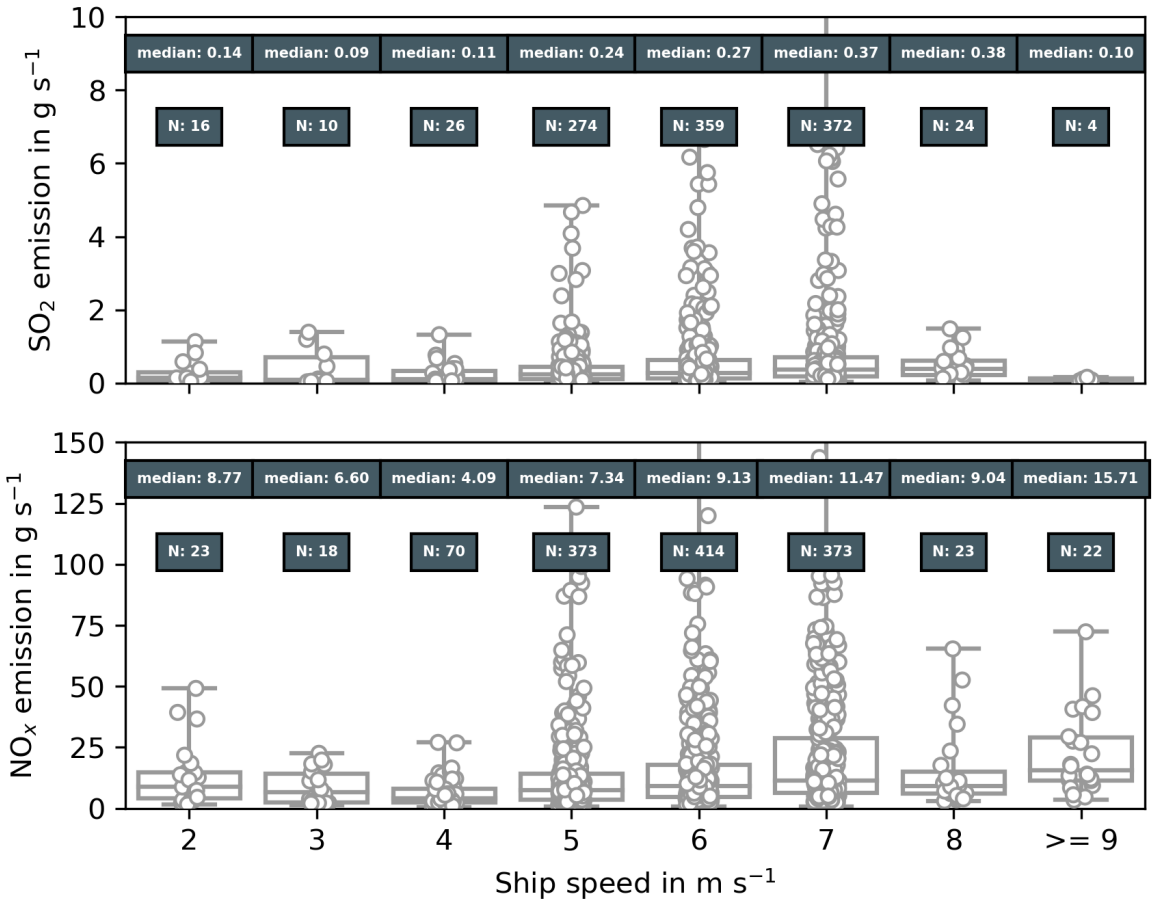

Figure 5.16: Box plot of SO_2 and NO_x emission rates in $g\,s^{-1}$ for different ship speeds. Boxes indicate the 25% and 75% percentile, the line in the middle is the median and the bars show minimum and maximum values. Dots show individual measurements. Boxes show the median emission rate and total number of observations for each ship speed.

Table 5.4: Comparison of emission rates derived from emission factors of other studies for two different assumed fuel consumptions. The lower value is for a fuel consumption of 165 $kg\,h^{-1}$, which is typical for inland ships. The upper value is for a fuel consumption of 2000 $kg\,h^{-1}$ which is roughly the fuel consumption of a large container ship (14.000 TEU carrying capacity) at a speed of 7 $m\,s^{-1}$ (Notteboom and Vernimmen, 2009).

Study	mean NO_x emission factor in $g\,kg^{-1}$ fuel	NO_x emission rate in $g\,s^{-1}$	number of evaluated ships
Moldanová et al. (2009)	73.4	3.4 - 40.8	1
Williams et al. (2009)	66.4 ± 9.1	3.0 - 36.9	> 200
Alföldy et al. (2013)	53.7 ± 22.3	2.5 - 29.8	497
Diesch et al. (2013)	53 ± 27	2.4 - 29.4	139
Beecken et al. (2014)	66.6 ± 23.4	3.1 - 37.0	174
Pirjola et al. (2014)	64.3 ± 24.6	2.9 - 35.7	11
Beecken et al. (2015)	58 ± 14.5	2.7 - 32.2	466
This study	-	mean 11.0 median 4.6	886
		mean seagoing 10.2 median seagoing 5.2	632
		mean inland 4.5 median inland 1.9	177

plumes. In older plumes emitted NO can already react with atmospheric O_3 to form additional NO_2. In this study, the plumes are measured shortly after their emission, while (Berg et al., 2012) probably measured older plumes. Comparison of the mean NO_x emission rate (11.0 ± 16.1 $g\,s^{-1}$) with the NO_2 emission rate of Berg et al. (2012) shows much better agreement between both. This hypothesis is also supported by the calculated NO_2/NO_x ratio of 0.138, which indicates that most of the emitted NO_x is emitted as NO and only then reacts with atmospheric ozone to form NO_2.

Generally, the emission rate derived from an individual measurement is prone to errors. The main reasons are the geometry of the light path and the assumptions made in the modelling of the plume expansion and dispersion. A plume only affects a small part of the light path and the measured concentrations are strongly influenced by the background variability. A shorter light path, which only covers the main shipping lane and less unpolluted air masses, would be beneficial to detect smaller enhancements of NO_2 and SO_2. This would increase the chances of detecting ship plumes of passing ships, even for ships with low emission rates.

The main source of the uncertainty is the plume modelling, especially the uncertainty of the exact stack position and exact stack height. While the position of the ship's AIS receiver is known, the exact position of the stack on the ship is unknown, which results

Table 5.5: Estimate of SO_2 emission rates for fuels with different fuel sulphur content, calculated for different fuel consumption under the assumption that all sulphur is converted to SO_2 during combustion. Lower value is for a fuel consumption of 165 $kg\,h^{-1}$, which is typical for inland ships. Upper value is for a fuel consumption of 2000 $kg\,h^{-1}$ which is roughly the fuel consumption of a large container ship at a speed of 6 $m\,s^{-1}$ (Notteboom and Vernimmen, 2009), which is the typical speed for the largest passing vessels.

Source	Fuel type	Fuel sulphur content in % M/M	SO_2 emission rate in $g\,s^{-1}$
Estimation	SECA limit	0.1	0.09 - 1.16
	Diesel fuel for inland shipping	1×10^{-5}	0.0009 - 0.0116
This study	-	-	mean 0.44 median 0.25 mean seagoing 0.47 median seagoing 0.28 mean inland 0.10 median inland 0.05

in an uncertainty of the plume position and thus the modelled concentrations. A better knowledge of the exact position of the emission source would therefore increase the quality of the derived emission rates and reduce the number of omitted emission rates. Also the Gaussian plume model is a simplification of the turbulent structures within a plume and a more sophisticated modelling approach might improve the quality of the derived emission rates.

At the same time, the repeated measurements of the same ships show a low variability in the derived emission rates and therefore demonstrate the general feasibility of the presented approach to derive emission rates. Also, the value of the calculated emission rates lies in the large number of measured ships and their statistics, which covers different meteorological conditions and allows to characterize the emission behaviour of the passing fleet of ships entering or leaving the port of Hamburg.

5.5 LP-DOAS measurements: Summary and conclusions

Two LP-DOAS instruments were set up in Wedel, about 10 km seawards of the Hamburg harbour to measure ship emissions of NO_2 and SO_2. One of the instruments was newly developed by the company Airyx specifically to measure ship emissions, while the other instrument is a well characterized scientific instrument built by the IUP Heidelberg. Both instruments show a good agreement and the new instrument proofed to be suitable to measure ship emissions.

To demonstrate the capabilities of LP-DOAS measurements for the evaluation and analysis of ship emissions, a method to derive emission rates of NO_2, NO_x and SO_2 from LP-DOAS measurements has been developed and successfully applied to the measurements of the IUP Heidelberg LP-DOAS. Between April 2018 and May 2019 a total number of 7402 passing ships have been identified and assigned to peaks in the trace gas time series. The method uses a Gaussian plume model to simulate the plumes of passing ships and to derive the concentration the instrument would have measured given the assumptions made in the model. The calculated concentration is compared to the measured enhancement in the trace gas to calculate the emission rate. The derived emission rates have then to be filtered for non-physical results, which occur when the assumptions made for the model do not reflect the measurement situation. After filtering a total, of 886 NO_x, 1069 SO_2 and 1375 NO_2 emission rates were derived. The emission rates of inland and seagoing ships have been analysed and compared to each other and showed that sea going ships have higher emission rates than inland ships. Generally the emission rates increase with size and speed of the ship. The uncertainty for a single emission rate are 43 % in the mean and 35 % in median. Repeated measurements of several ships that passed multiple times show a low variability in their emission rates.

To improve the accuracy of the estimate of the ship emission rates, better knowledge of several key parameters will reduce their uncertainty. For example better knowledge of the exact position of the emission location i.e. the position of the ship's funnel, is required. Similarly, better knowledge of the height of the emission, i.e. the height of the funnel of the ship and the water level at the time of measurement, is required. The use of more sophisticated models to describe the shape and evolution of the plume would be of value. Additionally a measurement geometry with a shorter light path across the river would make it easier to detect the pollution plumes from water craft having small emissions and thereby increase the chances of determining emission rates from such vessels.

In comparison to the standard instrumentation at the measurement site, the LP-DOAS does not need to be calibrated and is able to measure under all wind conditions. In contrast to the in situ instruments, the current LP-DOAS system does not measure CO_2, so that emission factors cannot be easily derived from NO_X/CO_2 (SO_2/CO_2) ratios. Therefore a model had to be used to calculate the emission rates of air pollutants. A measurement of the integrated CO_2 concentration along the light path would supersede the need for a dispersion model and should be considered for further technical developments of such measurements.

The study demonstrates that accurate emission rates of ships can be derived from LP-DOAS measurements and that there is much potential in this approach. The emission rates can be used as input for the assessment of the influence of shipping emissions on air quality in regions close to the shipping lanes at the coast or along rivers and canals.

6 Measurements of shipping emissions at the Rhine in NRW

[1] In the EU Life Project Clean Inland Shipping (CLINSH), two methods to measure ship emissions were used. In both cases measurements of in-situ instruments are used. In the first method in-situ instruments were deployed on-board of ships to measure emissions of the engines directly in the exhaust. These measurements were carried out on 40 inland vessels that participated in the project. In addition a method to derive emission rates from on-shore measurements has been developed and will be presented in this study. The retrieval concept for the on-shore measurements is based on the work presented in Krause et al. (2021), but the method has been improved and the algorithm can now be used with data of any in-situ measurement station located in the vicinity of a river. In both cases absolute NO_x emission rates (in $g\,s^{-1}$) have been derived from these measurements.
In total more than 33000 ship passages have been identified and analysed between 2017 and 2021 and are the basis for the future update of the inland waterway vessel emission register of the state of North Rhine-Westphalia. In contrast to more regularly reported emission factors in $g\,kg^{-1}$ or $g\,kWh^{-1}$, the derived NO_x emission rates can be used directly without further assumptions regarding the fuel consumption of the ships and directly reflect the real driving conditions at this part of the Rhine.

6.1 Measurement sites

For the CLINSH project, the State Agency for Nature, Environment and Consumer Protection in North Rhine-Westphalia (LANUV NRW) set up continuous measurement stations in Duisburg and in Neuss, which measure NO_x concentration and meteorological parameters such as atmospheric pressure, humidity, temperature, wind speed and wind direction close to the river Rhine. Instrumentation at both measurement sites along the river Rhine, Duisburg Rhine Harbour (DURH) and Neuss Rhine Harbour (NERH), was identical. Nitrogen oxides were measured with an AC32M from Environnement S.A. (ENVEA) 3.5 m above ground, while meteorological parameters were obtained with a weather station from Lambrecht Meteo GmbH during the course of the campaign. The weather sensor measured wind speed (U) with a rotary anemometer and wind direction (θ) with

[1] Parts of this chapter are based on Krause et al. (2022).

Table 6.1: Specifications of the used instruments.

Measurements at DURH and NERH	Specifications
Nitrogen oxides	NO_x ($NO+NO_2$)
Instrument	AC32M
Manufacturer	Environment S.A. (ENVEA)
Measurement principle	chemiluminescence
Measurement range	NO: 0 –1200 $g\,m^{-3}$
	NO_2: 0 –500 $g\,m^{-3}$
Measurement accuracy	± 15 %
Air sampling height	3.5 m above ground level
Meteorological parameters	wind speed (U), wind direction (θ)
Instrument	EOLOS-IND static weather sensor
Manufacturer	Lambrecht Meteo GmbH
Measurement range	θ: 0 –360 °
	U: 0.1 –85 $m\,s^{-1}$
Measurement accuracy	θ: ± 3 °
	U: ± 0.5 $m\,s^{-1}$
Measurement height	10 m above ground level

a wind vane at 10 m above ground. The time resolution for both measurement types is 0.2 Hz or 5 seconds, more details can be found in Table 6.1.
NO and NO_2 are measured by the chemiluminescence method, and the NO_x concentration is the sum of the measured NO and NO_2 concentration.
Additionally, the measurement stations also are supplemented with AIS (automatic identification system) receivers, which deliver information about the passing ships. Under favourable wind conditions (wind blowing ship plumes towards the in situ systems), both measurement stations show strong enhancements of NO_x when ships pass the measurement site, which can be clearly seen as a peak in the time series. An overview of the measurement sites can be found in Figure 6.1.

6.1.1 Duisburg Rhine Harbour (DURH)

The measurement site in Duisburg is located on the eastern riverbank of the Rhine, close to the Duisburg Harbour (DURH). The predominant wind direction has a westerly component, which transports emissions from ships towards the measurement site most of the time. These emissions cause peaks in the measured NO_x concentration time series (e.g. Figure 6.2) that can be identified and attributed to the source ships. Generally, the measurement site is well located to derive NO_x emission rates from ships steaming along the Rhine. The measured concentration peaks can be differentiated for ships that pass the measurement site in different driving conditions, e.g., ships that drive upstream against the river current and downstream with the river current. Additionally, ships that enter or leave the harbour can also be identified. The measurement station has been set

Figure 6.1: Overview over the two different measurement sites. The upper row shows a satellite image of the DURH station and a picture of the measurement container as seen from the Rhine. The lower row shows a picture of the measurement container in the NERH and a satellite picture of its location.

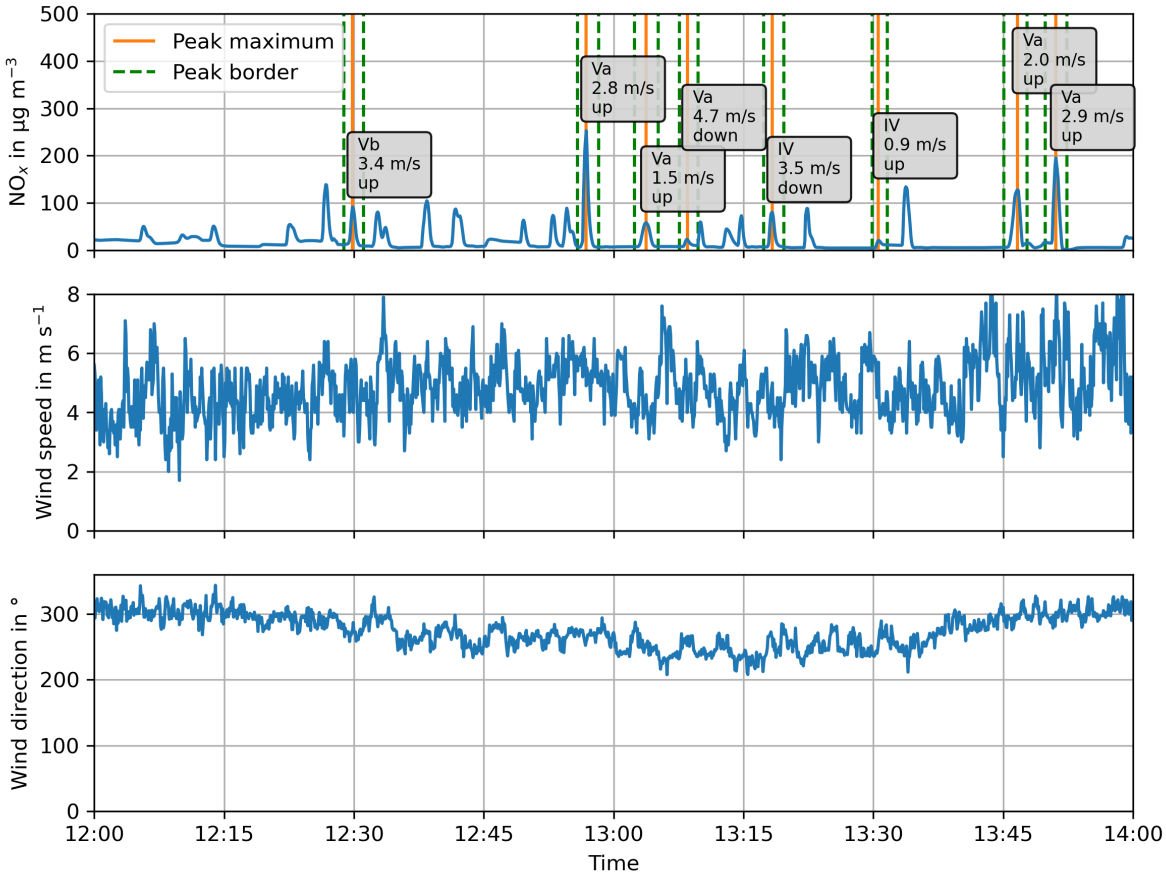

Figure 6.2: Example of the measured NO_x concentration, wind speed and wind direction at DURH. Wind direction 300° means, the wind is coming from south west, blowing over ship plumes from the river towards the measurement station. Ship peaks identified in the NO_x concentration are marked with an orange line, their borders are green dashed lines. The text box at each peak shows the ship class, the speed over ground and the direction of travel. Peaks without a label are most likely also caused by passing ships, but in these cases, unambiguous assignment of a source was not possible.

up in October 2017 and is still active at the time of writing. In this study, measurements from 2017 until the end of 2021 are evaluated.

6.1.2 Neuss Rhine Harbour (NERH)

The measurement site in Neuss is operating within the Neuss Rhine Harbour (NERH) itself, which is located west of the Rhine. Buildings and vegetation block the direct line of sight from the measurement station to the Rhine. The predominant wind direction is south-west. Due to location and wind direction most of the identified peaks stem from ships that are within the harbour area and only a minor part steams from ships that are steaming along the Rhine. Nevertheless, this measurement site is well suited to evaluate the emissions of slow steaming ships within the harbour area and without the influence of river currents. This measurement station was set up in September 2017 and dismantled at the end of 2019. Consequently, the emission rates could only be derived for the years 2017 to 2019.

6.2 Methods

The combination of the different measurements and the received AIS signals enables ship emissions from passing ships to be calculated. The approach uses three consecutive steps, which will be described in the following.

6.2.1 Peak identification

The first step is to identify the peaks caused by passing ships. To identify these peaks, a low pass filtered time series is calculated from the measured time series using a running median with a window length of 5 minutes. This low pass time series describes the changes in the background concentration caused by meteorological factors and other emission sources, but excludes the short-term variation caused by passing ships. The low pass filtered time series is then subtracted from the measured time series, resulting in a time series, which is close to zero on average, but still shows the sharp peaks caused by the passing ships. For those peaks it is then checked, if they exceed a defined threshold, to ensure they are actual enhancements and not only noise in the measurements. In this case, the threshold was defined as 2 ppbv. For each identified peak, the time of occurrence (t_{peak}), the peak width, and the height of the maximum above the background concentration is determined.

6.2.2 Ship assignment

In the second step the respective source ship of a peak is identified. For each peak, all ships within a 5 km radius around the measurement site and up to 5 minutes before the peak maximum are identified using the AIS signals. For each ship, the corresponding AIS signals within the given time frame and radius around the measurement site are collected and then interpolated to a one second time resolution. For each of these interpolated AIS signal positions, a trajectory is calculated to assess whether emissions caused at that specific ship position could have been transported to the measurement site by the wind. The wind speed and direction used for the trajectories are the 30 min averages of the wind measured at the measurement site. Each trajectory is calculated for the period between the time stamp of the AIS signal (t_{AIS}) and the time of the peak maximum (t_{peak}). It is then checked, whether the trajectories end within a 50 m radius of the measurement site. When only the trajectories of a single ship end close to the measurement site in the given time frame, the ship is assigned as the respective source of the peak.
In case the trajectories of several ships end within the 50 m radius around the measurement site, the peak is neglected for further analysis, as an unambiguous assignment of a single source is not possible. Once a ship has been identified as the source of the NO_x peak, all the information for that ship passage is assigned to the peak. To ensure the whole ship passage is registered, the first assigned ship position is the position transmitted 180 seconds before t_{AIS} and the last assigned position is the position 180 seconds after t_{peak}.

6.2.3 Calculation of emission rate

In the third and last step, the NO_x emission rate for each peak assigned to a source ship is calculated. The stations only measure the concentration of NO_x at the measurement site and not at the stack of the ship, therefore, a model has to be applied to estimate the emission rate from the concentration enhancement found at the measurement site. A simple approach is to assume that the plume of the ships can be described by a Gaussian-puff-model, similar to Equation 2.4:

$$C(x,y,z) = \sum_{i=1}^{N} \frac{(Qdt)_i}{(2\pi)^{3/2}\sigma_x\sigma_y\sigma_z} \cdot \exp\left(-\frac{(x-U\cdot(t-dt))^2}{2\sigma_x^2}\right) \cdot \exp\left(-\frac{y^2}{2\sigma_y^2}\right) \cdot \left[exp\left(-\frac{(z-H)^2}{2\sigma_z^2}\right) + exp\left(-\frac{(z+H)^2}{2\sigma_z^2}\right)\right] \tag{6.1}$$

where the concentration at a point ($C(x,y,z)$) can be described as a function of the emission rate (Q), the dispersion due to atmospheric stability (σ_x, σ_y, σ_z), the length of time of the emission (dt) at a certain source point (x=0, y=0), funnel height (H), the total transport time (t) and the wind speed (U). The wind direction is taken to be along x. The model releases a puff of pollutants at the ship's position, which is then transported by the

wind for an amount of time $(t - dt)$ and dispersed according to the current atmospheric stability. To model a time step $t - dt$ is used instead of t to simulate that the ship has just arrived at the new location and was not stationary at the latest position. The time (t) is different for each ship position and is always the time of occurrence of the peak maximum (t_{peak}) minus the time of the respective AIS signal (t_{AIS}). The result is a concentration field caused by the emission of pollutants at the specific ship location for a time step dt and transported for the time $t - dt$. This procedure is then repeated for all ship positions. The calculated concentration fields then describe how the plume developed during the ship passage (e.g. Figure 6.3).

The real emission rate is unknown and the model is only used to describe the dispersion and transport of the emitted pollutants. To model the dispersion and transport, the model is run with an arbitrary but constant emission rate (Q_{model}). The height of the plume centre is approximately at the height of the funnel above the water level, assuming that the plume quickly bends down due to wind and movement of the ship. The height is also assumed to be equal for all ships and was set to 5 m above the mean water level. The dispersion parameters are chosen according to atmospheric stability, which has been determined using the wind speed at the measurement site and and incoming global radiation during day and cloud coverage during night from a nearby weather station of the German Weather Service located at the Düsseldorf-Airport (DWD Climate Data Center, 2022a,b). In order to derive the emission rate, the integrated measured concentration, i.e. the area under the peak (C_{meas}), is compared to the modelled concentration at the measurement site, i.e. the area under the modelled peak (C_{model}). C_{meas} has already been corrected for the fluctuations in the background NO_x concentration. The background is assumed to be the mean value of the NO_x concentration 30 seconds before and after the peak.

Assuming the model sufficiently describes the ship plume, the only difference between modelled concentration and measured concentration is caused by the different emission rate. Therefore, the real emission rate of the ship (Q_{meas}) can be estimated by the following equation:

$$Q_{meas} = \frac{C_{meas}}{C_{model}} \cdot Q_{model} \tag{6.2}$$

This approach assumes, that the emission rate is constant for the whole modelled time domain. An example is shown in Figure 6.4.

6.2.4 Quality control and uncertainty of the NO_x emission rates

Not in all cases the assumptions made within the model truly reflect the conditions at the time of measurement. To assess the quality of the derived emission rate, Monte-Carlo-simulations are performed to assess whether a small change in one of the input

parameters results in a large change of the derived concentration at the measurement site. The parameters varied are wind speed, wind direction, atmospheric stability and the position of the ship in longitude, latitude and height. Each of these parameters is changed within the uncertainty ranges given in Table 6.2. For each changed parameter, the derived integrated peak concentrations are then compared to the integrated peak concentration of the reference simulation. If the Monte-Carlo-simulations and the reference simulation do not show large deviations, the derived NO_x emission rates for that specific case are used for further evaluation.

The uncertainty of the derived emission rate is given by:

$$\sigma_Q = \sqrt{\left(\frac{\partial Q_{meas}}{\partial C_{meas}} \cdot \sigma_{C\,meas}\right)^2 + \left(\frac{\partial Q_{meas}}{\partial C_{model}} \cdot \sigma_{C\,model}\right)^2} \tag{6.3}$$

where σ_{Cmeas} is the uncertainty of the measured integrated peak trace gas concentration and σ_{Cmodel} is the uncertainty of the modelled integrated peak trace gas concentration. The uncertainty of the model is defined as:

$$\sigma_{C\,model} = \sqrt{\sigma_{C\,U}^2 + \sigma_{C\,\theta}^2 + \sigma_{C\,stability}^2 + \sigma_{C\,lon}^2 + \sigma_{C\,lat}^2 + \sigma_{C\,H}^2} \tag{6.4}$$

where each σ_{Cj} is the standard deviation of the modelled trace gas concentrations of the Monte-Carlo-simulations with respect to changes of an individual input parameter (j). In the Monte-Carlo-simulations, each parameter is varied individually, therefore possible interactions between changes of more than one parameter at a time are neglected. For each parameter, the resulting concentrations of a set are summarized by the mean value ($mean_{Cj}$), the standard deviation (σ_{Cj}) and the minimum (min_{Cj}) and maximum value (max_{Cj}). These values are then compared to the reference simulation of the unperturbed input parameters. To be evaluated further, the following five criteria must be met by the set of Monte-Carlo-Simulations for each input parameter:

1) $mean_{Cj}$ / C_{model} must be within between 0.5 and 1.5, to eliminate cases with a systematic deviation caused by the uncertainty of a single input.

2) σ_{Cj} / C_{model} must be lower or equal to 1, to eliminate cases with a high variability caused by the uncertainty of a single input.

3) The difference between min_{Cj} / C_{model} and max_{Cj} / C_{model} must be lower than 2, to eliminate cases with a large spread between minimum and maximum of the set due to the uncertainty of a single input.

4) the absolute error of the derived emission rate must be lower than 5 $\mathrm{g\,s^{-1}}$, which eliminates cases, where the uncertainty is on a larger order of magnitude than the emission rate.

5) the relative error of the derived emission rate must be lower than 200 %, which eliminates cases, where the uncertainty is much larger than the emission rate.

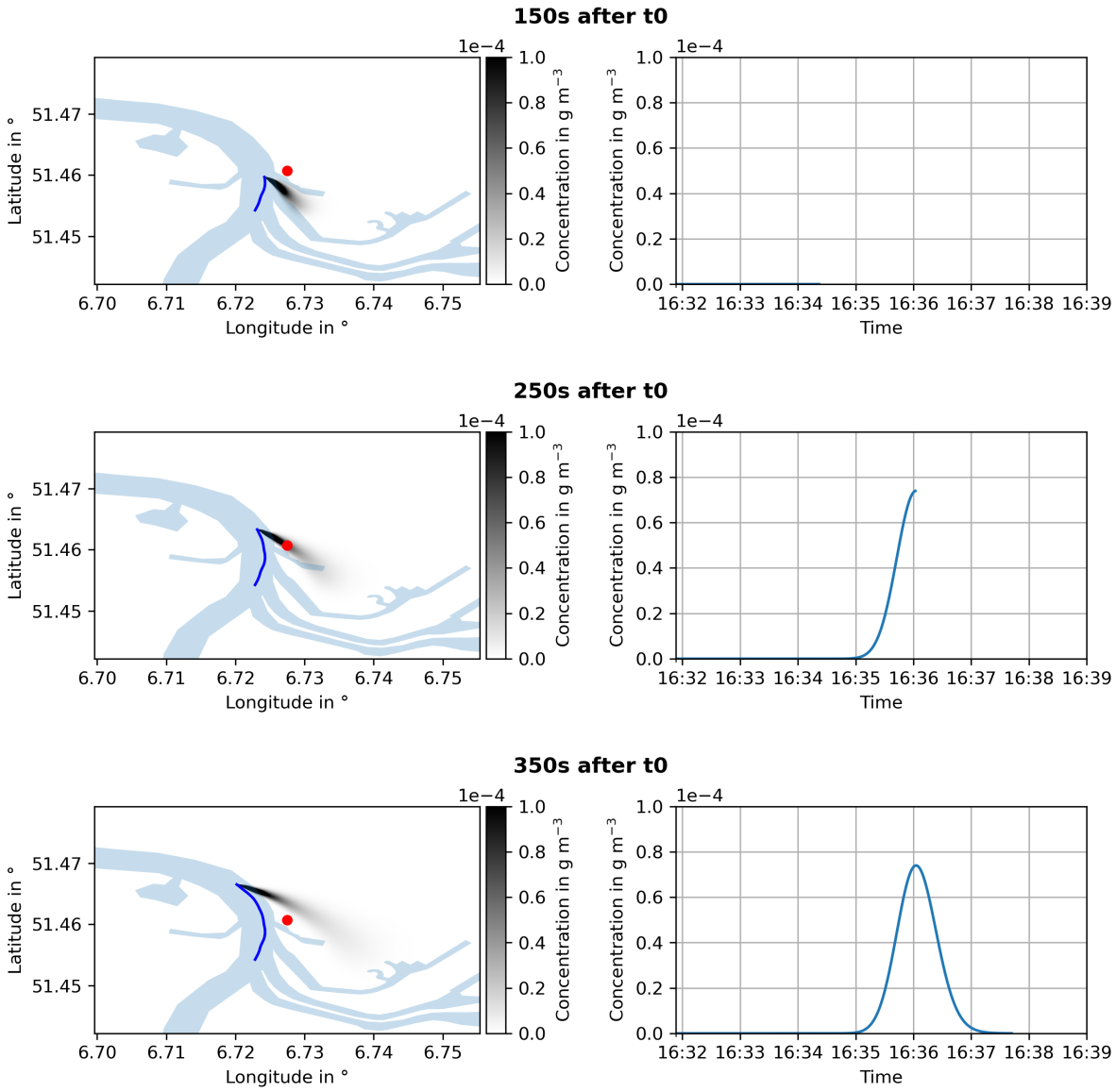

Figure 6.3: Example of a plume simulation for different time steps after the simulation start (t0). The upper, middle and lower panels show the movement of the modelled ship plume 150 s, 250 s and 350 s after the initiation of the plume. The left column shows a horizontal cross section of the modelled plume in 20 m height. The location of the measurement station is marked as a red dot. The blue line in the right column shows the modelled concentration at the location of the measurement station during the model run.

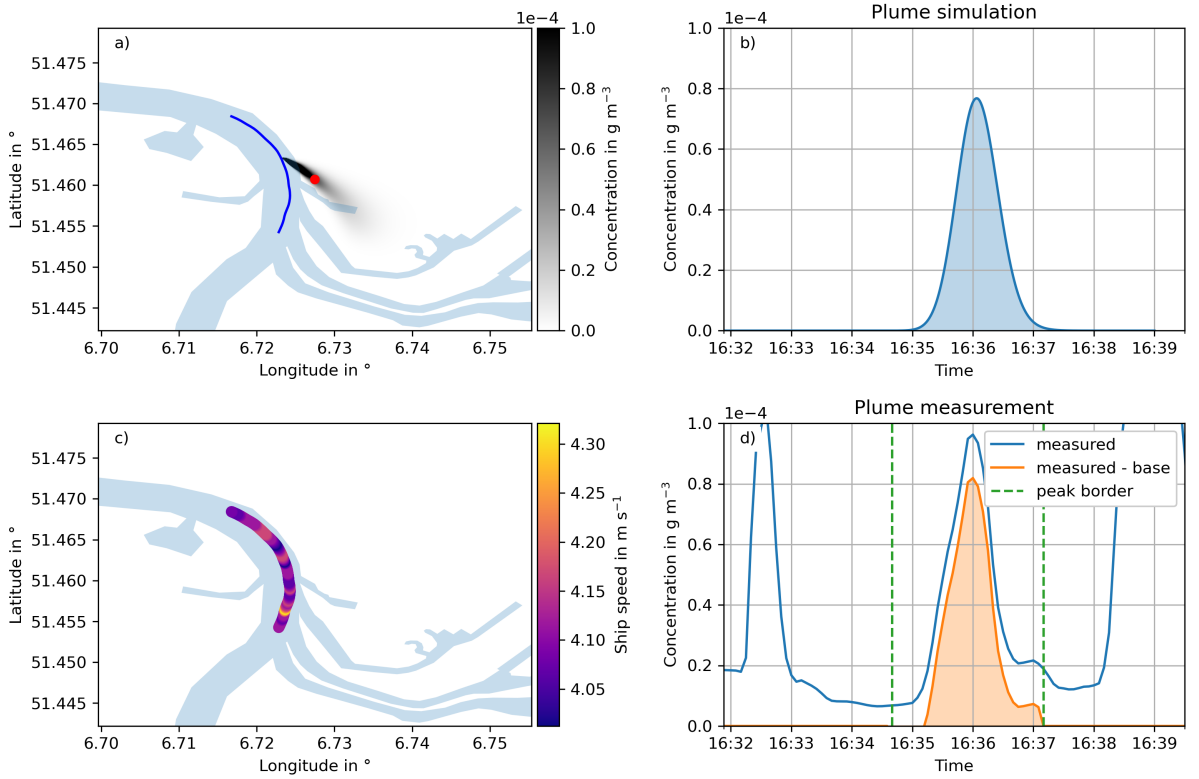

Figure 6.4: An example of a plume simulation for the 22nd August 2018 at 16:36 UTC compared with the measured plume. a) a map of the modelled plume for the time when the highest concentration has been measured. b) a plot of the simulated concentration of NO_x at the measurement site as a function of time. c) a map showing the ship speed over ground for each time step. d) a plot of the measured NO_x concentration as a function of time at the measurement station. The blue line represents the NO_x concentration, and the orange line is the background corrected NO_x concentration of the peak.

Table 6.2: Uncertainties of the input parameters used in the Monte-Carlo-Simulations.

Abbreviation	Name	Calculation of value
σ_{lon}	source position longitude	Uncertainty of the AIS signal, 10 m
σ_{lat}	source position latitude	Uncertainty of the AIS signal, 10 m
σ_H	plume height	$\sqrt{\sigma_{fh}^2 + \sigma_{wl}^2}$
σ_{fh}	funnel height	estimated: 5 m
σ_{wl}	water level	mean high water level - mean low water level
σ_U	wind speed	standard deviation of the wind speed
σ_θ	wind direction	estimated: 10 °
$\sigma_{stability}$	stability	atmospheric dispersion parameters of class with lower stability and higher stability than the assigned class
$\sigma_{c_{meas}}$	uncertainty of the measured peak area	$\sqrt{std(peak)^2 \cdot n}$, where n is the number of nodes used to calculate the peak area

6.3 Results

For Duisburg, a total of 32900 ship peaks has been identified and could be assigned to specific source ships. For 23500 of those peaks it was possible to determine the NO_x emission rate and fulfil the quality criteria. In Neuss, 5500 peaks have been identified and the respective emission rates have been derived, in 3200 cases those derived NO_x emission rates fulfil the quality criteria. The number of identified ship plumes is mainly limited by the wind, as the wind is needed to transport the emitted pollutants towards the measurement site. An additional limitation is the traffic density as in situations of high traffic, an unambiguous identification of a ship plume is often not possible. The derived emission rates were then summarized in the context of the respective CEMT ship class (Table 6.3).

The most common ship classes are IV, Va, Vb and Jowi which together account for approximately 80 percent of the total ship traffic (Figure 6.6). Between 2017 and 2021, there were approximately 256 ship passages every day at the DURH measurement site. As can be seen in Figure 6.7, most ships travelling upstream have a speed over ground of about 3 $\mathrm{m\,s^{-1}}$, while most ships travelling downstream have speeds over ground of about 5 $\mathrm{m\,s^{-1}}$. For the most common ship classes this enables to characterize the NO_x emission rates of the respective class under real driving conditions. For less common ship classes, there are fewer observations, which leads to a higher uncertainty of the summarized NO_x emission rates for these classes. In addition, there might not be enough data to differentiate sufficiently between direction of travel or different speeds.

For the most common ship classes this enables to characterize the NO_x emission rates of the respective class under real driving conditions. For less common ship classes, there are fewer observations, which leads to a higher uncertainty of the summarized NO_x emission rates for these classes. In addition, there might not be enough data to differentiate

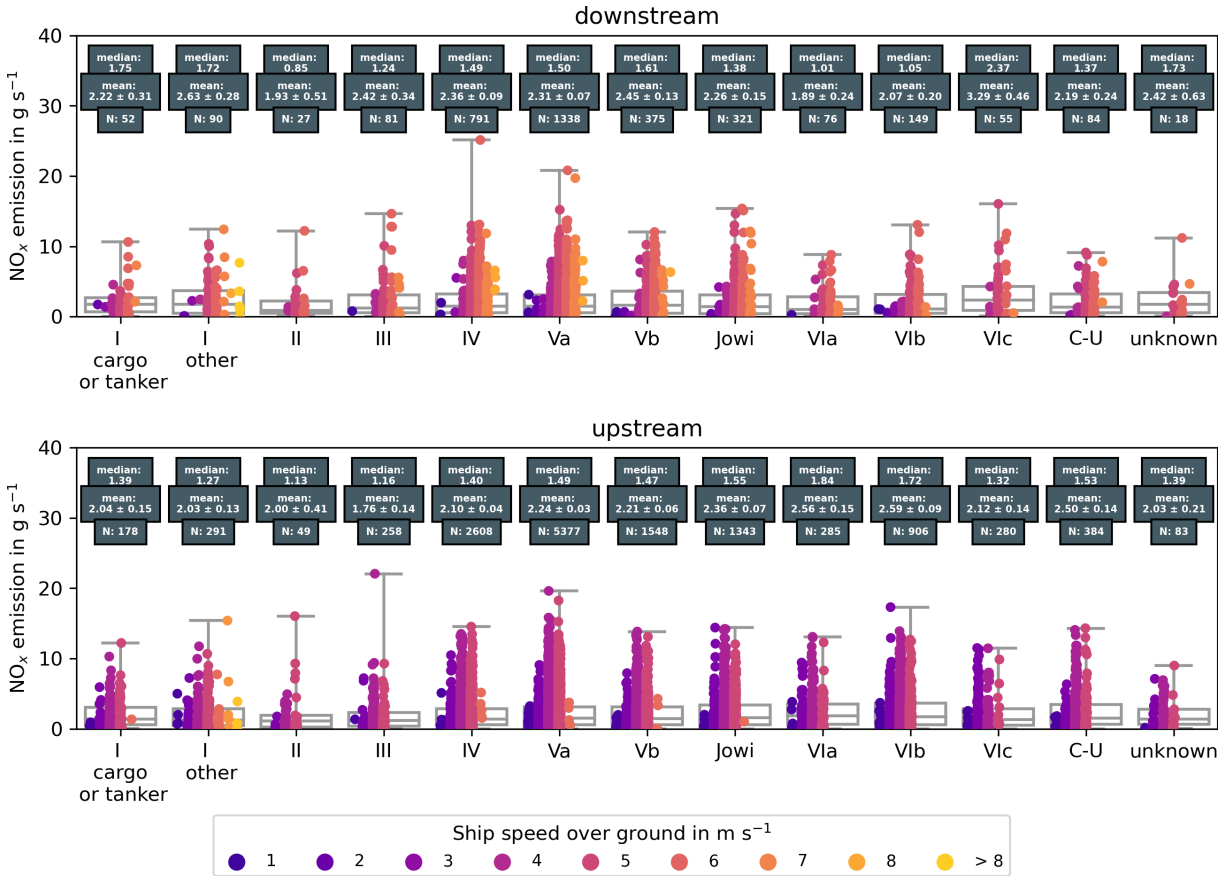

Figure 6.5: NO_x Emission rates for all ship classes, derived from measurements at DURH. Single measurements are colour-coded to the respective mean ship speed during the measurement.

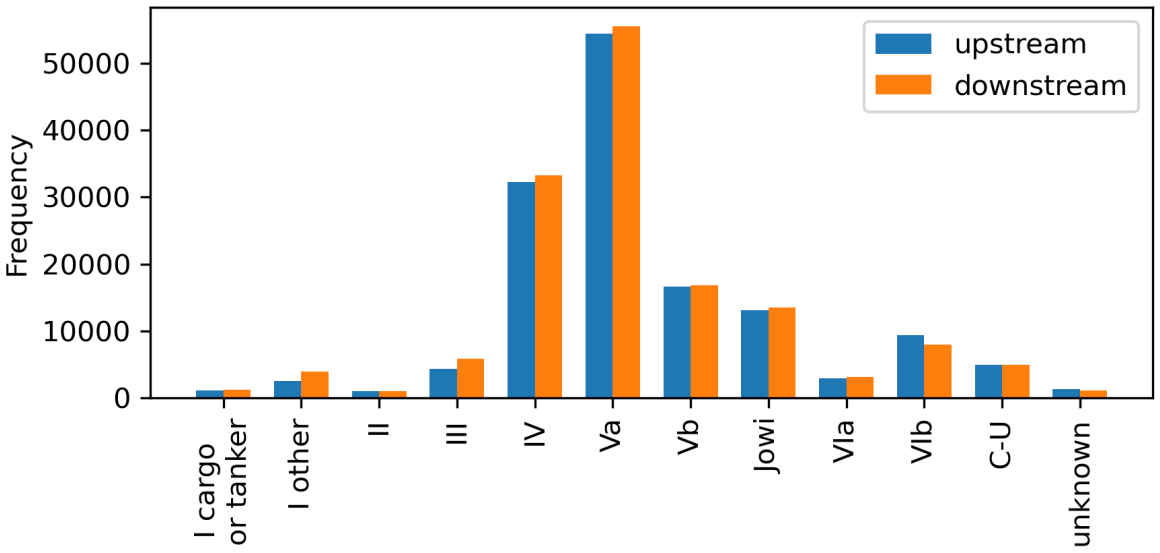

Figure 6.6: Ship traffic and fleet composition at DURH between November 2017 and December 2021. In total 291635 ship passages have been identified.

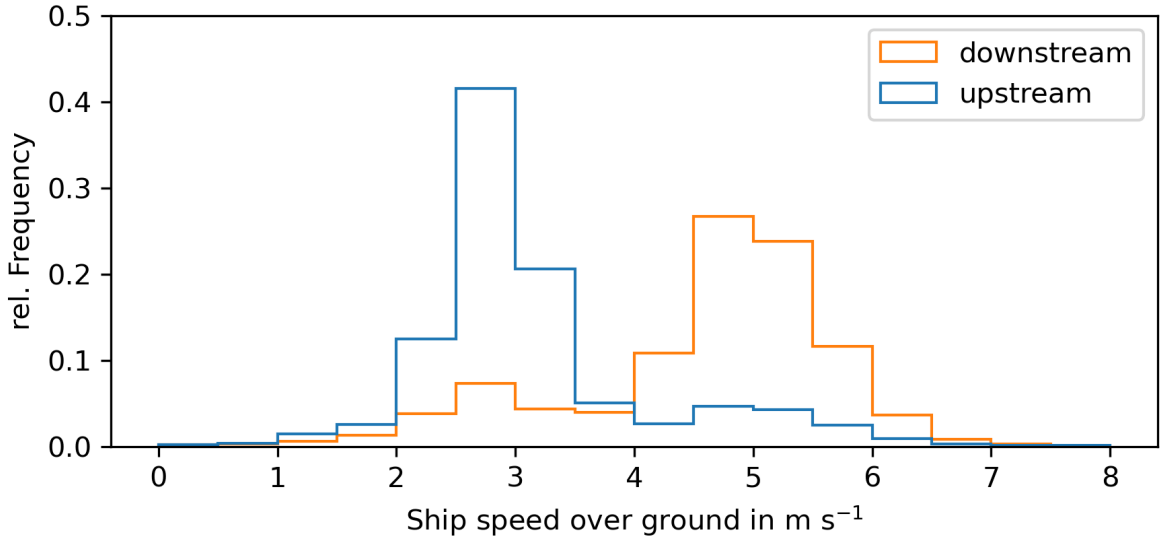

Figure 6.7: Ship speed over ground for all ship passages identified at DURH as a function of direction of travel.

sufficiently between direction of travel or different speeds.

The NO_x emission rates in the context of size are more difficult to summarize. Generally, larger ships show larger NO_x emission rates than smaller ships. At the same time, the larger ships are usually newer and their emissions are regulated, while older ships are subject to grandfathering, which means their engines do not have to comply with new regulations. Only if the engine of an older ship is exchanged, new regulations apply. Due to the long service life of inland ships, a lot of the smaller ships do not fall under the regulations and therefore still show high emissions.

6.3.1 Differences in direction of travel

The speed over ground is correlated with the emission rates, higher speeds leading to higher emissions as expected (e.g. Figure 6.8).

Unfortunately, at the DURH station most of the identified ships are vessels which are travelling upstream. The main wind direction at DURH is south-west which is parallel to the river, and ship plumes are therefore transported along the river. Unambiguous assignment is only possible if there is just a single ship plume that can reach the measurement station. Ships travelling upstream need a longer time to pass through the area, as they are slower than ships travelling downstream. Therefore, in cases of high traffic density, the longer time window of the slower upstream travelling ships increases the chances of an unambiguous identification and results in a larger number of observed ship plumes for that particular direction.

The direction of travel is important when investigating the emissions for a certain speed.

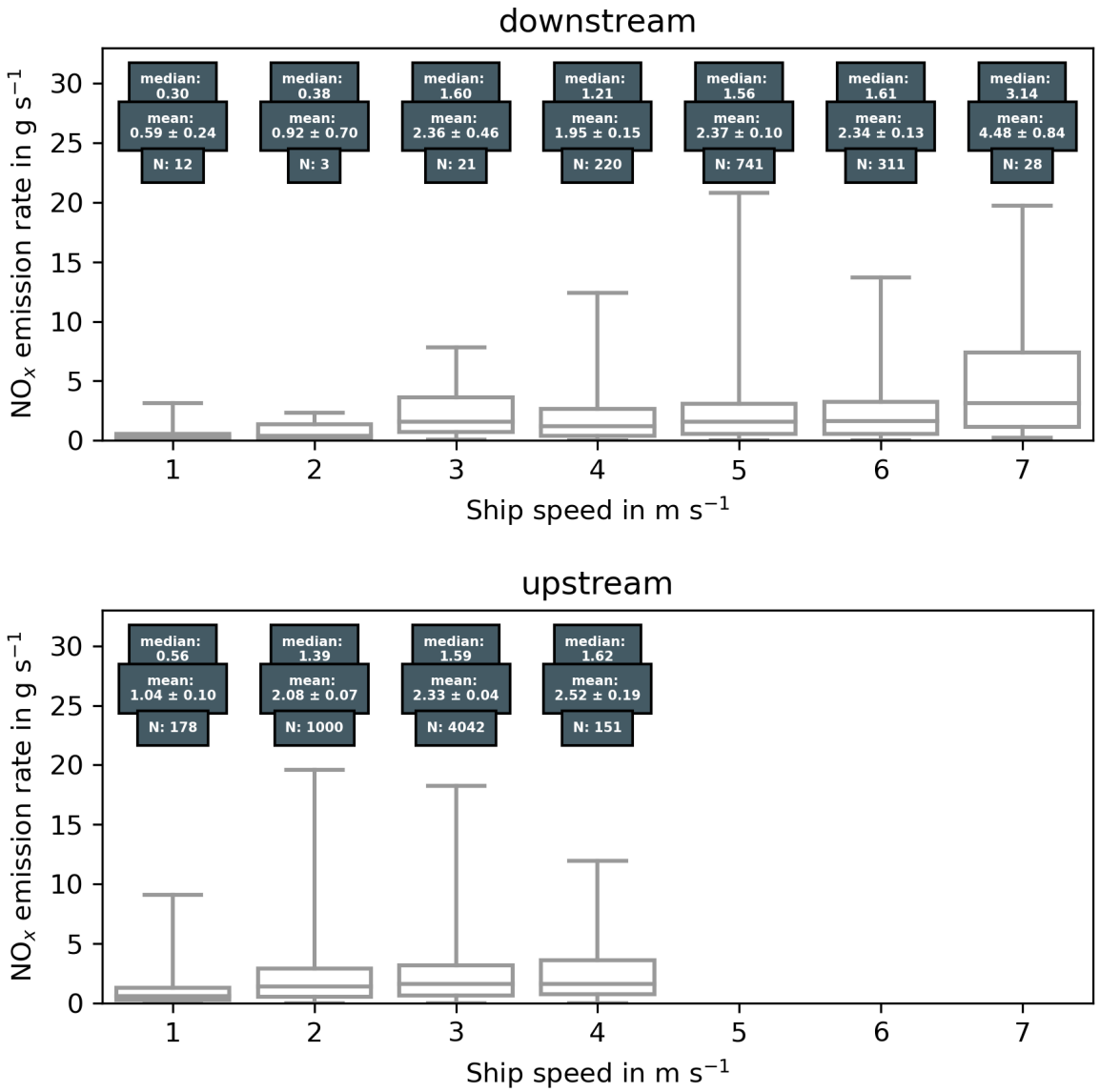

Figure 6.8: NO_x emission rates for ship class Va and their dependence on the direction of travel and ship speed over ground, derived from data measured at DURH.

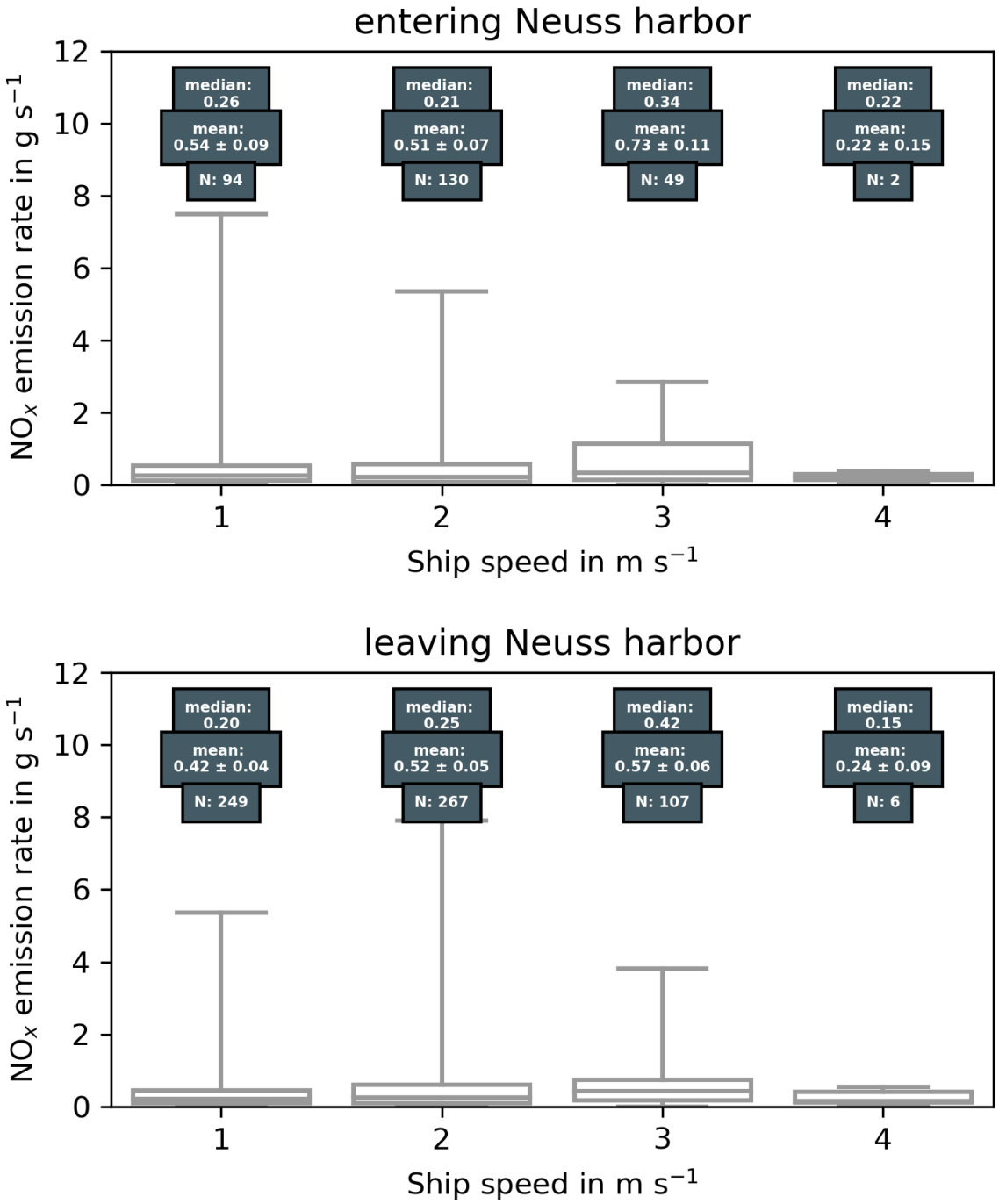

Figure 6.9: NO_x emission rates for ship class IV and their dependence on the direction of travel and ship speed over ground, derived from data measured at NERH.

Table 6.3: Modified ship classification scheme based on CEMT (European Conference of Ministers of Transport, 1992) classes. Ships are categorized by their respective length and width, e.g. a ship longer than 86 m but shorter than 111 m and width between 10 and 12 m is classified as class Va. Additionally coupled units are identified via their Electronic Reporting International (ERI) code which is also transmitted in the AIS signals.

Class	maximum length m	maximum width m	cargo capacity tons
I	39	6	350
II	56	7	655
III	68	9	1000
IV	86	10	1350
Va	111	12	2750
Vb	136	12	4000
Jowi	136	18	5300
VIa	173	12	5500
VIb	194	23	11000
VIc	194	35	16500
Coupled unit (C-U)	motor freighter pushing one barge identified via ERI identifier		
unknown	ships without information about width and / or length		

Ships that travel upstream have to overcome the river current and therefore need more power to achieve the same speeds along the ground compared to ships travelling downstream. With the same speed in water, the engine operating conditions should be similar and independent of direction of travel, therefore the NO_x emission rates should also be similar. A direct comparison for ship classes IV, Va, Vb and Jowi shows, that ships travelling upstream with a speed of about 3 $m\,s^{-1}$ and ships travelling downstream with a speed of 5 $m\,s^{-1}$ have similar NO_x emission rates in their respective size class (shown in Table 6.7), which suggests similar operating conditions. Ships that are not influenced by the current show similar NO_x emission rates independent of direction of travel (e.g. Figure 6.9).

The AIS signals only transmit speed over ground, to calculate the speed in water of the vessels additional information is needed. The Federal Waterways and Shipping Administration (Wasserstraßen und Schifffahrtsverwaltung des Bundes, WSV) operates several gauges to monitor the water level at the Rhine. There is roughly one gauge every 30 km. To get information about the water level and river currents between those gauge stations, mathematical discharge flow models are used. The Federal Institute for Hydrology (Bundesanstalt für Gewässerkunde, BfG) uses the modelling package SOBEK, which is a hydrological model that is used to simulate and solve problems in river management, flood protection, design of canals to model the discharge of the different rivers in Germany. SOBEK is a one-dimensional open-channel dynamic numerical modelling system

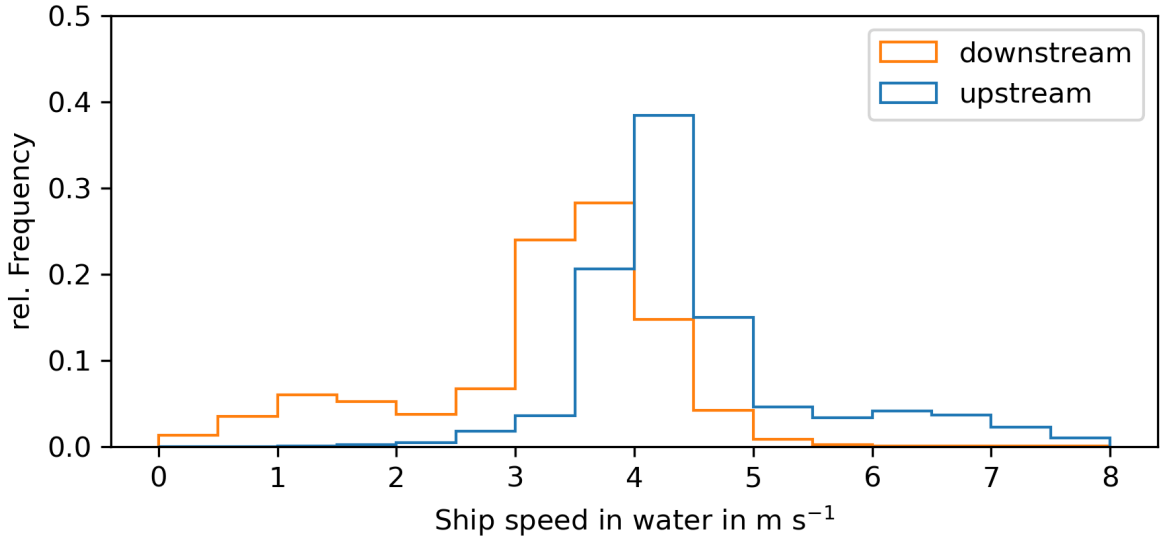

Figure 6.10: Ship speed in water for all ship passages identified at DURH as a function of direction of travel.

which can model unsteady water flow, salt intrusion, sediment transport, morphology and water quality. Outputs of the model are for example, discharge, water depth and flow velocity. To calculate the speed in water (v_{iw}) for each vessel, the information for speed over ground (v_{og}) is merged with the information about the flow velocity (v_{river}) modelled by SOBEK. When a ship is travelling upstream, the speed in water is speed over ground plus flow velocity ($v_{iw} = v_{og} + v_{river}$), as the ship needs to overcome the current to travel upstream. For a ship travelling downstream, the speed in water is the speed over ground minus flow velocity ($v_{iw} = v_{og} - v_{river}$), as the ship travels with the current, which adds to the speed over ground.

Figure 6.10 shows a histogram of the speed in water of all ship passages at DURH as a function of direction of travel. It can be seen, that the speed in water for ships travelling upstream and ships travelling downstream is similar, with a mean of 4.0 and 3.7 m s^{-1}, respectively. A Welch's t-test (unequal variances t-test) shows that the mean speeds in water are not the same on 95 % confidence interval.

A Welch's t-test of the mean of the $log(Q_{meas})$ shows that there is no significant (95 %) difference between ships going upstream and downstream. The logarithm of the emission rates had to be taken, because it closely resembles the normal distribution which is assumed for the test.

To test whether the direction can be neglected when analysing the emission rates as a function of speed in water, the speed in water and speed over ground have been compared for ships travelling upstream and ships travelling downstream. Figure 6.12 shows a scatter plot of $log(Q_{meas})$ as a function of speed over ground. Each measurement is colour coded by the respective direction of travel. Additionally, the histograms of speed over ground

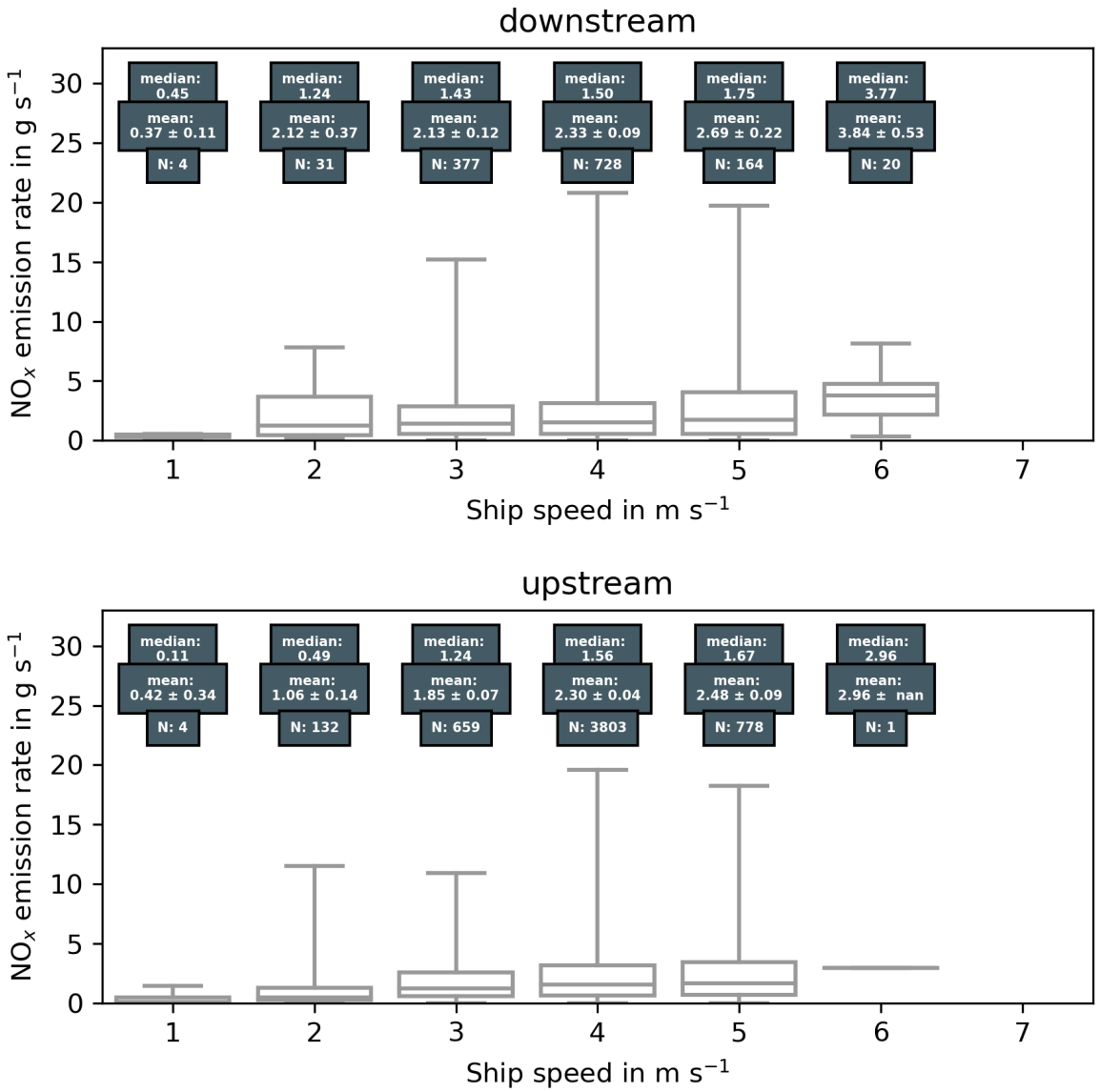

Figure 6.11: NO_x emission rates for ship class Va and their dependence on the direction of travel and ship speed in water, derived from data measured at DURH.

and $log(Q_{meas})$ are shown. The histograms of $log(Q_{meas})$ are very similar and overlap, while the histograms of speed over ground show different distributions and do not overlap. In the scatterplot both directions of travel can be clearly distinguished and each direction forms its own point cloud. Figure 6.12 shows a similar scatter plot but now $log(Q_{meas})$ is plotted as a function of speed in water. Again each measurement is colour coded by the respective direction of travel. Here the directions can't be distinguished in the scatter plot, they form a uniform point cloud, also the histogram of speed in water shows an overlap between both directions of travel. Figures 6.13 and 6.15 show emission rates for different directions of travel as a function of ship speed, averaged for 0.5 $\mathrm{m\,s^{-1}}$ speed intervals. In both cases the mean emission rate is only shown when more than 100 emission rates are observed within the given speed interval. For speed over ground (Figure 6.13), the shown emission rates of the different directions of travel do not overlap at the same speed over ground. In contrast, Figure 6.15 shows that both directions of travel have similar mean emission rates for a given speed in water.

In order to quantify the influence of the ship's speed, either over ground or in water, two Analysis of Variance (ANOVA) were performed. In the first ANOVA, the influence of direction of travel, speed over ground, ship type and the interaction between direction of travel and speed over ground were considered as explanatory variables for the logarithm of the emission rate ($log(Q_{meas})$). The logarithm of the emission rates was used as response variable because it transforms the distribution of the emission rates to a normal distribution, which is a prerequisite for the analysis of variance. The resulting anova tables are shown in Table 6.4 and Table 6.5.

For the first model, where speed over ground is considered as an explanatory variable, it can be seen that $log(Q_{meas})$ is significantly different from 0 (Intercept) and direction, speed over ground and type also have significant influence (95 % level) on $log(Q_{meas})$. The interaction of direction and speed in water is significant on the 90 % level.

In the second model, where speed in water is considered as an explanatory variable instead, $log(Q_{meas})$ is significantly different from 0 (Intercept). Speed in water and type are also significant on the 95 % level, while direction and the interaction term direction and speed in water are not significant on the 95 % level.

To summarize, the mean speed over ground is significantly different for each direction and the mean of $log(Q_{meas})$ is not significantly different for the different directions. The ship speed shows a significant influence on $log(Q_{meas})$, and when the ship speed over ground is considered, the direction and the interaction of direction of travel and ship speed over ground is also significant. When ship speed in water is considered the direction and the interaction of direction and speed in water is not significant. Consequently, when analysing the emission rates as a function of speed in water, both directions of travel can be considered to stem from the same population.

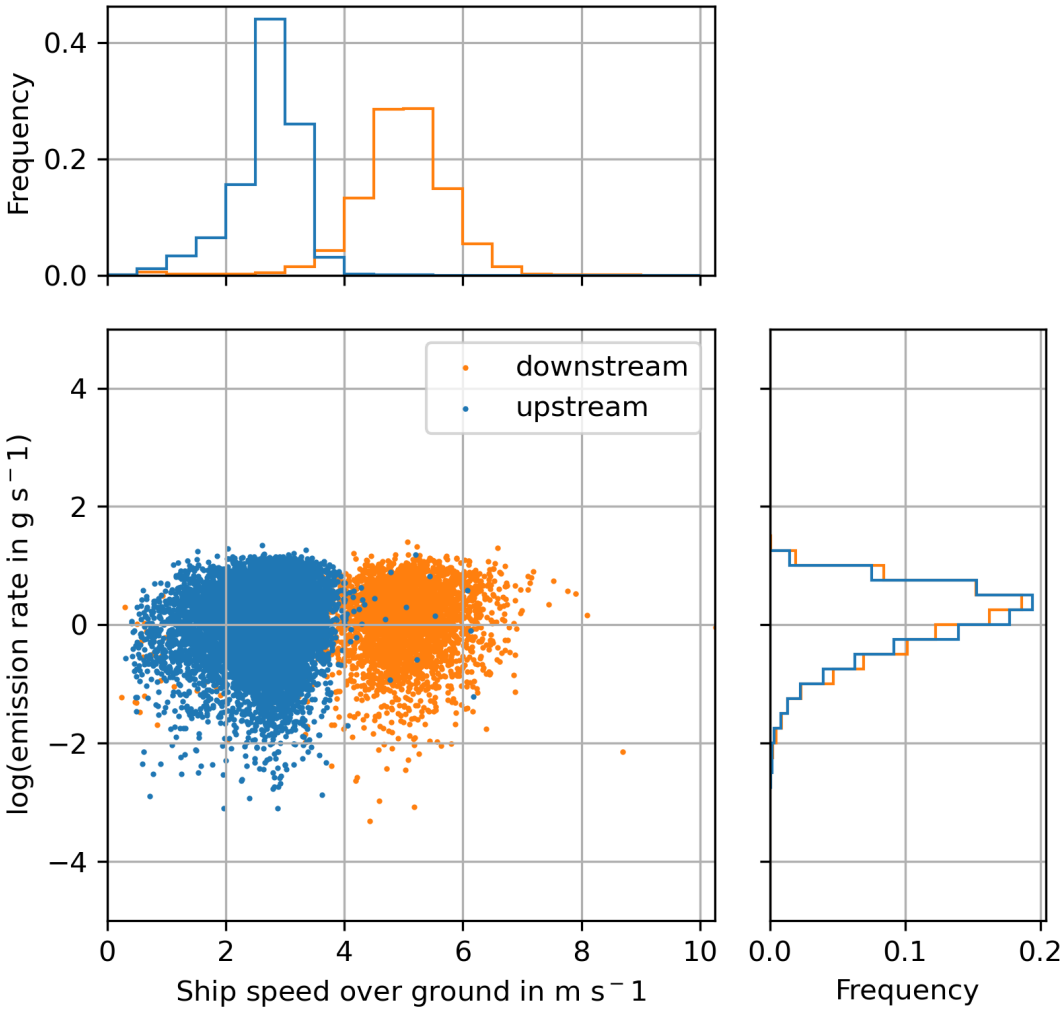

Figure 6.12: Scatter plot of log(emission rate) as a function of speed over ground.

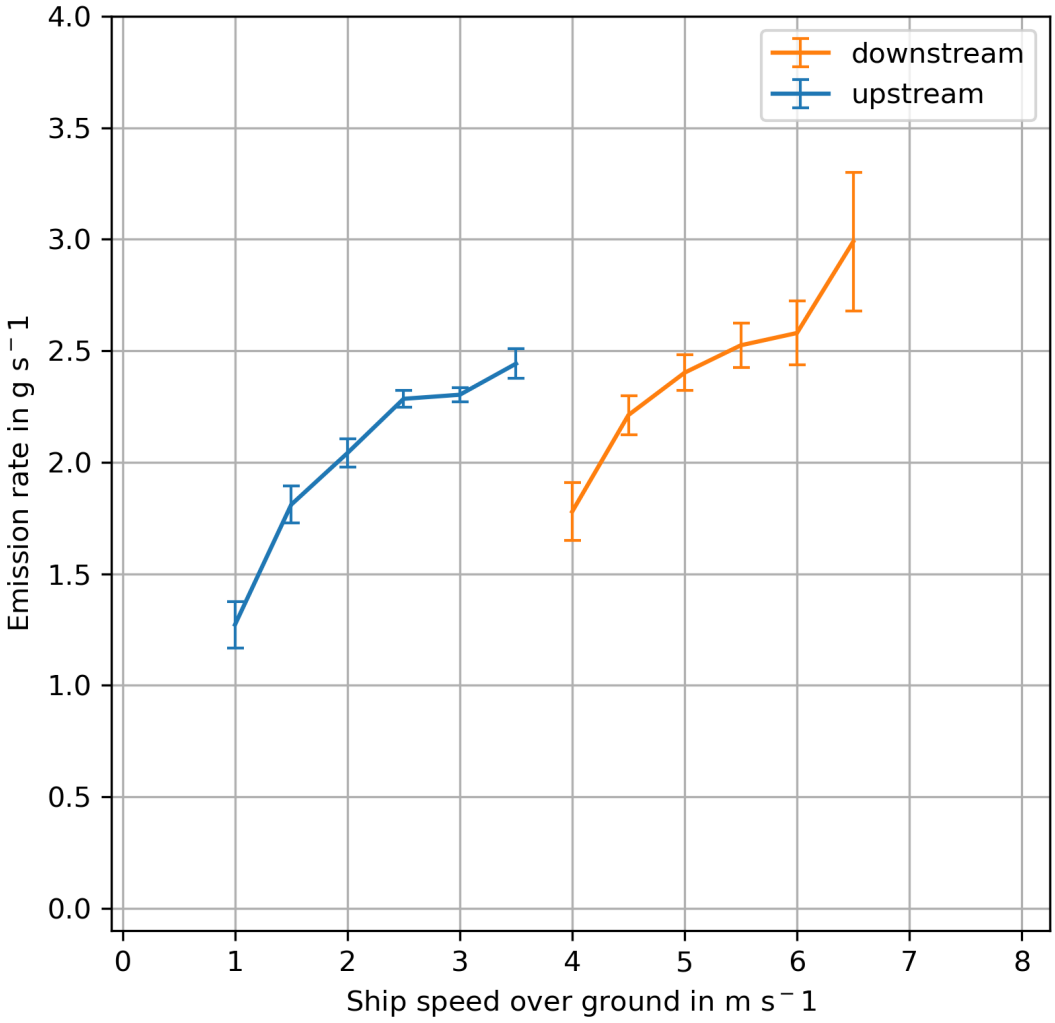

Figure 6.13: Mean emission rate as a function of ship speed over ground, binned for 0.5 $\mathrm{m\,s^{-1}}$ speed intervals. Error bars indicate standard error of the mean for each speed interval. Mean value is only shown for intervals with at least 100 individual emission rates.

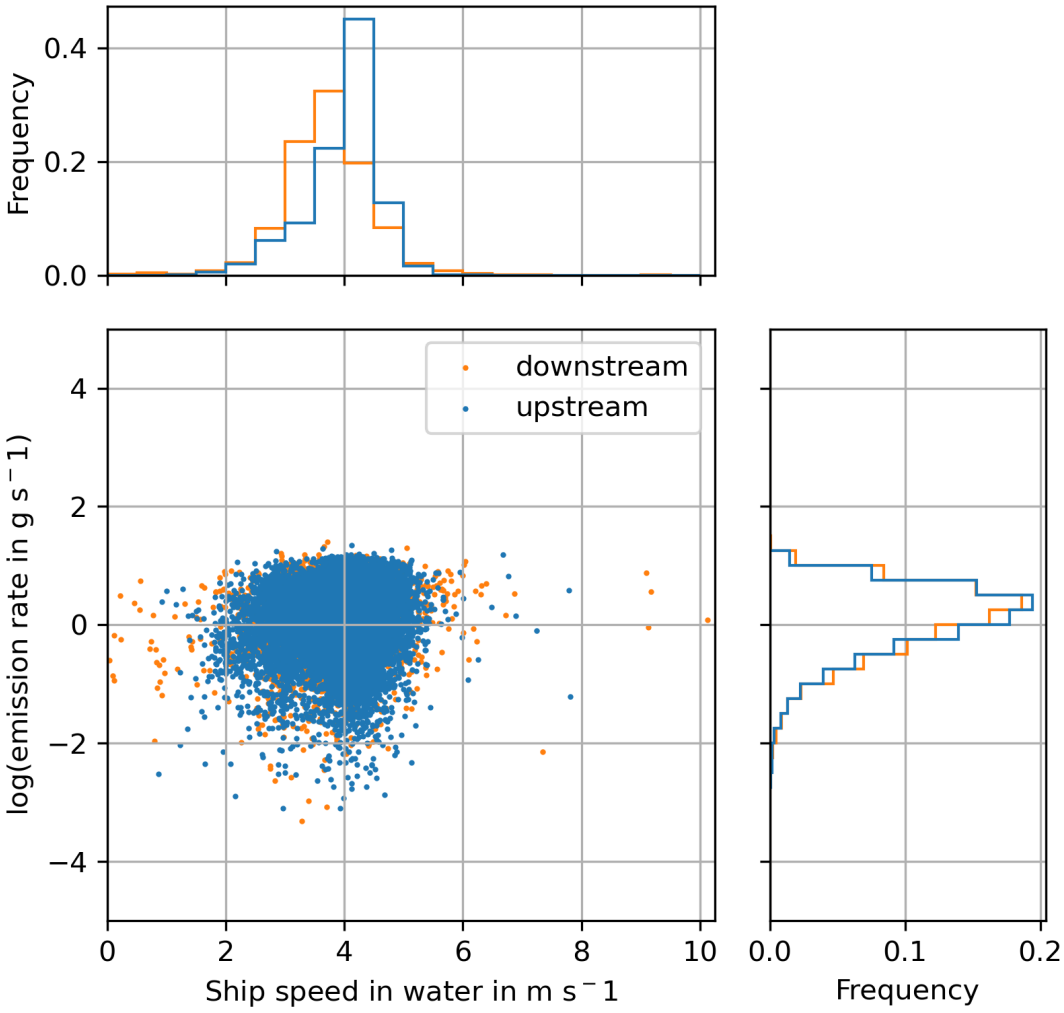

Figure 6.14: Scatter plot of log(emission rate) as a function of speed in water.

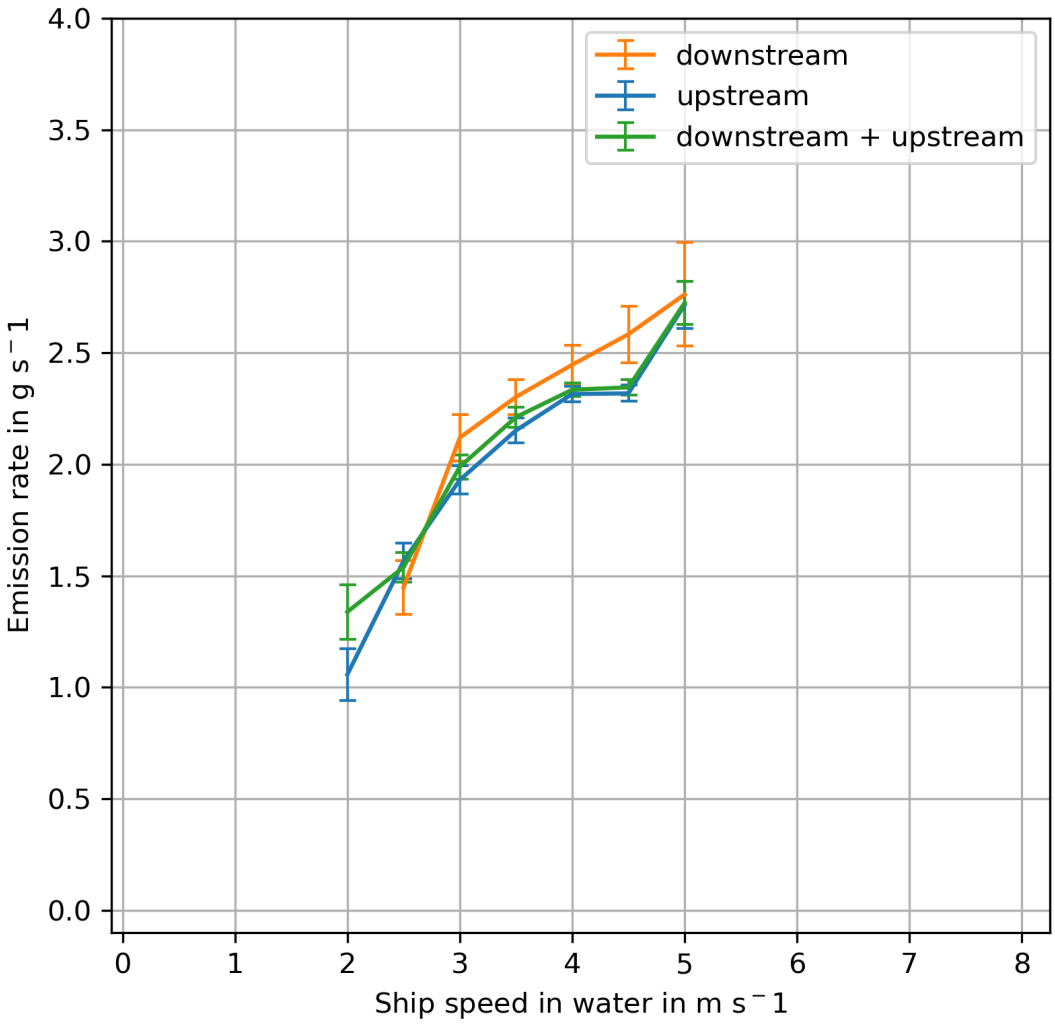

Figure 6.15: Mean emission rate as a function of ship speed in water, binned for 0.5 $\mathrm{m\,s^{-1}}$ speed intervals. Error bars indicate standard error of the mean for each speed interval. Mean value is only shown for intervals with at least 100 individual emission rates.

Table 6.4: ANOVA results for the model $log(Q_{meas}) \sim Direction + Speed\,over\,ground + Type + Direction : Speed\,over\,ground$. Here the variance in the logarithm of the emission rates is explained by the variance in direction of travel, the variance in speed over ground, the variance in ship type and the variance of the interaction between direction of travel and speed over ground.

Variable	Sum Sq	degrees of freedom	F value	Probability (> F)
Intercept	71.6	1	39.9	2.7×10^{-10}
Direction	12.5	1	6.9	0.008
Speed over ground	135.4	1	75.6	$< 2.2 \times 10^{-16}$
Type	101.2	12	4.7	1.0×10^{-7}
Direction:Speed over ground	5.0	1	2.8	0.096

Table 6.5: ANOVA results for the model $log(Q_{meas}) \sim Direction + Speed\,in\,water + Type + Direction : Speed\,in\,water$. Here the variance in the logarithm of the emission rates is explained by the variance in direction of travel, the variance in speed in water, the variance in ship type and the variance of the interaction between direction of travel and speed in water.

Variable	Sum Sq	degrees of freedom	F value	Probability (> F)
Intercept	51.8	1	28.9	7.8×10^{-8}
Direction	2.8	1	1.6	0.213
Speed in water	131.4	1	73.2	$< 2.2 \times 10^{-16}$
Type	91.1	12	4.2	1.0×10^{-6}
Direction:Speed in water	1.0	1	0.6	0.452

6.3.2 Comparison with on-board emissions measurements

In order to validate the emission rates within the CLINSH project, a comparison has been carried out between the values derived here from on-shore observations of the CLINSH fleet and the respective on-board measurements. CLINSH ships have been identified using the AIS signal as described in section 5.2.2. In case the plume observed from those ships passed the quality control, the CLINSH data base was checked for availability of on-board data for the same time. For the case of a match, on-board data have been averaged for the time period in which the plume detected by the on-shore observation system was released by the ship. Since the uncertainty of the Gaussian-puff-model is quite high, data one minute before and after the release time were taken into account as well. The 16 different CLINSH ships were observed nearly 200 times with both on-board and on-shore measurement systems. Table 6.6 and Figure 6.16 give an overview on the results.

For almost half of the ships, the agreement between on-board and on-shore observations is good and well within the error bars. However, it turns out that for some ships (e.g. ship M), on-shore values are systematically higher than the on-board data for the same time.

Table 6.6: Comparison of NO_x emission rates derived from on-shore measurements and on-board measurements for different ships participating in the CLINSH project. Number of engines only includes main engines used for navigation, and on-board measurements were only carried out on one of them. The number of engines used on ship G is not known, but assumed to be one.

Ship	class	No. of engines	on-shore mean $g\,s^{-1}$	on-shore median $g\,s^{-1}$	on-shore std $g\,s^{-1}$	on-board mean $g\,s^{-1}$	on-board std $g\,s^{-1}$	n
A	III	1	0.84	0.84	0.27	1.23	0.34	2
B	IV	1	0.94	0.40	0.92	0.81	0.32	6
C	IV	1	2.20	1.66	1.29	1.34	0.51	6
D	Va	1	2.12	1.75	0.63	0.73	0.41	3
E	Va	1	0.56	0.56	-	0.42	0.14	1
F	Va	1	2.40	1.55	2.33	2.17	0.67	45
G	Va	?	1.89	1.77	0.71	1.53	0.32	5
H	Va	1	3.65	3.85	2.44	2.47	1.23	4
I	Jowi	1	1.63	1.77	0.88	1.13	0.32	4
J	Jowi	1	2.05	0.30	3.86	0.71	0.41	13
K	Jowi	1	1.58	1.30	1.10	0.92	0.43	14
L	C-U	1	1.43	0.74	1.49	0.35	0.16	7
M* +	III	2	2.15	1.70	2.24	0.65 (1.30)	0.43 (0.86)	13
N*	Va	3	1.73	0.98	1.81	0.61 (1.83)	0.32 (0.96)	9
O*	Jowi	2	1.56	0.75	2.08	0.72 (1.44)	0.39 (0.78)	25
P*	VIb	2	1.44	0.66	1.37	0.83 (1.66)	0.42 (0.84)	17

* Ships M, N, O and P are equipped with more than one main engine used for navigation. It is assumed that the NO_x emission rates for all engines are the same. The total emission rate for all main engines is therefore assumed to be the number of engines multiplied with the measured on-board emission rates, shown in brackets.
+ Ship M is equipped with a selective catalytic reduction (SCR) system to reduce the NO_x emissions, which was not always operating.

One possible explanation is that some ships use more than one main engine for navigation, but the on-board measurement systems usually only capture the emissions of one of the engines and not the total amount emitted at the stack. The total emission rate for all main engines is assumed to be the number of engines multiplied with the measured on-board emission rates. Additionally, ship M is equipped with a SCRT (selective catalytic reduction) system to reduce the NO_x emissions, which was not always operating. Some vessels also use auxiliary engines to power generators or bow thrusters, which also add to the total emissions of the ship and can be seen by the on-shore measurements but not the on-board measurements. Taking into account all ships and all simultaneous observations, the ratio between on-shore and on-board is about 1.3 (see Figure 6.16).

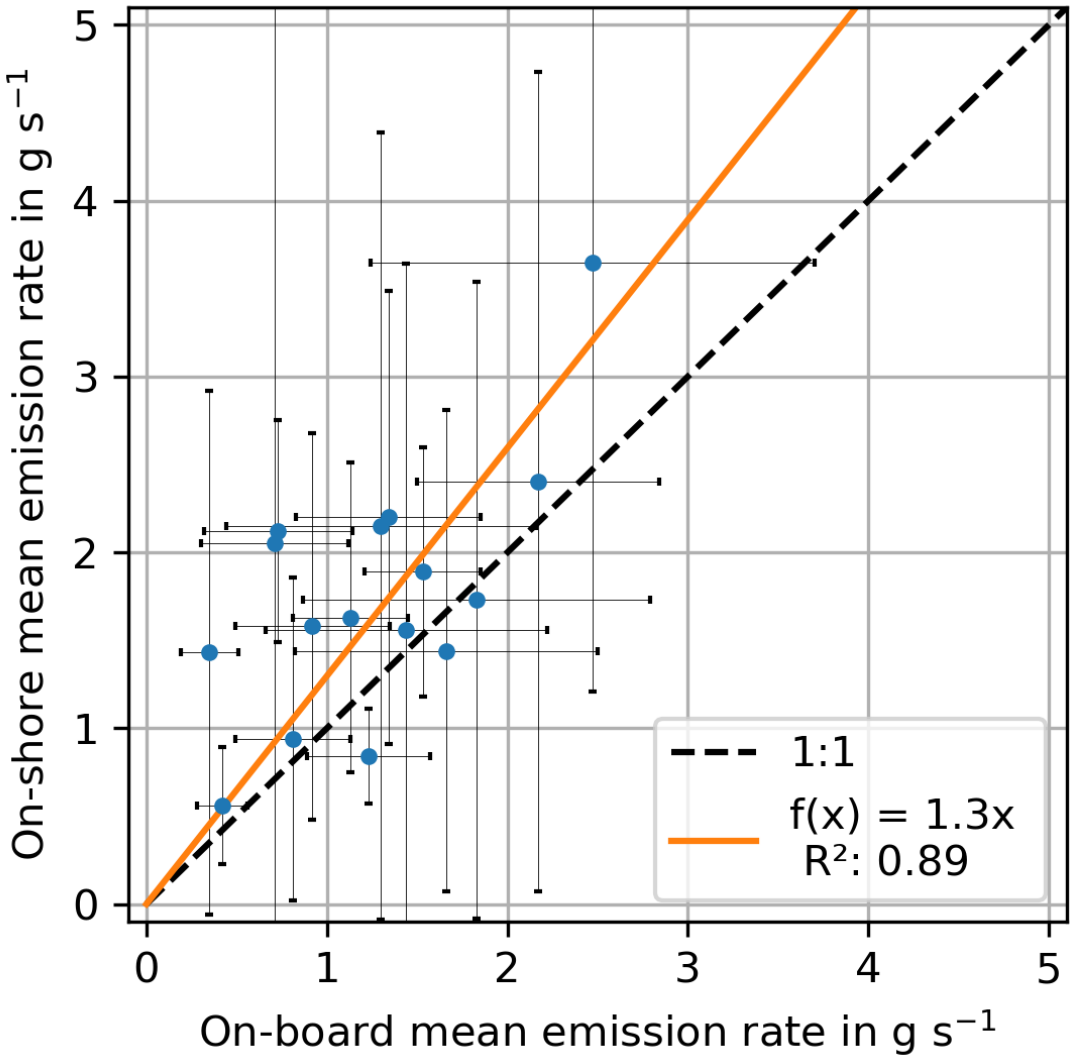

Figure 6.16: Scatter plot of on-board and on-shore emission rates. Each dot represents the mean value for one ship, errorbars indicate respective standard deviations. For ships with more than one main engine, the number of engines has been taking into account for the on-board emission rates. See also Table 6.6.

6.3.3 Comparison with other studies

The emission behaviour of vessels is usually described and evaluated by emission factors. These emission factors are relative measures, e.g. the amount of emitted NO_x is expressed per amount of burnt fuel or per amount of power generated by the engine. The absolute emission rate of NO_x has to be calculated from the emission factors and additional information about the fuel consumption. For comparison with the emission factors derived in other studies, two fuel consumption scenarios are considered. In the first scenario, a fuel consumption of 108 $kg\,h^{-1}$ is assumed, which describes the fuel consumption of a ship with 3200 tons cargo capacity travelling downstream. The second scenario uses a fuel consumption of 162 $kg\,h^{-1}$, which describes the fuel consumption of a ship with 3200 tons cargo capacity travelling upstream against the current. Both scenarios are based on the specific fuel consumptions in $kg\,km^{-1}$, which are 6 $kg\,km^{-1}$ for ships travelling downstream and 15 $kg\,km^{-1}$ for ships travelling upstream (Allekotte et al., 2020). The specific fuel consumptions have been converted to $kg\,h^{-1}$ using the average speed over ground for ships travelling upstream and downstream, which are 3 and 5 $m\,s^{-1}$, respectively.

Table 6.7 shows the comparison of literature values applied to these two scenarios with the emission rates derived in this study. The lower fuel consumption scenario shows absolute NO_x emission rates between 1.17 $g\,s^{-1}$ to 1.71 $g\,s^{-1}$. The higher fuel consumption scenario shows emission rates from 1.75 $g\,s^{-1}$ to 2.57 $g\,s^{-1}$. In comparison, the mean NO_x emission rates derived in DURH for ships that travel downstream with the most common speed of 5 $m\,s^{-1}$ are in the range of 2.36 $g\,s^{-1}$ to 2.53 $g\,s^{-1}$. For ships travelling upstream with the most common speed over ground of 3 $m\,s^{-1}$ the NO_x emission rates are 2.17 to 2.36 $g\,s^{-1}$. Generally, the mean NO_x emission rates fit into the range given by the emission factors of other studies, but are at the upper limit of the given range. At lower speeds, the mean emission rates are also lower (e.g. Figure 6.8).

Table 6.8 shows regulations that are in place for ships built or which had their engine replaced in the specified years. The regulations are defined in $g\,kWh^{-1}$ and have been converted to $g\,kg^{-1}$ using a specific fuel consumption of 230 $g\,kWh^{-1}$ (De Vlieger et al., 2004). To interpret the derived NO_x emission rates in the context of these regulations, the limits given in the regulations were converted to $g\,s^{-1}$ using the 162 $kg\,h^{-1}$ fuel consumption scenario. These values then can be interpreted as an upper limit for the NO_x emission rates for cases of high fuel consumption. Figure 6.17 shows the NO_x emission rates derived from the on-shore measurements at DURH for the most common ship classes (VI, Va, Vb and Jowi) as a function of their respective speed over ground. For all ship classes the mean NO_x emission rates for speeds higher than 2 $m\,s^{-1}$ exceed even the least strict regulation CCNR I of 9.2 $g\,kWh^{-1}$. For speeds over ground lower than 3 $m\,s^{-1}$ the mean NO_x emission rates are within the CCNR I limit, but in these cases, the assumed high fuel consumption scenario usually does not apply. When looking at the individual

Table 6.7: Comparison of the derived NO_x emission rates (ER) in $g\,s^{-1}$ with the emission factors (EF) in $kg\,h^{-1}$ derived from other studies. To calculate the emission rate from the emission factors, two fuel consumption scenarios are evaluated. Both scenarios are based on specific fuel consumption values for ships with a cargo capacity of 3200 tons (approximately class Va and Vb). First a fuel consumption of 108 $kg\,h^{-1}$ is assumed for ships that travel downstream, second a fuel consumption of 162 $kg\,h^{-1}$ is assumed for ships travelling upstream.

Study	NO_x EF in $g\,kg^{-1}$	NO_x ER in $g\,s^{-1}$	NO_x ER in $g\,s^{-1}$
Fuel consumption		108 $kg\,h^{-1}$	162 $kg\,h^{-1}$
Trozzi and Vaccaro (1998)	51	1.53	2.30
Kesgin and Vardar (2001)	57	1.71	2.57
Klimont et al. (2002)	51	1.53	2.30
Rohács and Simongáti (2007)	47	1.41	2.12
Schweighofer, J. and Blaauw, H. (2009)	39	1.17	1.75
van der Gon and Hulskotte (2010)	45	1.35	2.03
Diesch et al. (2013)	53	1.59	2.39
Knörr et al. (2013)	49	1.47	2.21
Kurtenbach et al. (2016)	54	1.62	2.43
Kattner (2019)	41	1.23	1.85
This study (DURH)		downstream	upstream
Speed over ground		5 $m\,s^{-1}$	3 $m\,s^{-1}$
IV	-	2.36 ± 0.13	2.17 ± 0.05
Va	-	2.37 ± 0.10	2.33 ± 0.04
Vb	-	2.53 ± 0.17	2.35 ± 0.07
Jowi	-	2.26 ± 0.19	2.36 ± 0.08

Table 6.8: Overview of NO_x emission limits, according to CCNR (CCNR, 2020; European Parliament and European Council, 1998) and EU regulations (European Parliament and European Council, 2016), in both cases given in units of $g\,kWh^{-1}$. For comparison these have been converted to $g\,kg^{-1}$ using a specific fuel consumption for inland ships of 230 $g\,kWh^{-1}$ (De Vlieger et al., 2004) and eventually to $g\,s^{-1}$ using the 162 $kg\,h^{-1}$ fuel consumption scenario.

Regulation	in effect since	Engine power in kW	NO_x EF in $g\,kWh^{-1}$	NO_x EF in $g\,kg^{-1}$	NO_x ER in $g\,s^{-1}$
CCNR I	2002	$P > 130$	9.2	39.9	1.80
CCNR II	2007	$P > 130$	6.0	26.1	1.17
EU RL2016/1629	2019	$130 < P < 300$	2.1	9.1	0.41
EU RL2016/1629	2019	$P > 300$	1.8	7.8	0.35

ship passages for the classes IV, Va, Vb and Jowi, approximately 50 % of the derived NO_x emission rates plus their respective uncertainty ($Q_{meas} + \sigma_Q$) are below the CCNR I upper limit, approximately 40 % are below CCNR II and 16 % are below EU RL2016/1629. These results indicate that a large number of old ships with unregulated engines are still in operation.

Kurtenbach et al. (2016) reported emission factors of 20 to 161 $g\,kg^{-1}$ with an average of 52 ± 3 $g\,kg^{-1}$, while Kattner (2019) derived a mean emission factor of 41 ± 28 $g\,kg^{-1}$. In both studies the mean emission factor is above the limits given by the regulations, but also here individual ships already comply with them.

It has to be kept in mind that the water level, hull form and propeller configuration can have a significant influence on the power required to navigate a ship, and therefore on the amount of emitted pollutants (Friedhoff et al., 2018). The mean NO_x emission rates presented here are the result of the evaluation of several years and thousands of different ships. It is therefore expected that the mean values are representative for the average ship emissions on the Rhine in Duisburg.

In addition to regulation of new ships and engines, additional technical measures, such as exhaust gas after-treatment can be used to reduce the emissions caused by ship traffic. The capabilities of exhaust gas after-treatment systems has already been shown in previous studies (e.g., Brandt and Busch, 2017; Busch et al., 2020; Kleinebrahm and Bourbon, 2013; Pirjola et al., 2014; Schweighofer, J. and Blaauw, H., 2009).

6.3.4 Ideal measurement location

The improved algorithm presented here has several advantages over the method described in Krause et al. (2021), where a Gaussian-plume-model was used to derive NO_x and SO_2 emission rates from Long-Path DOAS measurements. The measurement situation of an in-situ station is easier, as the concentration is only measured at the location of the station and does not represent the integrated column of an absorber along a light path.

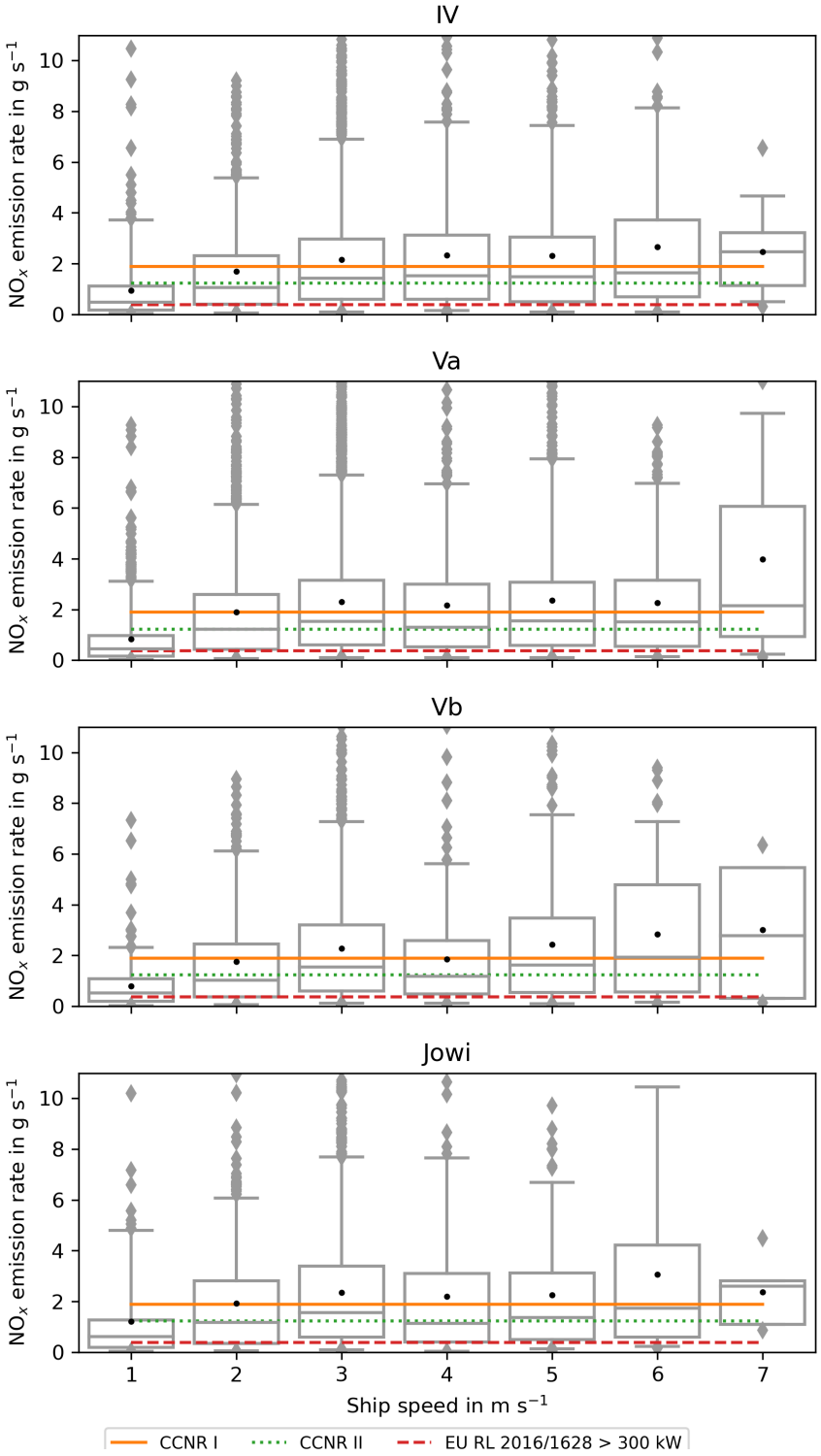

Figure 6.17: Boxplots of NO_x emission rates for ship classes IV, Va, Vb and Jowi as a function of ship speed over ground, derived from data measured at DURH. The mean value is shown as a black dot, the median value as a grey line and the whiskers indicate 5 and 95 % percentile. The limits given by the CCNR I, CCNR II and EU RL2016/1628 regulations were converted from g kWh^{-1} to g s^{-1} and are shown as coloured lines (see Table 6.8 for more details).

The equipment used in this study can be found in standardized air quality measurement stations, facilitating the use of existing stations for ship emission estimates. Only the additional AIS receiver is needed to get information about the passing vessels. This means that NO_x emission rates can be derived from existing stations with little additional costs. Also in-situ measurement stations are able to measure NO and NO_2 at the same time, so that NO_x can be measured directly and has not to be inferred from NO_2 and O_3 observations as in Krause et al. (2021).

The measurement stations in DURH and NERH were both suitable locations to derive emission rates from passing vessels under real driving conditions. However, their locations are not ideal and unnecessarily increase the difficulty when applying the algorithm to the measurement data. At the time of the installation of the measurement sites, the derivation of on-shore emission factors was not the focus of the CLINSH project. Therefore, some considerations on the position of the measurement location can improve or facilitate the derivation of the emission rates.

Ideally, a measurement station would be located at a section of a river where there are no confluences. This helps in analysing the derived emission rates, as it is easier to distinguish between ships travelling upstream and downstream. Also it removes possible special manoeuvres carried out by the ships trying to enter or leave a confluence. Also the measurement station should be located at a straight river section, preferably with the main wind direction orthogonal to the river. This decreases the chances of overlapping plumes and therefore increases the chances to identify the source ship. Locations where the wind blows along the river should be avoided, because the plumes of several ships can be mixed and the identification of the source ships can become impossible, especially when there is dense traffic. Locations with point sources of NO_x upwind the measurement site should also be avoided. These point sources could cause additional peaks, mix with the ship plumes and alter their respective peaks in the measured time series or simply lead to a highly variable background concentration which might be hard to correct. The terrain around the measurement site should be flat and even, so that the surface roughness can be characterized easily. Overall, a simple geometry of the surroundings and a low number of obstacles (i.e. trees, buildings) is beneficial for the Gaussian-puff-model. Additional usage of the measurements of the current water level would be beneficial as the uncertainty in the height of the emission could be reduced. Incoming solar radiation and cloud cover should ideally be measured at the measurement site, to be independent of other observations and to reduce the uncertainty regarding these parameters.

Generally, as has been shown in this study, these considerations are not required to derive the emission rates, but keeping at least some of them in mind can lead to overall better results or easier interpretation of those.

6.4 Application for emission inventory

As an example for an application of the derived emission rates, in this section, the total emission caused by ship traffic at specific sections of the Rhine is calculated. To quantify the total emissions caused by ship traffic in a specific area, the emission behaviour of the individual vessels as well as the traffic statistics need to be known. The emission behaviour of the individual vessels can be summarized in the form of emission factors for each class in dependence of direction of travel and speed, in this case speed over ground. The traffic statistics are derived from the AIS signals and are described briefly in the following paragraph.

The AIS station at DURH and NERH receive AIS signals within a range of several kilometres. The signal strength decreases with distance to the receivers and consequently with larger distances to the receiver, less AIS signals are received. In a radius of about 10 km around each station, every signal of every ship can be received and used for evaluation. To calculate the traffic statistics for the Rhine at different points, the river has been partitioned into segments, each representing a distance downstream from the river source. Each segment can be represented as a circle with a radius of 500 m and its center being located at the center of the river (see Figure 6.18).

For each of these segments, the number of ship passages need to be extracted. As the circles have radius of 500 m, a single passage consists of several AIS signals. To identify a single passage and distinguish it from several passages of the same ship, the time difference between the signals is used. If the differences are small, e.g. on the order of seconds to minutes, they most likely belong to the same passage, if the differences are larger, e.g. on the order of hours, they do not belong to an individual ship passage but to several different ones. For the evaluation a threshold of 60 minutes was defined, all signals which are within 60 minutes of each other are assumed to be one passage, if there is a gap of more than 60 minutes between two signals, this is treated as the start of a new individual passage. This evaluation is then done for each ship in each river segment. The individual AIS signals which comprise a single passage are then averaged to a single data point. This data includes the time stamp of the passage, the class of the ship, the mean speed over ground and direction of travel. For each ship type, the passages are divided into ships travelling upstream and ships travelling downstream and each of these directions is then further divided by speed over ground. The end result is a table of observed ship passages, where each row indicates a certain combination of ship type, direction of travel and speed over ground (e.g. seen in Table 6.11).

To verify this method the traffic derived by the described method have been compared to the traffic numbers reported by the Federal Waterways and Shipping Administration (WSV) for an AIS station located at the Dutch-German border, close to Lobith, Netherlands. The results of are shown in Table 6.10. Generally the numbers agree quite well,

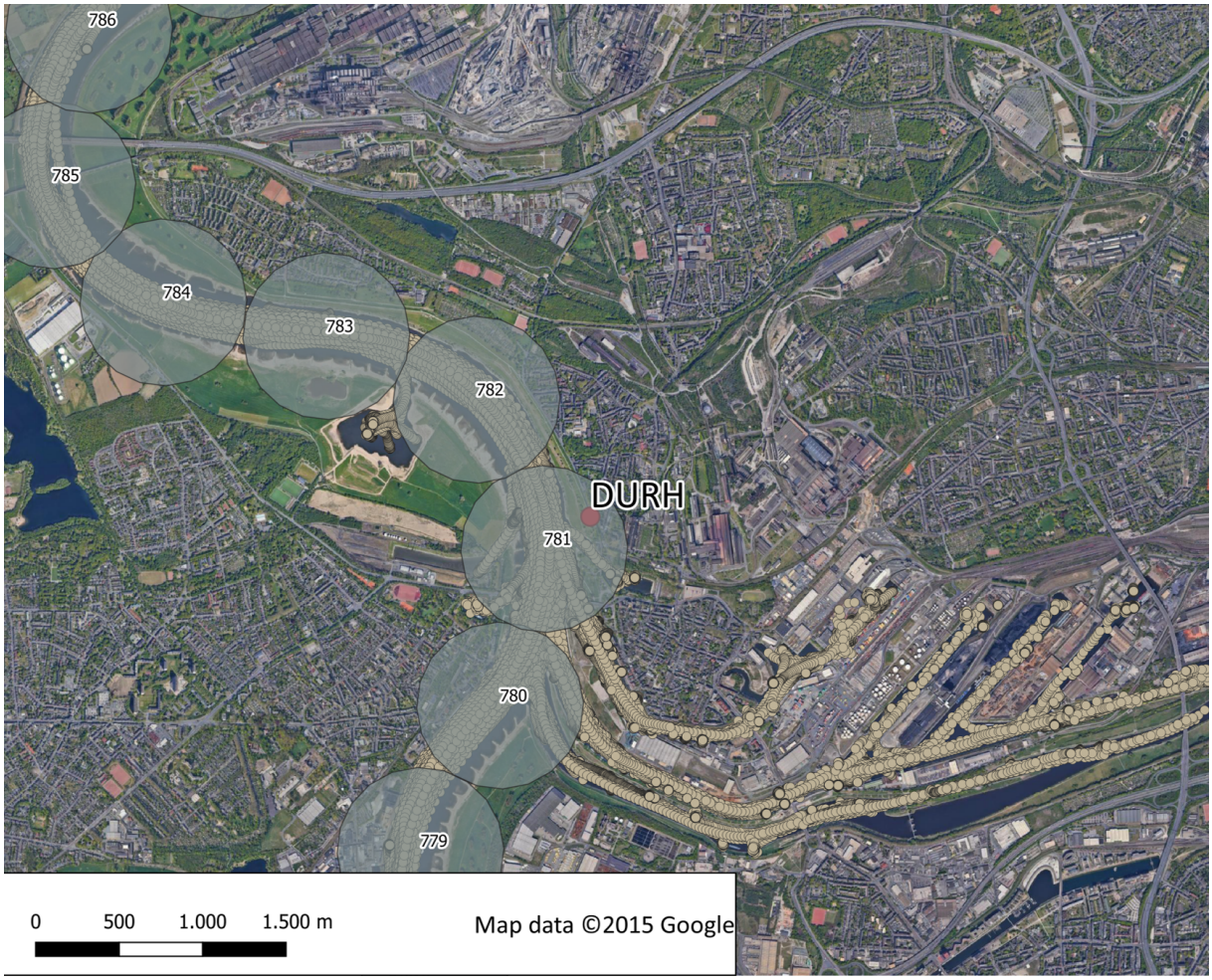

Figure 6.18: Map of the different river segments used at DURH to determine traffic statistics at DURH.

Table 6.9: Example of traffic statistics at Rhine kilometre 782.

I	II	III	IV	Va	Vb	Jowi	C-U	Vla	Vlb	Vlc	unknown	all	date
13	2	3	40	66	14	11	4	9	0	1	8	171	2017-10-23
20	4	5	64	97	29	21	8	6	3	1	20	278	2017-10-24
14	5	5	64	102	24	27	9	4	4	1	14	273	2017-10-25
21	4	11	76	109	40	19	7	9	3	0	13	312	2017-10-26
12	0	4	62	130	44	18	9	11	5	0	15	310	2017-10-27
7	2	7	54	126	32	22	8	11	3	2	15	289	2017-10-28
9	2	3	50	77	33	25	13	9	1	1	20	243	2017-10-29

Table 6.10: Comparison of traffic statistics derived by AIS signals and reported by the Federal Waterways and Shipping Administration (WSV) at the Dutch-German border at Lobith, Netherlands.

Year	derived from AIS	reported by WSV
2018	58200 (only data for the second half of 2018)	111352
2019	108800	106499
2020	109500	103624

even though the traffic derived from AIS signals overestimates the traffic by up to 5.6 %. One possible explanation for the larger amount of ship passages by the AIS method is the location of the receiver. There is a bunker station within the range of the AIS receiver and passing ships can get refuelled by resupply vessels which steam next to the passing ships for some time to refuel them. These refuelling approaches are identified as ship passages in the AIS approach, but are not ship passages reported by the WSV reports. Generally, the amount of ships decreases in upstream direction, because ships already reached their destination or change to one of the channels that connect to the Rhine. At the Dutch-German border, approximately 110.000 ship passages are registered, while in Duisburg only about 80.000 are registered.

For each ship passage the travel time through a segment needs to be calculated. Given the mean speed of a ship passage the time the ship needs pass through the river segment can be calculated. The total emission caused for a specified ship type, in a specified direction at a specified speed is then:

$$E(v,\, dir,\, shiptype) = n(v,\, dir,\, shiptype) \cdot t(v) \cdot Q(v,\, dir,\, shiptype) \tag{6.5}$$

where E is the total emitted NO_x for the observed time frame (e.g. a year), $t(v)$ is the time to travel through the given segment and $Q(v, dir)$ is the emission rate for the given speed over ground (v) in the given direction (dir). The total emission for the whole segment is then the sum of all those individual combinations of ship type, speed over ground and direction of travel:

Table 6.11: Example table to calculate the total emission caused by ship traffic at a specified segment of the Rhine.

Class	Number of observations	Direction	Speed over ground in $m\,s^{-1}$	Travel time per km in s	Emission rate in $g\,s^{-1}$	Total emission per km in kg
Va	199	upstream	2	500	1.53	152.2
Va	6006	upstream	3	333	2.29	4580.0
...	...	...	...	...	...	...
Va	2783	downstream	5	200	2.27	1263.4
...	...	...	...	...	...	...
$\sum$	N	-	-	-	-	58700

$$E_{total} = \sum_{i}^{N} E_i. \tag{6.6}$$

The combination of parameters is different for each segment, as ships do not travel at the same speed all the time, but rather adapt to the conditions. To illustrate the differences between different segments, some examples are shown in Figures 6.19, 6.20, 6.21. Each Figure shows an overview of the Rhine and histograms of ship speeds of all ship passages for a specified river segment. The histograms show, that the speed of the ships is not the same for the different segments, but depends on the local conditions. For example the segment at Rhine kilometre 740 includes the entrance to the Neuss harbour and shows a bimodal distribution of ship speed for ships travelling downstream, while this is less pronounced at e.g. Rhine kilometre 750. Also, the absolute number of ship passages differs over larger distances, as ships enter or leave harbours and side channels and change their direction of travel.

The total NO_x emissions caused by inland ship traffic for six different river segments is shown in Table 6.12. At DURH the total NO_x emissions caused by steaming ships in 2018 was 58.7 tons, while at NERH it was 48.9 tons. Generally, the total emissions decrease upstream, which can be explained by the lower number of ship passages. The calculated emissions only include emissions caused by ship passages on the Rhine itself; in harbour areas additional emissions caused by movement of the ships within the harbour and from the ships at berth is to be expected.

For comparison, the total NO_x emission of different power plants are shown in Table 6.13. Compared to the emissions of power plants, the emissions caused by ship traffic in a river segment are much lower. However, a rough calculation, assuming the emissions of Rhine kilometre 782 are representative for the whole distance from the German-Dutch border to DURH, results in a total emission of about 4755 tons of NO_x in 2018, which is in the

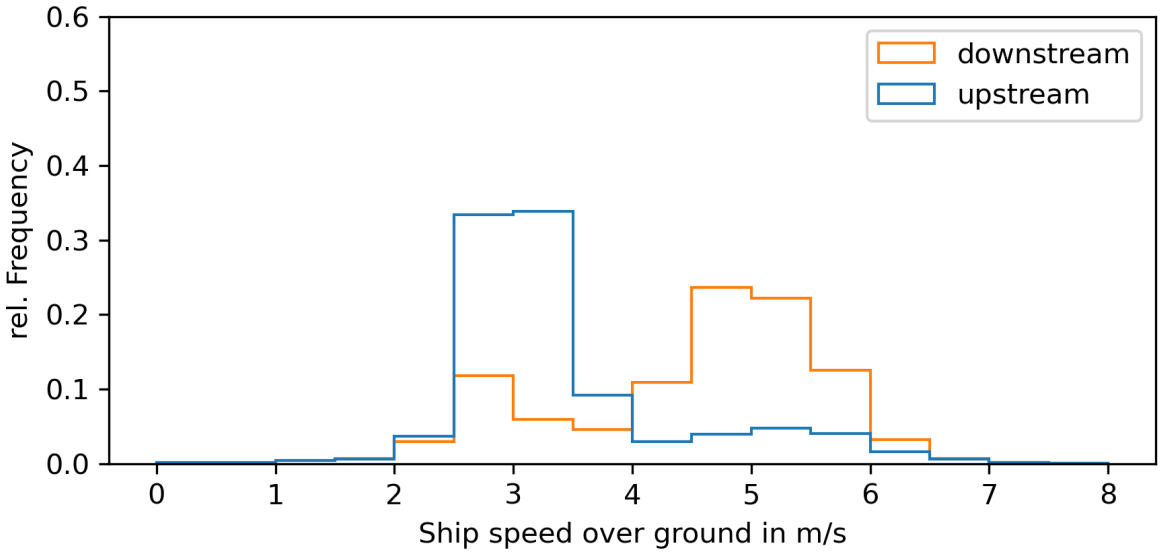

Figure 6.19: Map overview over Rhine kilometre 730 and histogram of ship speeds for ships travelling upstream and downstream.

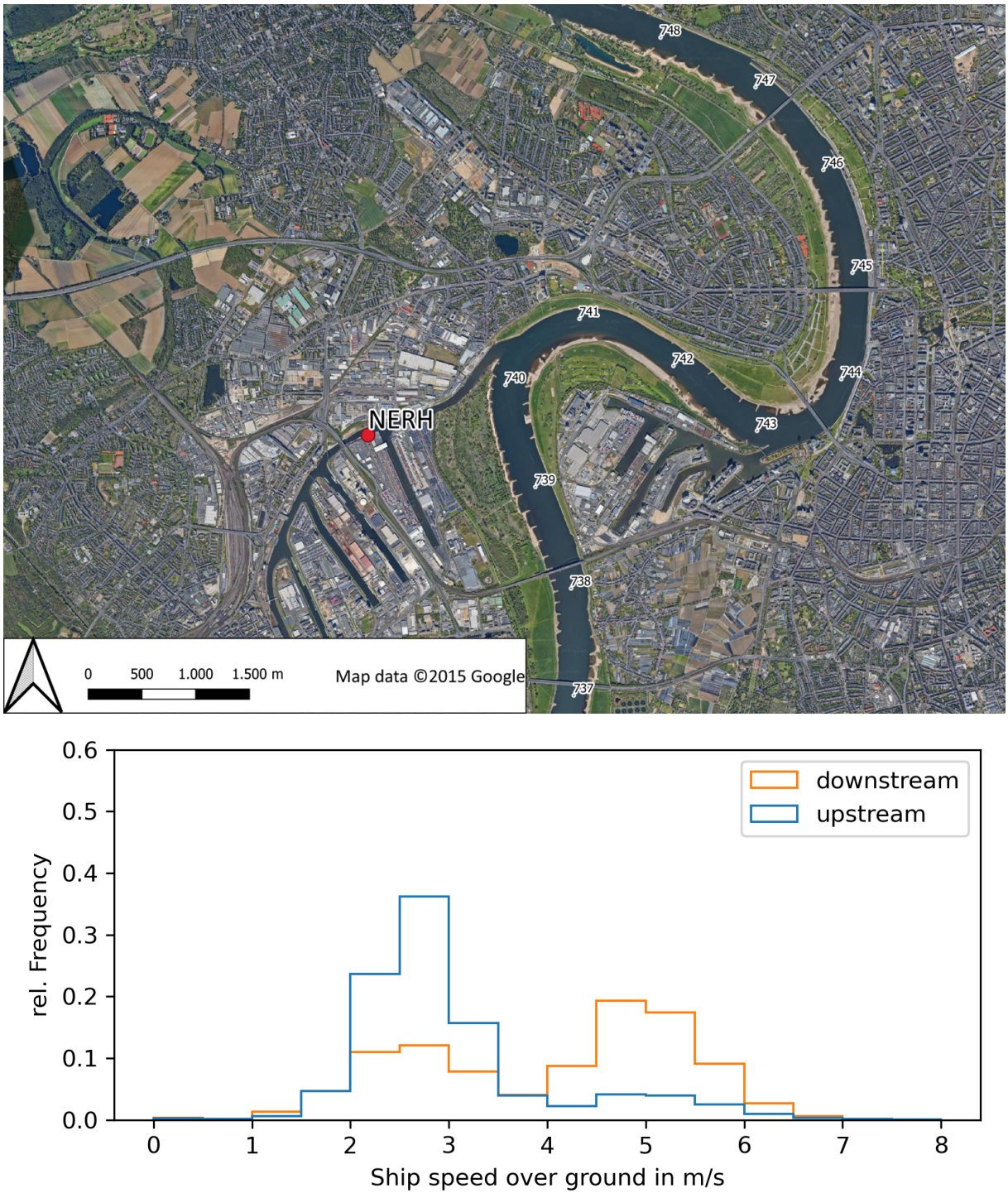

Figure 6.20: Map overview over Rhine kilometre 740 and histogram of ship speeds for ships travelling upstream and downstream.

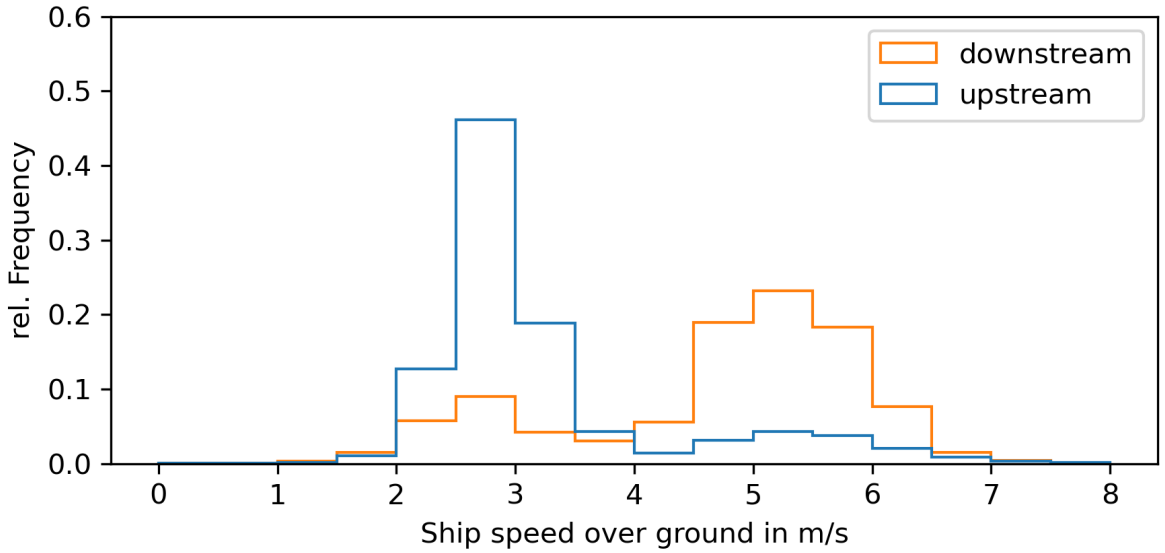

Figure 6.21: Map overview over Rhine kilometre 750 and histogram of ship speeds for ships travelling upstream and downstream.

Table 6.12: Total NO_x emissions by ship traffic in tons for 2018.

Measurement site	Rhine segment	Total NO_x emission in tons
NERH	730	36.3
NERH	742	48.9
NERH	750	47.2
DURH	772	45.5
DURH	782	58.7
DURH	791	57.7

Table 6.13: Total NO_x emissions of different power plants in 2021, retrieved from Umweltbundesamt (2022).

Source	Total NO_x emission in tons
RWE Power AG Kraftwerk Niederaußem	10200
RWE Power AG - Kraftwerk Neurath	13800
swb Erzeugung AG & Co. KG / Heizkraftwerk Hastedt	486
LEAG, Kraftwerk Jänschwalde	11600
Rhine (between German-Dutch border and DURH)	4755

same order of magnitude as the emissions of power plants. The total emissions of ship traffic for the whole Rhine in North-Rhine Westphalia should be similar to the emissions of a single coal fired power plant. However, the emissions by ship traffic on the Rhine are dispersed over a larger area.

In general, the calculation of the total emissions based on current traffic statistics and emission rates for each segment individually allows to create a realistic high resolution emission register for shipping emissions. The needed traffic statistics can be easily derived from AIS data and only a few receivers are needed to cover the whole Rhine.

6.5 In-situ measurements: Summary and conclusions

Two standardized in-situ measurement stations have been set up to measure ship emissions on the river Rhine. The first was set up on the river shore in Duisburg to measure the emissions directly at the Rhine, while the second one was installed in the harbour area of Neuss. The measurement stations were established in the period of September to October 2017. The station in Duisburg is still active while that in Neuss collected its measurements and was dismantled at the end of 2019. For both stations it was possible to identify peaks in the measured NO_x time series and find the corresponding source ships. A new method to derive absolute emission rates (in $\mathrm{g\,s^{-1}}$) from these peaks was developed and successfully applied to the data. Within the algorithm, each individual ship passage is modelled by a Gaussian-puff-model and the modelled concentration at the

measurement site is compared to the measured concentration to calculate the emission rate. The modelled concentrations are quality checked for non-physical results, which can occur when the uncertainty for the input parameters used in the Gaussian-puff-model is too high. In Duisburg, approximately 32900 peaks have been identified and could be attributed to a source ship and in approximately 23500 cases, quality controlled emission rates were derived. In Neuss, approx. 5500 peaks have been identified and approx. 3200 emission rates were derived. These emission rates were analysed in the context of ship class (size), speed over ground and direction of travel (upstream and downstream). Generally, the emission rates increase with ship size and ship speed, also the emission rates of ships travelling upstream are higher than those of ships travelling downstream with the same speed over ground. In contrast, for the same speed in water, the direction of travel has no significant influence on the emission rates. The derived emission rates in this study have been compared to emissions rates measured on-board of ships that participated in the project, and generally good agreement between both methods was found. Discrepancies can be explained by the different quantities that are measured. The on-shore measurements represent the sum of all NO_x emissions of the ship, including all auxiliary engines, while the on-board measurements are only carried out on the main engine. In case a ship uses more than one engine for navigation, the on-board measurements were only realised for one engine and not for all of them. Therefore, the number of engines had to be considered for the comparison of on-shore and on-board measurements. The emission rates have been compared to emission factors (in $\mathrm{g\,kg^{-1}}$) from other studies, under the assumption of two fuel consumption scenarios, and agree quite well considering the uncertainties.

The mean emission rates for the most common ship classes (IV, Va, Vb and Jowi) at speeds higher than 2 $\mathrm{m\,s^{-1}}$ exceed even the least strict regulations of CCNR I of 9.2 $\mathrm{g\,kWh^{-1}}$. Looking at individual ship passages for these four classes, approximately 50 % comply with CCNR I, 40 % comply with CCNR II and 16 % comply with EU RL2016/1629.

The algorithm mostly relies on input parameters that are routinely measured by standardized air quality stations. The only additional information meed is about the passing ships which can be provided by AIS receivers. In contrast to emission factors, the derived emission rates can be directly used in the conjunction with traffic statistics to model the total emissions caused by ship traffic in the area. This allows to circumvent possible uncertainties caused by assumptions made to convert relative emission factors to absolute emission rates during the modelling process. Also the emission rates include the emission of all engines on board the ships and not only of the main engine for each passing vessel.

The emission factors collected in 2017-2021 have already been applied by LANUV for the port areas of Duisburg and Neuss within the framework of CLINSH to calculate shipping-related emissions. It is planned to use this procedure for the future update of the inland waterway vessel emission register of the state of North Rhine-Westphalia for

the determination of shipping emissions. The continuously measuring station in Duisburg will remain in operation in the coming years and will be evaluated using the described algorithm. The derived emission rates can be used in conjunction with ship traffic statistics derived from AIS to calculate the total amount of NO_x emitted by inland ships at a given river segment.

7 Future developments regarding ship emissions

In the future, the total amount if ship emissions is likely to increase. The total amount of pollutants emitted by shipping is strongly correlated to the economic growth. In the past, the amount of transported goods by ship increased in correlation with the growth of the global economy. Consequently, the size of the global merchant fleet also increased and more and larger ships were built, which ultimately lead to an increase in the amount of emitted pollutants by the shipping sector. Future scenarios are uncertain, but in all cases, an economic growth is predicted (see Table 7.1). While in 2021 a strong increase in shipping activity was predicted (UNCTAD, 2022a), the prognosis of 2022 already changed to lower growth rates (UNCTAD, 2022b). In both cases the predicted increase in shipping activity is uncertain and unforeseen events such as the COVID19 pandemic or the war in Ukraine can have a large influence.

Also, the change from power generation based on fossil fuel combustion to renewable energy sources will decrease the amount of emitted air pollutants by the energy production sector. In conjunction with this, the automotive industry is forced to and tries to change its production from combustion engines towards vehicles with electric engines. For example, in the EU the "Fit for 55" package comprises revised and new laws, to reduce the GHG emissions by 55 % in 2030 and to reach carbon neutrality in 2050 (European Union, 2022). This reduction in GHG emissions also decreases the amount of other air pollutants at the same time. As energy production and traffic are two of the main sources of air pollution, a reduction of their emission intensity makes other sources of air pollution, e.g. the shipping industry, more relevant.

Generally, the shipping industry tries to reduce their emissions of GHG as well. The IMO aims to cut the GHG emissions by 40 % in 2030 and by 70 % in 2050 compared to 2008 (Aakko-Saksa et al., 2023; International Maritime Organization, 2023). Additionally, the EU proposes a maximum limit on the GHG intensity of all energy sources used on ships. Also the EU aims to reduce the GHG emissions of the maritime sector by 2 % in 2025, 20 % in 2035 and 80 % 2050 compared to 2020 levels (European Union, 2022). Additionally, the EU Commission foresees implementation of a cap-and-trade systems, which limits the GHG emissions for each ship, with a mechanism in place to trade those limits in a secondary market similar to the emissions trading already in place.

Table 7.1: International maritime trade forecasts. Numbers in brackets were reported by UNCTAD (2022a) while the other numbers were reported in UNCTAD (2022b).

Year	Annual Growth containerized trade volume in %	Annual Growth total seaborne trade volume in %
2022	(5.9) 1.2	(3.2) 1.4
2023	(4.7) 1.9	(2.4) 1.4
2024	(4.4) 3.0	(2.3) 2.2
2025	(4.2) 3.1	(2.3) 2.3
2026	(4.1) 2.9	(2.2) 2.3
2027	3.8	2.2

The reduction in GHG emissions can be achieved in various ways and also indirectly influences the emissions of NO_x, SO_x or PM. Fuel type, engine load and engine size affect emissions from ships. In order to reduce GHG emissions, ships can travel at lower speeds which leads to lower engine loads and lower fuel consumption. However, engines are designed to operate at high engine loads and adjustments of the engine parameters come at the cost of the fuel economy and increased black carbon (BC) emissions (Aakko-Saksa et al., 2023). There will always be a trade-off between NO_x and BC emissions and fuel economy. Even though this load dependency is more pronounced in older ship engines, it still is a relevant problem, because of the long service life of ships. Non-optimised use of engines is anticipated to reduce along with the energy efficiency targets. Kites and rotors can further reduce the energy consumption of a ship and are especially effective at lower speeds (Aakko-Saksa et al., 2023). Exhaust gas after treatment systems which reduce emissions of NO_x or SO_2 increase the fuel consumption, typically by about 10 %, consequently additional solutions are needed to reduce GHG and pollutant emissions at the same time (Aakko-Saksa et al., 2023).

The impact of ship emissions on global warming is likely to increase in the future. The decrease in fuel sulphur content reduces the amount of emitted SO_2 and consequently the amount of sulphate particles which reflect sunlight (Aakko-Saksa et al., 2023). Alternative fuels might increase the overall GHG emissions, e.g. by increased emissions of methane by incomplete combustion or leakages when LNG is used as fuel. NH_3 can be used as shipping fuel as well but as it is produced by the Haber-Bosch process, the amount of emissions depends on the electricity used during this process. Using electricity from renewable energy sources would make it possible to have almost no GHG and sulphur emissions. The same is true for ship using electric propulsion systems, which currently mostly are used for short distances. In the future, electric propulsion systems powered by electricity from renewable energy sources might enable ship transport with close to zero emissions. Also biofuels from sustainable agriculture can be promising to get sulphur free and carbon neutral fuels in the future.

Currently no readily available fuel option delivers significant savings on pollutants and GHG emissions at the same time (Gilbert et al., 2018). In most cases, stricter NO_x and SO_x regulations also reduce CO_2 emissions (Bouman et al., 2017), but there are studies which report an increase in CO_2 equivalent emissions when stricter NO_x and SO_2 regulations are applied (Eide et al., 2013; Lindstad et al., 2016; Ma et al., 2012). For GHG emissions, it is important to consider emissions of the full life-cycle of the fuel, from production, transport to combustion to evaluate the performance of alternative fuels (Aakko-Saksa et al., 2023; Gilbert et al., 2018). In general, retrofitable solutions to reduce GHG and pollutant emissions are preferable, as they would enable fast implementation of new legislation and maximize the impact of future regulations. Hydrogen and ammonia can be mixed with conventional marine fuels and speed up the transformation of the shipping industry towards lower or near zero emissions. Technology from the car and truck sector might also be usable for ships and enable a faster reduction of ship emissions, e.g. a mix of hydrogen and methane (hythane) can be used as fuel for combustion engine and is a proven technology in the automotive sector (Aakko-Saksa et al., 2023).

8 Conclusions

In this thesis, the air pollution caused by ships was analysed using different measurement techniques at different measurement sites. To show the capabilities of LP-DOAS instruments to monitor ship emissions, two such instruments were set up in Wedel, a small town at the river Elbe about 10 km seawards of the Hamburg harbour. The LP-DOAS instruments were able to measure SO_2 and NO_2 emitted by the ships. One of the instruments was a new prototype ,specifically designed by Airyx GmbH to measure ship emissions, while the other one was a well characterized scientific instrument of the IUP Heidelberg. The new prototype instrument proved to be capable of gathering data with a similar quality as the scientific instrument.

As a demonstration of the capabilities of LP-DOAS in monitoring ship emissions, a new method to derive emission rates of NO_2, NO_x and SO_2 from LP-DOAS measurements has been successfully developed and presented. Between April 2018 and May 2019, 7402 ship passages have been identified and assigned to peaks in the SO_2 and / or NO_2 time series, measured by the scientific IUP Heidelberg LP-DOAS. For these ship passages, the individual emissions rates of NO_2, NO_x and SO_2 have been derived. A Gaussian plume model is applied to simulate the plumes of passing ships. The simulated plumes are then used to derive a concentration the LP-DOAS instruments would have measured given the assumptions in the model. The modelled concentration is compared to the measured concentration enhancement to calculate the emission rate. After filtering, a total of 886 NO_x, 1069 SO_2 and 1375 NO_2 emission rates were derived. Filtering was needed to remove non-physical results, which occur when the assumptions of the model do not reflect the real measurement situation. The emission rates increase as a function of ship size and as a function of speed over ground. Several ships passed the measurement site multiple times and showed a low variability in their emission rates. The derived emission rates can potentially be used as input for the assessment of the influence of ship emissions on regions close to shipping lanes.

The method to derive emission rates from trace gas time series was improved over time. Four years of measurements of in-situ measurement stations located at the Rhine in North-Rhine Westphalia have been successfully analysed using the improved method. The first measurement station was set up close to the Duisburg Rhine Harbour and is still active. The second measurement station was set up within the Neuss Rhine Harbour and has been dismantled at the end of 2019. The data of both stations showed large NO_x peaks

and it was possible to identify the corresponding source ships of these NO_x enhancements. In Duisburg, about 32900 peaks have been identified and could be attributed to the respective source ships. In approximately 23500 cases, quality controlled emission rates were derived using the improved algorithm. In Neuss, approx. 5500 peaks have been identified and 3200 quality controlled emission rates were derived. The emission rates were summarized in the context of the ship class (size), ship speed in water as well as ship speed over ground and direction of travel. The emission rates generally increase as a function of speed. However, there are differences when looking at speed over ground and speed in water. While for speed over ground, the direction of travel has to be considered in the analysis as well, it can be neglected when looking at the speed in water. Ships with the same speed in water show similar emission rates independent of their direction of travel. The emission rates derived by the presented method were also compared to emission rates measured directly on-board of ships that participated in the CLINSH project. Generally, a good agreement between both methods was found. Discrepancies can be explained by the different quantities that are measured. While the on-shore in-situ instruments measure the sum of all NO_x emissions of the ship, including all auxiliary engines, the on-board measurements were only carried out on the main engine. The emission rates derived from the on-shore measurements have been compared to emission factors (in $\mathrm{g\,kg^{-1}}$) from other studies under the assumption of two fuel consumption scenarios, and agree well considering the uncertainties. Evaluation of the emission rates in context of existing NO_x regulations showed, that at speeds over ground higher than 2 $\mathrm{m\,s^{-1}}$ even the least strict NO_x regulations are often exceeded. For the most common ship classes, approximately 50 % comply with CCNR I, 40 % comply with CCNR II and 16 % comply with EU RL2016/1629. New regulations are not enforced for existing ships, currently only regulations that were in place when the ship was built need to be complied with. An exception is the installation of a new engine, in which case the new regulations also apply. The findings in this study suggest, that the current fleet of inland ships on the Rhine at Duisburg is quite old and does not need to comply with new regulations. The full effect of the current regulations has therefore not yet been achieved.

Additionally, a way to compute traffic statistics out of AIS signals from AIS receivers along the Rhine was successfully developed. The evaluation showed that there are about 80000 ship passages in Duisburg each year. In conjunction with the derived emission rates it was possible to calculate the absolute NO_x emissions of ships for each year segment wise for each kilometre of the river Rhine. A rough calculation of the total NO_x emissions of ship traffic from the Dutch-German border to Duisburg showed, that they are on the same order of magnitude as the total NO_x emissions of one large brown coal power plant in North-Rhine Westphalia. With the change to renewable energy sources, the relevance of power plants in the context of air pollution declines, while the relative contribution of ship emissions to the total anthropogenic emissions is likely to increase. Consequently,

ships emissions need to be monitored in the future to evaluate their impact on air quality.

Outlook

The measurement of ship emissions and the derivation of emission rates can be improved in several ways. Better knowledge of key parameters will reduce the uncertainty of the derived emission rates. Better knowledge of the exact position of the emission location i.e. the position of the ship's funnel and it's height would improve the quality of the calculated emission rates. More sophisticated models to describe the plume shape and dispersion would be of value.

For the LP-DOAS measurements, a shorter light path across the river would enhance the possibility to detect emissions from smaller vessels. The measurement of the CO_2 concentration along the light path would supersede the need for a dispersion model. Measurements of CO_2 using an LP-DOAS style techniques, would enable deriving emission factors additionally to emission rates. These emission factors would be comparable to emission factors derived from in-situ measurement, but keep the advantages of the LP-DOAS instruments. In contrast to in-situ instruments, the LP-DOAS does not need to be calibrated and is able to measure independent of wind conditions, i.e. it does not rely on the wind to transport pollutants to the measurement site. Consequently, it would be possible to measure emissions from almost every ship passing a measurement site.

For emission registers, it would be beneficial to use emission rates or emission factors derived in the area they should represent. Based on the analysis of the AIS signals gathered along the Rhine, ships tend to adjust their speed to local conditions. These adjustments can take place at short spatial intervals. Consequently, to calculate the total emissions of inland ships, traffic statistics should be gathered with a high spatial resolution, to capture the variability of the ship speed and fleet composition correctly. Together with spatially high-resolution traffic data, emission rates can be used to create a high-resolution ship emissions register., which would be a major improvement to current approaches.

Bibliography

Päivi T. Aakko-Saksa, Kati Lehtoranta, Niina Kuittinen, Anssi Järvinen, Jukka-Pekka Jalkanen, Kent Johnson, Heejung Jung, Leonidas Ntziachristos, Stéphanie Gagné, Chiori Takahashi, Panu Karjalainen, Topi Rönkkö, and Hilkka Timonen. Reduction in greenhouse gas and other emissions from ship engines: Current trends and future options. *Progress in Energy and Combustion Science*, 94:101055, 2023. ISSN 03601285. doi: 10.1016/j.pecs.2022.101055.

B. Alföldy, J. B. Lööv, F. Lagler, J. Mellqvist, N. Berg, J. Beecken, H. Weststrate, J. Duyzer, L. Bencs, B. Horemans, F. Cavalli, J.-P. Putaud, G. Janssens-Maenhout, A. P. Csordás, R. van Grieken, A. Borowiak, and J. Hjorth. Measurements of air pollution emission factors for marine transportation in SECA. *Atmospheric Measurement Techniques*, 6(7):1777–1791, 2013. doi: 10.5194/amt-6-1777-2013.

Michel Allekotte, Kirsten Biemann, Christoph Heidt, Marie Colson, and Wolfram Knörr. Aktualisierung der Modelle TREMOD/TREMOD-MM für die Emissionsberichterstattung 2020 (Berichtsperiode 1990-2018), 2020.

Virginie Attivissimo, Christiane Gengler, Mario Colantonio, Manuel Da Silva, Daniel Ganea, Julien Tardivon, and Knut Utvik. *Energy, transport and environment statistics: 2020 edition*, volume 2020 of *Statistical books*. Publications Office of the European Union, Luxembourg, 2020 edition edition, 2020. ISBN 978-92-76-20736-8.

J. Beecken, J. Mellqvist, K. Salo, J. Ekholm, and J.-P. Jalkanen. Airborne emission measurements of SO_2, NO_2 and particles from individual ships using a sniffer technique. *Atmospheric Measurement Techniques*, 7(7):1957–1968, 2014. doi: 10.5194/amt-7-1957-2014.

J. Beecken, J. Mellqvist, K. Salo, J. Ekholm, J.-P. Jalkanen, L. Johansson, V. Litvinenko, K. Volodin, and D. A. Frank-Kamenetsky. Emission factors of SO_2, NO_2 and particles from ships in Neva Bay from ground-based and helicopter-borne measurements and AIS-based modeling. *Atmospheric Chemistry and Physics*, 15(9):5229–5241, 2015. doi: 10.5194/acp-15-5229-2015.

S. Beirle. Estimate of nitrogen oxide emissions from shipping by satellite remote sensing.

Geophysical Research Letters, 31(18), 2004. ISSN 00948276. doi: 10.1029/2004GL020312.

N. Berg, J. Mellqvist, J.-P. Jalkanen, and J. Balzani. Ship emissions of SO_2 and NO_2: DOAS measurements from airborne platforms. *Atmospheric Measurement Techniques*, 5(5):1085–1098, 2012. doi: 10.5194/amt-5-1085-2012.

K. Folkert Boersma, Geert C. M. Vinken, and Jean Tournadre. Ships going slow in reducing their nox emissions: changes in 2005–2012 ship exhaust inferred from satellite measurements over europe. *Environmental Research Letters*, 10(7):074007, 2015. doi: 10.1088/1748-9326/10/7/074007.

Evert A. Bouman, Elizabeth Lindstad, Agathe I. Rialland, and Anders H. Strømman. State-of-the-art technologies, measures, and potential for reducing ghg emissions from shipping – a review. *Transportation Research Part D: Transport and Environment*, 52: 408–421, 2017. ISSN 13619209. doi: 10.1016/j.trd.2017.03.022.

Andreas Brandt and Dieter Busch. *Emissionen des Containerschiffs MS Aarburg: Auswirkungen der Nachrüstung mit einer Diesel-Wasser-Emulsionsanlage*, volume 77 of *LANUV-Fachbericht*. Landesamt für Natur, Umwelt und Verbraucherschutz Nordrhein-Westfalen (LANUV), Recklinghausen, 2017.

Guy Brasseur and Susan Solomon. *Aeronomy of the middle atmosphere: Chemistry and physics of the stratosphere and mesosphere*, volume 32 of *Atmospheric and oceanographic sciences library*. Springer, Dordrecht, 3., rev. and enlarged ed. edition, 2005. ISBN 1-4020-3284-6. URL http://www.loc.gov/catdir/enhancements/fy0823/2007468800-d.html.

G. A. Briggs. Diffusion estimation for small emissions. Preliminary report, 1973. URL https://www.osti.gov/biblio/5118833.

Dieter Busch, Andreas Brandt, Martin Kleinebrahm, and Sergej Dreger. *Emissionsmessungen auf dem Laborschiff Max Prüss nach Ausrüstung mit einem SCRT-System: Ein Beitrag zum Projekt Clean Inland Shipping (CLINSH)*, volume 102 of *LANUV-Fachbericht*. Landesamt für Natur Umwelt und Verbraucherschutz Nordrhein-Westfalen (LANUV), Recklinghausen, 2020. URL https://edocs.tib.eu/files/e01fn21/1745705619.pdf.

CCNR. Rheinschiffsuntersuchungsordnung (RheinSchUO), 2020. URL https://www.ccr-zkr.org/files/documents/reglementRV/rv1de_012022.pdf.

L. Clapp. Analysis of the relationship between ambient levels of O_3, NO_2 and NO as a function of NO_x in the UK. *Atmospheric Environment*, 35(36):6391–6405, 2001. ISSN 13522310. doi: 10.1016/S1352-2310(01)00378-8.

D.A Cooper. Exhaust emissions from high speed passenger ferries. *Atmospheric Environment*, 35(24):4189–4200, 2001. ISSN 13522310. doi: 10.1016/S1352-2310(01)00192-3.

James J. Corbett, Paul S. Fischbeck, and Spyros N. Pandis. Global nitrogen and sulfur inventories for oceangoing ships. *Journal of Geophysical Research*, 104(D3):3457–3470, 1999. ISSN 0148-0227. doi: 10.1029/1998JD100040.

I. De Vlieger, L. Int Panis, H. Joul, and E Cornelis. Fuel consumption and CO_2-rates for inland vessels. *Urban Transport X*, 75, 2004. doi: 10.2495/UT040621.

J.-M. Diesch, F. Drewnick, T. Klimach, and S. Borrmann. Investigation of gaseous and particulate emissions from various marine vessel types measured on the banks of the Elbe in Northern Germany. *Atmospheric Chemistry and Physics*, 13(7):3603–3618, 2013. doi: 10.5194/acp-13-3603-2013.

DWD Climate Data Center. Historical 10-minute station observations of solar incoming radiation,longwave downward radiation and sunshine duration for Germany, version V1, 2022a.

DWD Climate Data Center. Selected 81 stations, distributed over Germany, in the traditional KL-standard format, version recent, 2022b.

M. S. Eide, S. B. Dalsøren, Ø. Endresen, B. Samset, G. Myhre, J. Fuglestvedt, and T. Berntsen. Reducing co_2 from shipping – do non-co_2 effects matter? *Atmospheric Chemistry and Physics*, 13(8):4183–4201, 2013. doi: 10.5194/acp-13-4183-2013.

European Commission, Eurostat (ESTAT), GISCO. Countries, 2020 - administrative units - dataset, 2020. URL https://ec.europa.eu/eurostat/web/gisco/geodata/reference-data/administrative-units-statistical-units/countries.

European Conference of Ministers of Transport. RESOLUTION No. 92/2 ON NEW CLASSIFICATION OF INLAND WATERWAYS, 1992. URL https://www.itf-oecd.org/sites/default/files/docs/wat19922e.pdf.

European Parliament and European Council. DIRECTIVE 97/68/EC OF THE EUROPEAN PARLIAMENT AND OF THE COUNCIL of 16 December 1997 on the approximation of the laws of the Member States relating to measures against the emission of gaseous and particulate pollutants from internal combustion engines to bin installed in non-road mobile machinery. *OJ*, L 059:p. 1, 1998. URL https://eur-lex.europa.eu/legal-content/EN/TXT/PDF/?uri=CELEX:01997L0068-20161006&from=EN.

European Parliament and European Council. Regulation (EU) 2015/757 of the European Parliament and of the Council of 29 April 2015 on the monitoring, reporting

and verification of carbon dioxide emissions from maritime transport, and amending Directive 2009/16/EC (Text with EEA relevance). *OJ*, L 123:p. 55, 2015. URL https://eur-lex.europa.eu/eli/reg/2015/757/oj.

European Parliament and European Council. REGULATION (EU) 2016/1628 OF THE EUROPEAN PARLIAMENT AND OF THE COUNCIL of 14 September 2016 on requirements relating to gaseous and particulate pollutant emission limits and type-approval for internal combustion engines for non-road mobile machinery, amending Regulations (EU) No 1024/2012 and (EU) no 167/2013, and amending and repealing Directive 97/68/EC. *OJ*, L 252:p. 53, 2016. URL https://eur-lex.europa.eu/legal-content/EN/TXT/?uri=CELEX:02016R1628-20210630.

European Union. Reducing carbon emissions: Eu targets and measures, 2022. URL https://www.europarl.europa.eu/news/en/headlines/society/20180305STO99003/reducing-carbon-emissions-eu-targets-and-measures.

V. Eyring, H. W. Köhler, A. Lauer, and B. Lemper. Emissions from international shipping: 2. impact of future technologies on scenarios until 2050. *Journal of Geophysical Research*, 110(D17), 2005a. ISSN 0148-0227. doi: 10.1029/2004JD005620.

V. Eyring, H. W. Köhler, J van Aardenne, and A. Lauer. Emissions from international shipping: 1. the last 50 years. *Journal of Geophysical Research*, 110(D17), 2005b. ISSN 0148-0227. doi: 10.1029/2004JD005619.

Veronika Eyring, Ivar S.A. Isaksen, Terje Berntsen, William J. Collins, James J. Corbett, Oyvind Endresen, Roy G. Grainger, Jana Moldanova, Hans Schlager, and David S. Stevenson. Transport impacts on atmosphere and climate: Shipping. *Atmospheric Environment*, 44(37):4735–4771, 2010. ISSN 13522310. doi: 10.1016/j.atmosenv.2009.04.059.

J. Faber, S. Hanayama, S. Zhang, P. Pereda, B. Comer, E. Hauerhof, W. Schim van der Loeff, T. Smith, Y. Zhang, H. Kosaka, M. Adachi, J.-M. Bonello, C. Galbraith, Z. Gong, K. Hirata, D. Hummels, A. Kleijn, D. S. Lee, Y. Liu, A. Lucchesi, X. Mao, E. Muraoka, L. Osipova, H. Qian, D. Rutherford, S. Suárez de la Fuente, H. Yuan, C. V. Perico, L. Wu, D.-H. Y. Deping Sun, and H. Xing. *Fourth IMO GHG study 2020: Full report*. International Maritime Organization, London, 2021.

Junlan Feng, Yan Zhang, Shanshan Li, Jingbo Mao, Allison P. Patton, Yuyan Zhou, Weichun Ma, Cong Liu, Haidong Kan, Cheng Huang, Jingyu An, Li Li, Yin Shen, Qingyan Fu, Xinning Wang, Juan Liu, Shuxiao Wang, Dian Ding, Jie Cheng, Wangqi Ge, Hong Zhu, and Katherine Walker. The influence of spatiality on shipping emissions, air quality and potential human exposure in the yangtze river delta/shanghai, china.

Atmospheric Chemistry and Physics, 19(9):6167–6183, 2019. doi: 10.5194/acp-19-6167-2019.

B. Friedhoff, S. List, K. Hoyer, and M. Tenzer. Bestimmung des effektiven Propellerzustroms, 2018. URL https://www.bmvi.de/SharedDocs/DE/Anlage/G/bestimmung-effektiver-propellerzustrom.pdf?__blob=publicationFile.

Aristeidis K. Georgoulias, K. Folkert Boersma, Jasper van Vliet, Xiumei Zhang, Ronald van der A, Prodromos Zanis, and Jos de Laat. Detection of no 2 pollution plumes from individual ships with the tropomi/s5p satellite sensor. *Environmental Research Letters*, 15(12):124037, 2020. doi: 10.1088/1748-9326/abc445.

Paul Gilbert, Conor Walsh, Michael Traut, Uchenna Kesieme, Kayvan Pazouki, and Alan Murphy. Assessment of full life-cycle air emissions of alternative shipping fuels. *Journal of Cleaner Production*, 172:855–866, 2018. ISSN 09596526. doi: 10.1016/j.jclepro.2017.10.165.

Steven R. Hanna, Gary A. Briggs, and Rayford R. Hosker. Handbook on atmospheric diffusion, 1982.

International Maritime Organization. *Protocol of 1997 to amend MARPOL 73/78: Annex VI of MARPOL 73/78 Regulations for the Prevention of Air Pollution from Ships and Final Act of the 1997 MARPOL Conference and the Technical Code on Control of Emission of Nitrogen Oxides from Marine Diesel Engines*. IMO, London, 1998. ISBN 9280160893. doi: Sales.

International Maritime Organization. *IMO 2020: Consistent implementation of MARPOL ANNEX VI*. IMO Publication. International Maritime Organization, London, 2019. ISBN 9789280117189.

International Maritime Organization. Initial imo ghg strategy, 2023. URL https://www.imo.org/en/MediaCentre/HotTopics/Pages/Reducing-greenhouse-gas-emissions-from-ships.aspx.

Lasse Johansson, Jukka-Pekka Jalkanen, and Jaakko Kukkonen. Global assessment of shipping emissions in 2015 on a high spatial and temporal resolution. *Atmospheric Environment*, 167:403–415, 2017. ISSN 13522310. doi: 10.1016/j.atmosenv.2017.08.042.

L. Kattner, B. Mathieu-Üffing, J. P. Burrows, A. Richter, S. Schmolke, A. Seyler, and F. Wittrock. Monitoring compliance with sulfur content regulations of shipping fuel by in situ measurements of ship emissions. *Atmospheric Chemistry and Physics*, 15(17):10087–10092, 2015. doi: 10.5194/acp-15-10087-2015.

Lisa Kattner. *Measurements of shipping emissions with in-situ instruments*. PhD thesis, 2019.

Ugur Kesgin and Nurten Vardar. A study on exhaust gas emissions from ships in Turkish Straits. *Atmospheric Environment*, 35(10):1863–1870, 2001. ISSN 13522310. doi: 10.1016/S1352-2310(00)00487-8.

Martin Kleinebrahm and Gaston-José Bourbon. *Minderung der Feinstaub-, Ruß- und Stickstoffoxidemissionen auf dem Fahrgastschiff Jan von Werth durch Nachrüstung eines SCRT-Systems*, volume 49 of *LANUV-Fachbericht*. LANUV, Recklinghausen, 2013. doi: Martin.

Z. Klimont, J. Cofala, I. Bertok, M. Amann, C. Heyes, and F. Gyarfas. Modelling emissions of particulate matter in Europe: A framework to estimate reduction potential and control costs ; Forschungsbericht 29943249, 2002.

Wolfram Knörr, Christoph Heidt, Martin Schmied, and Benedikt Notter. Aktualisierung der Emissionsberechnung für die Binnenschifffahrt und übertragung der Daten in TREMOD, 2013. URL https://www.ifeu.de/fileadmin/uploads/IFEU-INFRAS-2013-Aktualisierung-der-Emissionsberechnung-f%C3%BCr-die-Binnenschifffahrt-und-%C3%9Cbertragung-der-Daten-in-TREMOD3.pdf.

Helmut Kraus. *Die Atmosphäre der Erde: Eine Einführung in die Meteorologie*. Springer, Berlin and Heidelberg, 3., erw. und aktualisierte aufl. edition, 2004. ISBN 3-540-20656-6.

Helmut Kraus. *Grundlagen der Grenzschicht-Meteorologie: Einführung in die Physik der atmosphärischen Grenzschicht und in die Mikrometeorologie*. Springer, Berlin and Heidelberg, 2008. ISBN 978-3-540-75980-5. URL http://digitale-objekte.hbz-nrw.de/webclient/DeliveryManager?pid=2346342&custom_att_2=simple_viewer.

K. Krause, F. Wittrock, A. Richter, D. Busch, A. Bergen, J. P. Burrows, S. Freitag, and O. Halbherr. Determination of no_x emission rates of inland ships from on-shore measurements. *EGUsphere*, 2022:1–24, 2022. doi: 10.5194/egusphere-2022-767. URL https://egusphere.copernicus.org/preprints/egusphere-2022-767/.

Kai Krause, Folkard Wittrock, Andreas Richter, Stefan Schmitt, Denis Pöhler, Andreas Weigelt, and John P. Burrows. Estimation of ship emission rates at a major shipping lane by long-path DOAS measurements. *Atmospheric Measurement Techniques*, 14(8):5791–5807, 2021. doi: 10.5194/amt-14-5791-2021.

N. Kriedel, L. Roux, L. Farhner, S. Meissner, and F. Schubert. INLAND NAVIGATION IN EUROPE MARKET OBSERVATION, 2019. ISSN 2070-6715. URL https://inland-navigation-market.org/wp-content/uploads/2019/11/ccnr_2019_Q2_en-min2.pdf.pdf.

N. Kriedel, L. Roux, L. Farhner, S. Meissner, and T. Bayer. INLAND NAVIGATION IN EUROPE MARKET OBSERVATION, 2020. ISSN 2070-6715. URL https://inland-navigation-market.org/wp-content/uploads/2020/09/CCNR_annual_report_EN_2020_BD.pdf.

N. Kriedel, L. Roux, L. Farhner, S. Meissner, and M. Ferrari. INLAND NAVIGATION IN EUROPE MARKET OBSERVATION, 2021. ISSN 2070-6715. URL https://inland-navigation-market.org/wp-content/uploads/2021/09/CCNR_annual_report_EN_2021_WEB.pdf.

Ralf Kurtenbach, Kai Vaupel, Jörg Kleffmann, Ulrich Klenk, Eberhard Schmidt, and Peter Wiesen. Emissions of NO, NO_2 and PM from inland shipping. *Atmospheric Chemistry and Physics*, 16(22):14285–14295, 2016. doi: 10.5194/acp-16-14285-2016.

Haakon Lindstad, Ryan M. Bright, and Anders H. Strømman. Economic savings linked to future arctic shipping trade are at odds with climate change mitigation. *Transport Policy*, 45:24–30, 2016. ISSN 0967070X. doi: 10.1016/j.tranpol.2015.09.002.

Sina Löschke, editor. *The ocean, guarantor of life - sustainable use, effective protection*, volume 7 of *World ocean review : [...], [Englische Ausgabe]*. maribus gGmbH, Hamburg, 2021. ISBN 9783866486980.

Hongrui Ma, Koen Steernberg, Xavier Riera-Palou, and Nigel Tait. Well-to-wake energy and greenhouse gas analysis of sox abatement options for the marine industry. *Transportation Research Part D: Transport and Environment*, 17(4):301–308, 2012. ISSN 13619209. doi: 10.1016/j.trd.2012.01.005.

Ioannis Manisalidis, Elisavet Stavropoulou, Agathangelos Stavropoulos, and Eugenia Bezirtzoglou. Environmental and health impacts of air pollution: A review. *Frontiers in public health*, 8:14, 2020. ISSN 2296-2565. doi: 10.3389/fpubh.2020.00014.

MarineTraffic. MarineTraffic – Global Ship Tracking Intelligence (www.marinetraffic.com), 2021. URL https://www.marinetraffic.com/.

Richard Meller and Geert K. Moortgat. Temperature dependence of the absorption cross sections of formaldehyde between 223 and 323 K in the wavelength range 225-375 nm. *Journal of Geophysical Research*, 105(D6):7089–7101, 2000. ISSN 0148-0227. doi: 10.1029/1999JD901074.

Jana Moldanová, Erik Fridell, Olga Popovicheva, Benjamin Demirdjian, Victoria Tishkova, Alessandro Faccinetto, and Cristian Focsa. Characterisation of particulate matter and gaseous emissions from a large ship diesel engine. *Atmospheric Environment*, 43(16):2632–2641, 2009. ISSN 13522310. doi: 10.1016/j.atmosenv.2009.02.008.

Naceur et al. *Energy and air pollution*. World Energy Outlook 2016 Special Report. International Energy Agency, Paris, 2016. URL http://www.iea.org/publications/freepublications/publication/weo-2016-special-report-energy-and-air-pollution.html.

Theo E. Notteboom and Bert Vernimmen. The effect of high fuel costs on liner service configuration in container shipping. *Journal of Transport Geography*, 17(5):325–337, 2009. ISSN 09666923. doi: 10.1016/j.jtrangeo.2008.05.003.

F. Pasquill. *Atmospheric diffusion: The dispersion of windborne material from industrial and other sources*. D. Van Nostrand, 1. publ., reprint edition, 1968.

L. Pirjola, A. Pajunoja, J. Walden, J.-P. Jalkanen, T. Rönkkö, A. Kousa, and T. Koskentalo. Mobile measurements of ship emissions in two harbour areas in Finland. *Atmospheric Measurement Techniques*, 7(1):149–161, 2014. doi: 10.5194/amt-7-149-2014.

Ulrich Platt and Jochen Stutz. *Differential Optical Absorption Spectroscopy: Principles and Applications*. Physics of Earth and Space Environments. Springer, Berlin and Heidelberg, 2008. ISBN 978-3-540-21193-8. doi: 10.1007/978-3-540-75776-4. URL http://nbn-resolving.de/urn:nbn:de:1111-20080905298.

Martin Otto Paul Ramacher, Volker Matthias, Armin Aulinger, Markus Quante, Johannes Bieser, and Matthias Karl. Contributions of traffic and shipping emissions to city-scale NO_x and PM2.5 exposure in Hamburg. *Atmospheric Environment*, 237:117674, 2020. ISSN 13522310. doi: 10.1016/j.atmosenv.2020.117674.

A. Richter, M. Begoin, A. Hilboll, and J. P. Burrows. An improved NO_2 retrieval for the GOME-2 satellite instrument. *Atmospheric Measurement Techniques*, 4(6):1147–1159, 2011. doi: 10.5194/amt-4-1147-2011.

Andreas Richter, Veronika Eyring, John P. Burrows, Heinrich Bovensmann, Axel Lauer, Bernd Sierk, and Paul J. Crutzen. Satellite measurements of NO_2 from international shipping emissions. *Geophysical Research Letters*, 31(23), 2004. ISSN 00948276. doi: 10.1029/2004GL020822.

Tobias Christoph Valentin Werner Riess, Klaas Folkert Boersma, Jasper van Vliet, Wouter Peters, Maarten Sneep, Henk Eskes, and Jos van Geffen. Improved monitoring of shipping NO_2 with TROPOMI: decreasing NO_x emissions in European seas during the COVID-19 pandemic. *Atmospheric Measurement Techniques*, 15(5):1415–1438, 2022. doi: 10.5194/amt-15-1415-2022.

József Rohács and Gyozo Simongáti. The role of inland waterway navigation in a sustainable transport system. *Transport*, 22(3):148–153, 2007. doi: 10.1080/16484142.2007.9638117.

Schweighofer, J. and Blaauw, H. FINAL REPORT THE CLEANEST SHIP PROJECT, 2009.

John H. Seinfeld and Spyros N. Pandis. *Atmospheric chemistry and physics: From air pollution to climate change*. Wiley, Hoboken, NJ, 2. ed. edition, 2006. ISBN 0471720186. URL http://www.loc.gov/catdir/enhancements/fy0826/2005058370-b.html.

A. Serdyuchenko, V. Gorshelev, M. Weber, W. Chehade, and J. P. Burrows. High spectral resolution ozone absorption cross-sections – Part 2: Temperature dependence. *Atmospheric Measurement Techniques*, 7(2):625–636, 2014. doi: 10.5194/amt-7-625-2014.

André Seyler, Folkard Wittrock, Lisa Kattner, Barbara Mathieu-Üffing, Enno Peters, Andreas Richter, Stefan Schmolke, and John P. Burrows. Monitoring shipping emissions in the German Bight using MAX-DOAS measurements. *Atmospheric Chemistry and Physics*, 17(18):10997–11023, 2017. doi: 10.5194/acp-17-10997-2017.

André Seyler, Andreas C. Meier, Folkard Wittrock, Lisa Kattner, Barbara Mathieu-Üffing, Enno Peters, Andreas Richter, Thomas Ruhtz, Anja Schönhardt, Stefan Schmolke, and John P. Burrows. Studies of the horizontal inhomogeneities in NO_2 concentrations above a shipping lane using ground-based multi-axis differential optical absorption spectroscopy (MAX-DOAS) measurements and validation with airborne imaging DOAS measurements. *Atmospheric Measurement Techniques*, 12(11):5959–5977, 2019. doi: 10.5194/amt-12-5959-2019.

T. W. P. Smith, J. P. Jalkanen, B. A. Anderson, J. J. Corbett, J. Faber, S. Hanayama, E. O'Keeffe, S. Parker, L. Johansson, L. Aldous, C. Raucci, M. Traut, S. Ettinger, D. Nelissen, D. S. Lee, S. Ng, A. Agrawal, J. J. Winebrake, M. Hoen, S. Chesworth, and A. Pandey. *THIRD IMO GHG study 2014: Full report*. International Maritime Organization, London, 2015.

O. G. Stutton. A theory of eddy diffusion in the atmosphere. *Proceedings of the Royal Society of London. Series A, Containing Papers of a Mathematical and Physical Character*, 135(826):143–165, 1932. ISSN 0950-1207. doi: 10.1098/rspa.1932.0025.

J. Stutz and U. Platt. Numerical analysis and estimation of the statistical error of differential optical absorption spectroscopy measurements with least-squares methods. *Applied optics*, 35(30):6041–6053, 1996. ISSN 1559-128X. doi: 10.1364/ao.35.006041.

J. Stutz, E. S. Kim, U. Platt, P. Bruno, C. Perrino, and A. Febo. UV-visible absorption cross sections of nitrous acid. *Journal of Geophysical Research*, 105(D11):14585–14592, 2000. ISSN 0148-0227. doi: 10.1029/2000JD900003.

Lin Tang, Martin O. P. Ramacher, Jana Moldanová, Volker Matthias, Matthias Karl, Lasse Johansson, Jukka-Pekka Jalkanen, Katarina Yaramenka, Armin Aulinger, and Malin Gustafsson. The impact of ship emissions on air quality and human health in the Gothenburg area – Part 1: 2012 emissions. *Atmospheric Chemistry and Physics*, 20(12):7509–7530, 2020. doi: 10.5194/acp-20-7509-2020.

Ryan Thalman and Rainer Volkamer. Temperature dependent absorption cross-sections of O2-O2 collision pairs between 340 and 630 nm and at atmospherically relevant pressure. *Physical chemistry chemical physics : PCCP*, 15(37):15371–15381, 2013. doi: 10.1039/c3cp50968k.

C. Trozzi and R. Vaccaro. Methodologies for estimating air pollutant emissions from ships, Technical Report MEET. (Methodologies for Estimating Air Pollutant Emissions from Transport) RF98, 1998.

UBA. Nationale trendtabellen für die deutsche berichterstattung atmosphärischer emissionen 1990 - 2020, 2022. URL https://www.umweltbundesamt.de/themen/luft/emissionen-von-luftschadstoffen.

Umweltbundesamt, 2022. URL https://thru.de/thrude/.

UNCTAD. *UNCTAD Handbook of Statistics 2020*. United Nations, 2021. ISBN 978-92-1-005354-9. URL https://www.un-ilibrary.org/content/books/9789210053549.

UNCTAD. *REVIEW OF MARITIME TRANSPORT 2021*. United Nations, [S.l.], 2022a. ISBN 978-92-1-113026-3.

UNCTAD. *REVIEW OF MARITIME TRANSPORT 2022*. United Nations, [S.l.], 2022b. ISBN 978-92-1-113073-7. URL https://unctad.org/system/files/official-document/rmt2022_en.pdf.

UNCTAD. *UNCTAD Handbook of Statistics 2021*. United Nations, 2022c. ISBN 978-92-1-001061-0. URL https://www.un-ilibrary.org/content/books/9789210010610.

H. D. van der Gon and J. Hulskotte. Methodologies for estimating shipping emissions in the Netherlands, A documentation of currently used emission factors and related activity data, BOP report, Netherlands Environmental Assessment Agency, 2010. URL https://www.tno.nl/media/2151/methodologies_for_estimating_shipping_emissions_netherlands.pdf.

A. C. Vandaele, C. Hermans, P. C. Simon, M. van Roozendael, J. M. Guilmot, M. Carleer, and R. Colin. Fourier transform measurement of NO_2 absorption cross-section in the visible range at room temperature. *Journal of Atmospheric Chemistry*, 25(3):289–305, 1996. ISSN 0167-7764. doi: 10.1007/BF00053797.

John M. Wallace and Peter Victor Hobbs. *Atmospheric science: An introductory survey*, volume 92 of *International geophysics series*. Academic Press, Amsterdam and Heidelberg, 2. ed. edition, 2006. ISBN 012732951X. URL http://www.loc.gov/catdir/enhancements/fy0634/2005034642-d.html.

WHO. Air pollution, 2023. URL https://www.who.int/health-topics/air-pollution.

E. J. Williams, B. M. Lerner, P. C. Murphy, S. C. Herndon, and M. S. Zahniser. Emissions of NO_x , SO_2 , CO, and HCHO from commercial marine shipping during Texas Air Quality Study (TexAQS) 2006. *Journal of Geophysical Research*, 114(D21), 2009. ISSN 0148-0227. doi: 10.1029/2009JD012094.

Axel Zenger. *Atmosphärische Ausbreitungsmodellierung: Grundlagen und Praxis*. Springer, Berlin and Heidelberg, 1998. ISBN 978-3-642-63811-4. doi: DOI10.1007/978-3-642-58979-9.

Fan Zhang, Yingjun Chen, Chongguo Tian, Diming Lou, Jun Li, Gan Zhang, and Volker Matthias. Emission factors for gaseous and particulate pollutants from offshore diesel engine vessels in China. *Atmospheric Chemistry and Physics*, 16(10):6319–6334, 2016. doi: 10.5194/acp-16-6319-2016.

Fan Zhou, Shengda Pan, Wei Chen, Xunpeng Ni, and Bowen An. Monitoring of compliance with fuel sulfur content regulations through unmanned aerial vehicle (UAV) measurements of ship emissions. *Atmospheric Measurement Techniques*, 12(11):6113–6124, 2019. doi: 10.5194/amt-12-6113-2019.

Fan Zhou, Liwei Hou, Rui Zhong, Wei Chen, Xunpeng Ni, Shengda Pan, Ming Zhao, and Bowen An. Monitoring the compliance of sailing ships with fuel sulfur content regulations using unmanned aerial vehicle (UAV) measurements of ship emissions in open water. *Atmospheric Measurement Techniques*, 13(9):4899–4909, 2020. doi: 10.5194/amt-13-4899-2020.

List of Figures

List of Tables

Erklärung

Hiermit versichere ich, dass ich die vorliegende Arbeit selbstständig verfasst und keine anderen als die angegebenen Quellen und Hilfsmittel verwendet habe. Alle Stellen der Arbeit, die wörtlich oder sinngemäß aus Veröffentlichungen oder aus anderweitigen fremden Äußerungen entnommen wurden, sind als solche kenntlich gemacht.

Kai Krause

Bremen, 19.6.2023

Danksagung

Ich möchte Prof. Dr. John P. Burrows für die Möglichkeit danken, am IUP Bremen an einem nicht nur wissenschaftlich interessanten, sondern gesellschaftlich relevantem und angewandten Themengebiet forschen zu können. Vielen Dank auch für die Kommentare und Vorschläge zu meinen Veröffentlichungen.
Ich danke auch Prof. Dr. Markus Quante für die Übernahme des Zweitgutachtens und das Interesse an meiner Arbeit.
Großer Dank gilt auch Folkard Wittrock für die Betreuung meiner Arbeit und die gekühlten Getränke, wenn in Wedel mal wieder am DOAS geschraubt werden musste.
Vielen Dank auch an Stefan Schmitt und Denis Pöhler für die Hilfe beim Aufbau und Betrieb der beiden LP-DOAS. Insbesondere der schnelle, unkomplizierte Support, wenn wieder etwas nicht funktionierte, war hilfreich. Stefan Schmitt möchte ich zudem für die zusätzlich eingebrachten Ideen während der PhD-Committee Meetings danken. Vielen Dank auch an Andreas Weigelt vom BSH, der mir die ein oder andere Fahrt nach Wedel erspart hat.
Besonderer Dank gilt auch Andreas Richter, insbesondere für die vielen Ratschläge und Kommentare zu den Veröffentlichungen und dieser Dissertation.
Anja Schönhardt und (wieder) Andreas Richter möchte ich für die durchweg entspannte Atmosphäre im Büro danken, auch in stressigen Zeiten.
Ich möchte auch Dieter Busch, Anton Bergen, Svenja Sommer und Patrick Wagner für die Zusammenarbeit im CLINSH-Projekt danken. Besonderer Dank gilt dabei noch einmal Svenja für die Daten zu den Fließgeschwindigkeiten des Rheins aus SOBEK.
Vielen Dank auch an die DOAS-Arbeitsgruppe für die entspannte Atmosphäre, die vielen Kuchen nach den DOAS-Seminaren und das ein oder andere Bierchen am Freimarkt oder anderen abendlichen Freizeitveranstaltungen.
Bedanken möchte ich mich außerdem bei meinen Freunden für viele unterhaltsame Stunden, offline mit alkoholischen und nichtalkoholischen Getränken und gutem Essen oder online beim abendlichen Zocken.
Vielen Dank auch an meine Familie und insbesondere an meine Eltern, die mich immer unterstützt haben.
Danken möchte ich auch allen Menschen die ich bis hierhin nicht aufgelistet habe, welche mich aber bei der Anfertigung dieser Arbeit unterstützt haben.